Soteria deliverable 4.3: Solar wind–magnetosphere coupling and the terrestrial impact

Vennerstrøm, Susanne; Christiansen, Freddy; Asikainen, Timo; Mursula, Kalevi; Crespon, François; Tátrallyay, M.; Kecskeméty, K.; Németh, Z.; Kuzin, S. V.; Slemzin, V. A.; Ulyanov, A. S.; Bogachev, S. A.; Sylwester, J.; Gburek, S.; Podgorski, P.; Kowalinski, M.; Verigin, M. I.

Publication date:
2010

Document Version
Publisher's PDF, also known as Version of record

Citation (APA):
Vennerstrøm, S., Christiansen, F., Asikainen, T., Mursula, K., Crespon, F., Tátrallyay, M., ... Verigin, M. I. (2010). Soteria deliverable 4.3: Solar wind–magnetosphere coupling and the terrestrial impact. European Community's Seventh Framework Program.

Deliverable 4.3

Project acronym: *SOTERIA*
Project title: *SOlar-TERrestrial Investigations and Archives*
Grant Agreement number: *218816*
Coordinator: *Giovanni Lapenta*
Project co-funded by the European Commission,
Seventh Framework Programme
Funding Scheme: *FP7-SPACE-CALL-1*

Due date of deliverable:	1 November 2010
Actual submission date:	14 November 2010
Start date of the project:	1 November 2008
Project duration:	3 years

Work package:	4
Task(s):	Solar wind – magnetosphere coupling and the terrestrial impact
Lead beneficiary for this deliverable:	MTA KFKI RMKI
Editor:	Mariella Tátrallyay, Károly Kecskeméty
Authors:	T. Asikainen, S. Bogachev, F. Christiansen, F. Crespon, S. Gburek, K. Kecskeméty, M. Kowalinski, S. Kuzin, K. Mursula, Z. Németh, P. Podgorski, V. Slemzin, J. Sylwester, M. Tátrallyay, A. Ulyanov, S. Vennerstrøm
Quality reviewer:	

Project co-funded by the European Commission within the Seventh Framework Programme (2007)		
Dissemination level		
PU	**Public**	
PP	**Restricted to other programme participants (including the Commission Services)**	**X**
RE	**Restricted to a group specified by the consortium (including the Commission Services)**	
CO	**Confidential, only for members of the consortium (including the Commission Services)**	

Document Control

This document has no controlled or maintained paper copies. The master document is held under soteria on the spaceweather.eu network. All files have widespread access for reading only. Changes to this document will be notified to its audience.

Issue record

Version	Date	Author(s)	Reason for modification	Status
1.0	1.11.2010	M. Tátrallyay and 15 coauthors		Compiled from reports
1.1	14.11.2010			Ready for submission

NOTICE

SOTERIA Deliverable 4.3

Solar wind–magnetosphere coupling and the terrestrial impact

This report was prepared by the following participants of SOTERIA Work Package 4:

Susanne Vennerstrøm, Freddy Christiansen
National Space Institute, Technical University of Denmark, København, Denmark (DTU)

Timo Asikainen, Kalevi Mursula
Department of Physics, University of Oulu, Oulu, Finland (UOulu)

François Crespon
Noveltis, Ramonville-Saint-Agne, France (Noveltis)

Mariella Tátrallyay, Károly Kecskeméty, Zoltán Németh
MTA KFKI Res. Inst. for Particle and Nuclear Physics, Budapest, Hungary (MTA KFKI RMKI)

Sergey V. Kuzin, Vladimir A. Slemzin, A.S. Ulyanov, Sergey A. Bogachev
P.N. Lebedev Physical Institute of Russian Academy of Sciences, Moscow, Russia (LPI)

Janusz Sylwester, Szymon Gburek, Piotr Podgorski, Mirek Kowalinski
Space Research Centre, Polish Academy of Sciences, Wroclaw, Poland (SRC PAS)

Non-SOTERIA collaborator involved:

Mikhail I. Verigin
Space Research Inst., Moscow, Russia

Contents

1. Introduction

This report is presenting the studies performed in the frame of Task 4.2 of SOTERIA: solar wind – magnetosphere coupling and the terrestrial impact. The broad range of research topics includes investigations of different regions of the terrestrial plasma environment: from the outer boundaries of the magnetosphere (bow shock and magnetopause) through the radiation belts down to the ionosphere and upper atmosphere. Magnetic field and plasma data from spacecraft monitoring the interplanetary field and from satellites orbiting the Earth (on higher and lower orbits), ground based observations, empirical and theoretical models were used for the investigations.

The main objectives of Task 4.2 of Work Package 4 were:

1. Determination of the relationship between upstream solar wind parameters, the location of the bow shock and magnetopause and the occurrence of solar wind and energetic particles down to geostationary orbit thereby investigating the radiation hazards of geostationary satellites.

2. Quantify the effect of the local magnetic field intensity, including its time variability during storms, on the radiation level in low Earth orbit.

3. Identification of the dominant parameters in the near Earth solar wind that determine how the energy is transferred from the solar wind to the inner magnetosphere during space storms, and how it is partitioned between atmospheric heating, radiation belt intensification etc.

4. Identification of the different contributions to magnetic perturbations during space storms, such as ring current, magnetopause current, tail-current, field-aligned currents, and ionospheric currents and determination of their relative importance.

5. Study of impact of temporal and spatial variations of the radiation belts and the atmospheric densities produced by the solar wind on the functioning of space based instruments and comparison of the measured data with the SPENVIS model predictions.

WP4 delivered its first report at the end of the first year of the SOTERIA project. The Catalogue of Selected Events (D4.1, at http://soteria-space.eu/doc/reports/SOTERIA_D4_1.pdf) presented eight large solar events from the declining phase of the last solar cycle when extensive observations detected one or more large Coronal Mass Ejections on the Sun together with the ICMEs travelling in interplanetary space and reaching the Earth. Space-borne and ground based observations, as well as empirical and theoretical model calculations in connection with these events were collected in report D4.1 in order to help further, more detailed investigations. In the following sections, different aspects of the events presented in D4.1 are discussed together with other active and quiet periods of the last solar cycle.

In Section 2 three of the selected events of D4.1 are investigated when the magnetopause was unusually close to the Earth due to the extreme solar wind conditions. The location of this boundary is one of the most important parameters in space physics, because it separates the magnetospheric plasma from the solar wind and determines the size of the magnetosphere. The extreme locations of the magnetopause as observed by the Cluster and GOES satellites are discussed here applying different models using interplanetary parameters. From Cluster data, the location of the bow shock is also investigated.

The Dst index was designed to monitor the ring current (originally from ground based magnetic field measurements), containing contributions from other magnetospheric current systems as well. Section 3 is discussing the Dcx (corrected Dst) index and the contributions of ring, tail and magnetopause currents to it. In the past, only some quantitative estimates of the tail current effects were discussed when Dst was estimated. Here, the latitude of the isotropic boundary obtained from the corrected energetic particle measurements aboard the low-altitude NOAA/POES satellites is used as a proxy for the tail current intensity. Using local linear regression methods, quantitative expressions are obtained for the contributions of the different current systems to Dcx. Unknown parameters of the expressions are determined from data measured during the time interval 1999 – 2007 covering all events of D4.1. Event 1 is discussed in more details among the case studies.

Section 4 is dealing with the solar wind energy input into the magnetosphere which is strongly enhanced during periods of southward interplanetary magnetic field. Solar wind effects on the energy injection and dissipation are discussed in the ring current as viewed by the Dcx index and by energetic proton observations aboard the NOAA/POES satellites, and in the ionosphere where the energy is dissipated as Joule heating by field aligned currents closing through the ionosphere. The large scale structure of the full ionospheric/field-aligned current system is derived from single passes of the Ørsted and Champ satellites for the November 2003 storm (Event 5 of D4.1). Assuming a given ionospheric conductance, the ionospheric potential equation is solved and from this the Joule heating of the ionosphere is computed.

Solar energetic particles penetrate the magnetosphere from polar regions down to the cut-off latitude. In Section 5.1, the cut-off latitude values determined directly from SAMPEX - PET and POES - MEPED data are compared with low-latitude magnetic disturbances measured by the Ørsted, Champ and SAC-C satellites and with the Dst and Auroral Boundary indices during large geomagnetic activity. Two events are discussed in details; one is Event 3 of D4.1. Auroral electrojets, their latitudinal migration during storms, their intensity and various precipitation boundaries associated with the electrojets may be monitored by magnetic intensity measurements from satellites on low-Earth polar orbit as discussed in Section 5.2. For all events of D4.1, the total electron content (TEC) is determined for high latitudes and the equatorward auroral boundary latitude is estimated from the TEC maps.

Space instruments aboard near-Earth orbiting satellites are operated under the impact of various environmental factors. Some of these factors may lead to distortion of the observational data and provide cumulative effects which may reduce the useful operational time or may change the operational ranges of the instruments. Section 6.1 presents the radiation belt effects on the data obtained with the TESIS solar telescope and on the SPHINX X-ray spectrophotometer aboard the CORONAS-Photon satellite during the solar minimum period between February and November 2009. The observational results are compared with the predictions of the SPENVIS space environment model. Section 6.2 is analyzing the radiation damage of the MEPED detectors measuring energetic protons between 30 keV and 6.9 MeV onboard the low-altitude NOAA/POES satellites. For the first time, the entire time series of NOAA/POES measurements were studied extending nearly continuously from 1978 to present. By inter-satellite comparison, we studied the effects of the radiation damage on the instruments and computed correcting factors for each satellite.

Low-Earth orbiting satellites experience orbit decay due to atmospheric drag. The density of the atmosphere at the altitude of satellites is mainly influenced by three factors: solar heating of the thermosphere by EUV radiation, kinetic energy depositing by precipitating particles, and Joule heating by ionospheric currents. The decay of the Champ orbit is examined in Section 6.3 for more than four years (2001-2005) including four of the selected events of D4.3.

This report is the result of cooperative efforts of teams participating in SOTERIA Work Package 4. The authors of the report had the following meetings during the first 2 years of the project where they presented the status of their research, discussed the problems and results, shared the tasks for running and future collaborations:

SOTERIA Workshop, Saariselka, 23-24 March 2009;
Event Study Workshop of WP4, Hvar, 14-18 September 2009;
1st SOTERIA General Meeting and WP4 Workshop, Davos, 18-21 January 2010;
WP4 Workshop, Budapest 10-12 August 2010.

We also organized teleconferences with the participation of all teams and there were many bilateral discussions by phone and by e-mail. The joint work will be continued in the future, several papers are getting prepared for publication.

2 Location of the terrestrial magnetopause and the bow shock

2.1 Background and purpose of the study

The terrestrial magnetopause is the result of the interaction between the supersonic solar wind and the Earth's magnetic field. The location of the magnetopause is one of the most important parameters in space physics because it is the boundary that separates the magnetospheric plasma from the solar wind and determines the size of the magnetosphere. As the velocity of the solar wind exceeds the velocity of sonic, Alfvenic, and magnetosonic waves in interplanetary space, a bow shock forms in front of the magnetopause where plasma parameters suddenly change: velocity decreases while density, temperature, and the tangential component of the magnetic field increase. The region between the bow shock and the magnetopause is the magnetosheath.

Since Ferraro (1952) first calculated the size of the magnetosphere, space physicists have done much effort to model the location and shape of the magnetopause under different solar wind conditions. Most of the early studies supposed that the location of the magnetopause depends solely on solar wind dynamic pressure. Fairfield (1971) recognized that the interplanetary magnetic field (IMF) can also affect the magnetopause location. Later, more empirical models were developed using large in situ data sets of magnetopause crossings. Some models define the magnetopause size and shape in limited parameter ranges, and they are not valid for the broad, and especially for the extreme ranges of solar wind conditions.

Interplanetary plasma and magnetic field parameters significantly change in connection with large solar events like flares and coronal mass ejections (CMEs). The velocity of the solar wind can increase well above 1000 km/s while the average value is ~400 km/s. Also, the density of plasma can be about 10 times larger than average. High solar wind dynamic pressure and large negative values of the north-south component of the interplanetary magnetic field (IMF B_z) drastically compress the terrestrial magnetosphere.

Work Package 4 of SOTERIA selected eight events during the declining phase of the last solar cycle when extensive observations detected one or more large CMEs on the Sun together with the ICMEs travelling in interplanetary space and reaching the Earth. Space-borne and ground based observations, as well as empirical and theoretical model calculations in connection with these events were published in the Catalogue of Selected Events (SOTERIA Deliverable 4.1, 2009 at http://soteria-space.eu/doc/reports/SOTERIA_D4_1.pdf)

Most of the listed large solar events caused extremely strong geomagnetic storms. Two of these events are investigated here when the Cluster spacecraft observed the magnetopause and the bow shock unusually close to the Earth due to extreme solar wind conditions. During these events and also in another case, the magnetopause was inside the geosynchronous orbit of the GOES satellites at 6.3 R_E for several hours. The observed extreme locations of these discontinuities are discussed applying different bow shock and magnetopause models using interplanetary parameters which were taken from the OMNI dataset (based on Wind and Geotail measurements propagated to the nose of the bow shock) and from ACE. These interplanetary data are available at NASA´s Coordinated Data Analysis Web:
http://cdaweb.gsfc.nasa.gov/istp_public/

2.2 Modelling the magnetopause location

2.2.1 Two-dimensional modelling

Two-dimensional models assume cylindrical symmetry around the aberrated Sun-Earth line. Empirical models developed in the last century are mainly based on magnetopause crossings observed close to the equatorial or ecliptic plane. They provide mathematical expressions for the size and shape of the magnetopause as functions of IMF B_z and solar wind dynamic pressure.

From these models, the magnetopause is easily predictable for any given upstream condition. In this work two widely used 2D models were applied.

Shue et al. (1997) derived a model by fitting observed magnetopause locations to the functional form of a conic of revolution: $R_{MP} = R_{MP0}\,(2/(1+\cos\theta))^{\alpha}$ where R_{MP} is the radial distance to the observation point and θ is the solar zenith angle (angle between the solar and R_{MP} direction). This form has two parameters: R_{MP0} is the standoff distance and α controls the tail flaring. It can describe both the open and closed magnetosphere on the night side, depending on the value of α. The parameters were determined as the function of the solar wind dynamic pressure P_d and IMF B_z in Geocentric Solar Magnetospheric coordinates (X is the direction from the Earth to the Sun, and the magnetic dipole is in the X-Z plane):

$R_{MP0} = \{11.4 + K\,B_z\}\,P_d^{-1/6.6}$ where $K = 0.013$ if $B_z > 0$ and $K = 0.14$ if $B_z < 0$, and

$\alpha = (0.58 - 0.01B_z)\,(1 + 0.01\,P_d)$.

Later, Shue et al. (1998) improved their model for extreme solar wind conditions. They introduced a nonlinear dependence of the parameters to better describe the solar wind pressure effect on the magnetopause flaring and the IMF B_z effect on the subsolar standoff distance:

$R_{MP0} = \{10.22 + 1.29\tanh[0.184\,(B_z + 8.14)]\}\,P_d^{-1/6.6}$ and

$\alpha = (0.58 - 0.007B_z)\,(1 + 0.024\ln[P_d])$.

The two models provide the same result for average solar wind conditions, however, the saturation effect in the two parameters is better represented by the improved model (Shue et al., 1998) under extremely large dynamic pressure and/or large negative IMF B_z .

2.2.2 Three-dimensional modelling

Recently, Lin et al. (2010) developed an asymmetric three-dimensional magnetopause model in GSM coordinates in which the location and shape of the magnetopause depends not only on $\theta = \arccos(X/R_{MP})$ solar zenith angle, but also on the azimuth angle $\varphi = \arctan[Z_{GSM}, Y_{GSM}]$ and on the dipole tilt angle ϕ measured from $+Z_{GSM}$ towards the solar direction. From the interplanetary parameters, the magnetic pressure P_m is also taken into account in addition to solar wind dynamic pressure P_d (usually $P_m < P_d/100$) and IMF B_z:

$R_{MP}\,(\theta,\varphi,\phi) = R_0\,F(\theta,\varphi,\phi) + a_{14}(P_d + P_m)^{a15}\,\{\exp[d_n\Psi_n^{a21}] + \exp[d_s\Psi_s^{a21}]\}$

where $R_0 = a_0(P_d + P_m)^{a1}\{1 + a_2\exp[a_3B_z - 1]/\exp[a_4B_z + 1]\}$

$F(\theta,\varphi,\phi) = \{\cos(\theta/2) + a_5\sin(2\theta)(1 - \exp[-\theta])\}^{\beta(\varphi,\phi)}$

$\beta(\varphi,\phi) = a_6 + a_7\exp[(a_8B_z) - 1]/[\exp(a_9B_z) + 1] + a_{10}\cos\varphi + (a_{11} + a_{12}\phi)\sin\varphi + a_{13}(\sin\varphi)^2$

$d_n = a_{16} + a_{17}\phi + a_{18}\phi^2$ $d_s = a_{16} - a_{17}\phi + a_{18}\phi^2$

$\theta_n = a_{19} + a_{20}\phi$ $\theta_s = a_{19} - a_{20}\phi$

$\Psi_n = \arccos[\cos\theta\cos\theta_n + \sin\theta\sin\theta_n\cos(\varphi - \pi/2)]$

$\Psi_s = \arccos[\cos\theta\cos\theta_s + \sin\theta\sin\theta_s\cos(\varphi - 3\pi/2)]$

Here $\beta(\varphi,\phi)$ controls the tail flaring, θ_n and θ_s is the solar zenith angle of the north and south indentation vertex, respectively, while Ψ_n and Ψ_s is the angle between the direction of $R_{MP}(\theta,\varphi,\phi)$ and the direction to the actual indentation vertex.

Lin et al. (2010) determined the 22 constants a_0 through a_{21} of their three-dimensional model from 1226 magnetopause crossings observed by 10 spacecraft (including satellites on polar orbit) using the Levenberg-Marquart method for nonlinear multiparameter fitting.

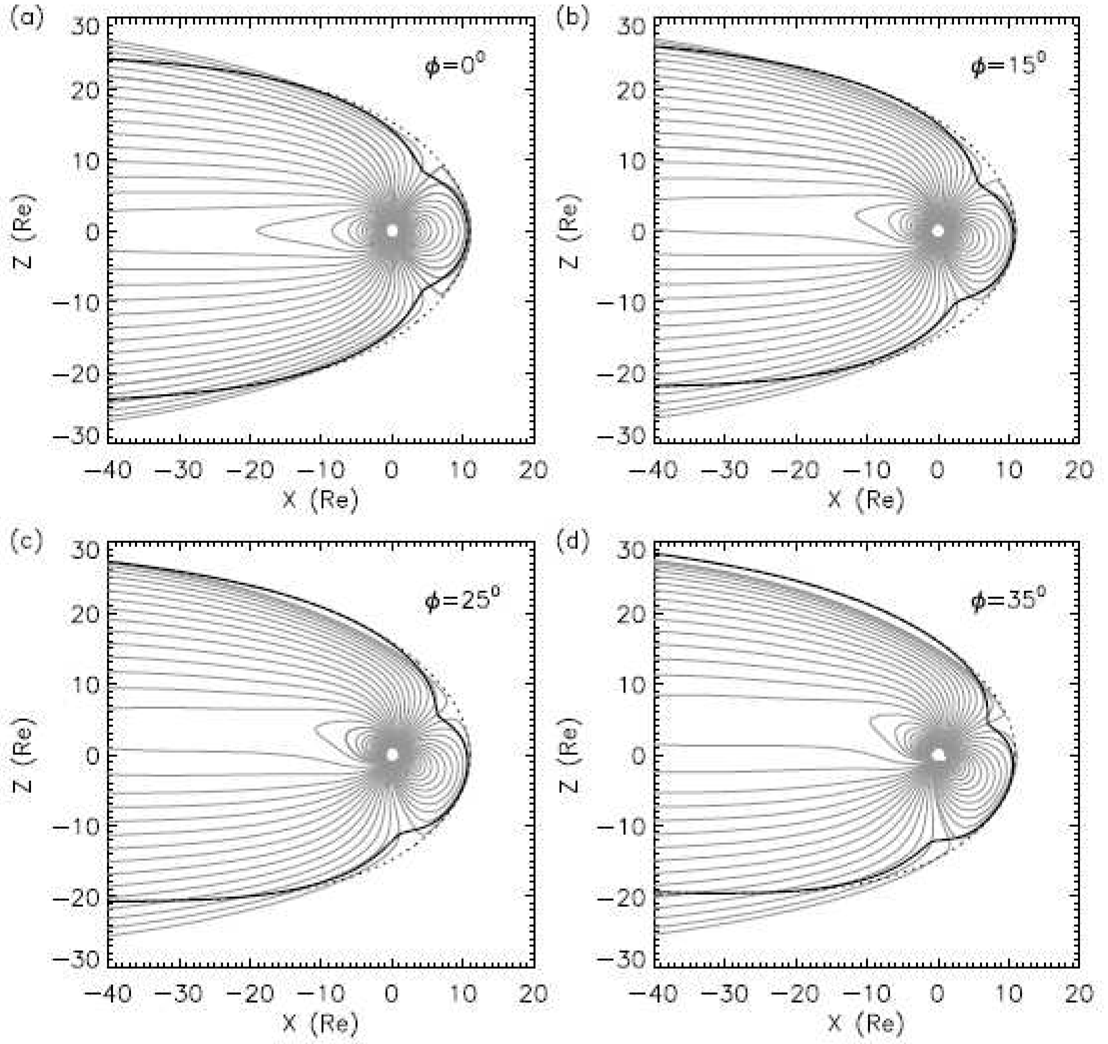

Fig. 2.1 Magnetopause shapes (thick solid curves) from the model of Lin et al. (2010) and the magnetic field lines (gray curves) from the Tsyganenko (1996) model in the X-Z plane for different ϕ dipole tilt angle values. The dotted curves present the magnetopause when the indentations are not considered in the model of Lin et al. (2010). (Fig. 8 of Lin et al., 2010.)

Figure 2.1 demonstrates that the indentations in Lin´s model are near the center of the cusp ´funnel´ provided by the model of Tsyganenko (1996) and their location is obviously controlled by ϕ. The model of Lin et al. (2010) is expected to give a better representation of the magnetopause compared to the two-dimensional models, especially at higher geomagnetic latitudes.

2.3 Modelling the bow shock location

2.3.1 Two-dimensional modelling

The simple empirical two-dimensional models assume that the bow shock is symmetric about the Sun – obstacle line and it can be represented by a general conic of revolution as

$$R_{BS} = R_{BS0}\,(1+ \varepsilon)/(1+ \varepsilon \cos\theta)$$

where θ is the solar zenith angle and the two parameters are: R_{BS0} standoff distance and ε eccentricity. Farris et al. (1991) fitted this formula of conic revolution to 351 independent bow shock crossings observed by the ISEE1 spacecraft and received $\varepsilon = 0.81$ and $R_{BS0} = 13.7\ R_E$. Several other studies determined the average location and shape of the bow shock providing slightly different values for ε and R_{BS0} depending on the observations used for the fitting.

In the present study, $\varepsilon = 0.81$ is used in the formula as determined by Farris et al. (1991) substituting the actual standoff distance calculated from interplanetary solar wind and magnetic field parameters according to Farris and Russell (1994):

$$R_{BS0} = R_{MP0}\{1+1.1[(\gamma-1)M_{ms}^2 + 2]/[(\gamma+1)(M_{ms}^2 - 1)]\}$$

where $M_{ms}=V_{sw}/V_{ms}$ is the upstream magnetosonic Mach number, γ polytropic index is 5/3, and the magnetopause standoff distance R_{MP0} is calculated from one of the magnetopause models. When M_{ms} could not be determined and therefore R_{BS0} was not available, $R_{BS0} = 1.25\ R_{MP0}$ was used.

2.3.2 Three-dimensional modelling

Verigin et al. (2001, 2003) developed a semi-empiric three-dimensional bow shock model combined with MHD solution using the GIPM (Geocentric InterPlanetary Medium) reference frame based on the direction of the solar wind and the IMF. In the following forms $\mathbf{V_{sw}}$ (V_x,V_y,V_z) is the solar wind velocity vector in Geocentric Solar Ecliptic coordinates, V_E is the orbital velocity of the Earth, and **B** is the interplanetary magnetic field vector.

The axes of the GIPM coordinate system are determined as follows:

$\mathbf{e_x} = (-V_x,-V_y-V_E,-V_z)/|\mathbf{V_{sw}}|$, i.e. $\mathbf{e_x}$ is anti-parallel to the solar wind direction

$\mathbf{e_y} = -\mathbf{B} + (\mathbf{B},\mathbf{e_x})\mathbf{e_x} / |\mathbf{B} - (\mathbf{B},\mathbf{e_x})\mathbf{e_x}|$ for $(\mathbf{B},\mathbf{e_x}) > 0$ or

$\mathbf{e_y} = \mathbf{B} - (\mathbf{B},\mathbf{e_x})\mathbf{e_x} / |\mathbf{B} - (\mathbf{B},\mathbf{e_x})\mathbf{e_x}|$ for $(\mathbf{B},\mathbf{e_x}) < 0$, i.e. $\mathbf{e_y}$ is anti-parallel or parallel to the IMF component perpendicular to the solar wind direction depending on the direction of $(\mathbf{B},\mathbf{e_x})$,

$\mathbf{e_z} = \mathbf{e_x} \times \mathbf{e_y}$, meaning that $(\mathbf{B},\mathbf{e_z}) = 0$, i.e. the IMF is in the X-Y plane.

The bow shock standoff distance, curvature radius of its nose, and the asymptotic cone angle of the tail are determined using the actually measured solar wind velocity, interplanetary magnetic field, solar wind dynamic pressure, Alfvenic and sonic Mach numbers. The exact MHD solution is used for determining the tail flaring. The bow shock model of Verigin et al. (2001, 2003) is used only for one of the investigated cases when all measured interplanetary parameters (including solar wind temperature) were reliable and could be propagated to the nose of the bow shock.

2.4 Three-dimensional MHD modelling in CCMC

The results of a real three-dimensional MagnetoHydrodynamic Model are also used in this study. The Block-Adaptive-Tree-Solarwind-Roe-Upwind-Scheme (BATS-R-US) was developed by the University of Michigan and is now available for the community of space scientists through NASA´s Community Coordinated Modeling Center at http://ccmc.gsfc.nasa.gov/.

It was designed using the Message Passing Interface (MPI) and the Fortran90 standard and executes on a massively parallel computer system. The BATS-R-US code solves 3D MHD equations in finite volume form using numerical methods related to Roe's Approximate Riemann Solver. It uses an adaptive grid composed of rectangular blocks arranged in varying degrees of spatial refinement levels. Inputs to BATS-R-US are the solar wind density, velocity, temperature, and magnetic field measurements, transformed into GSM coordinates and propagated from the solar wind monitoring satellite's position to the sunward boundary of the simulation domain. The Earth's magnetic field is approximated by a dipole with updated axis orientation and co-rotating inner magnetospheric plasma or with a fixed orientation during the entire simulation run. These runs are time consuming, in our case it took more than 3 weeks from request to completion.

2.5 Case studies

Three events are investigated here in details which are among the Selected Events in report D4.1 of SOTERIA WP4. All three events caused large geomagnetic storms, solar wind dynamic pressure was high for several hours and IMF B_z had large negative values. In all cases one or two of the GOES geosynchronous satellites crossed the magnetopause and measured magnetic field of interplanetary origin (usually negative B_z) for sereval hours instead of the geomagnetic field having positive B_z values close to the equatorial plane on the dayside. In two events the Cluster spacecraft observed the magnetopause and the bow shock unusually close to the Earth.

2.5.1 17-18 January 2005 (Event 7 of D4.1)

Figure 2.2 presents the solar wind velocity, dynamic pressure and IMF taken from NASA's OMNI dataset measured by the Wind spacecraft and propagated to the nose of the bow shock on 17-18 January. The high dynamic pressure observed between 14:00 and 24:00 UT on 17 January was the effect of a solar event which occurred earlier than the two CMEs causing the large geomagnetic storm next day when there is a gap in the interplanetary parameters. The top panel shows the standoff distance of the magnetopause R_{MP0} and that of the bow shock R_{BS0} calculated according to Shue et al. (1997) and Farris and Russell (1994), respectively.

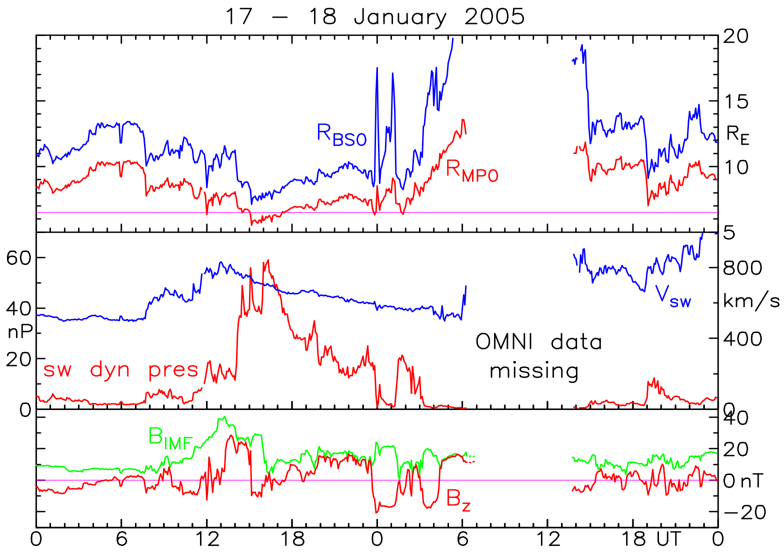

Figure 2.2 Interplanetary parameters at Earth from NASA's OMNI dataset based on Wind measurements.

Top panel: model standoff distances of bow shock R_{BS0} (blue curve) and magnetopause R_{MP0} (red), GOES orbit (lilac). Middle panel: solar wind dynamic pressure (red), velocity (blue). Bottom panel: total IMF (green), B_z component (red).

It is obvious that the nose of the magnetopause was inside the geosynchronous orbit (6.3 R_E is marked by a lilac line) for more than 2 hours after 15:00 UT. GOES12 was in this region and magnetic field data measured aboard clearly show (see Fig. 2.3) that the satellite crossed the magnetopause outbound at 15:15 UT and measured the field of interplanetary origin: small negative and positive B_z values in good agreement with the variations of the IMF. The propagating time from the bow shock to GOES12 was not taken into account, causing a time shift of few minutes between model predictions for the magnetopause crossing and the observation (exit/entry time is indicated by a green vertical line). The time interval when the satellite was upstream of the magnetopause is well predicted by both models of Sue et al. (1997) and Shue et al. (1998). For small B_z values, there is almost no difference between the two models. The model of Lin et al. (2010) slightly overestimates the displacement of the magnetopause towards the Earth.

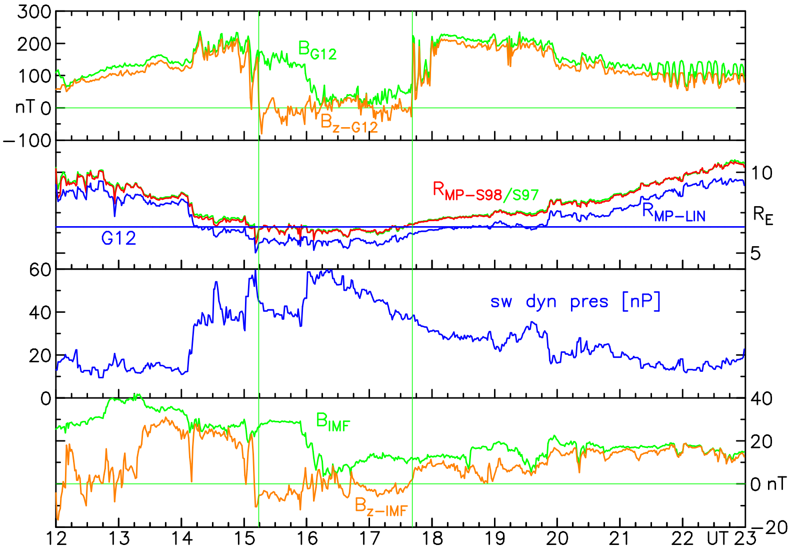

Figure 2.3 Top panel: GOES12 magnetic field observations: total value (green), $B_{z\text{-}GSM}$ (yellow). Panel 2: model magnetopause locations: Shue et al., 1997 (green); Shue et al., 1998 (red); Lin et al., 2010 (blue) for GOES12 trajectory (blue line). Panel 3: solar wind dynamic pressure. Bottom panel: IMF: total field (green), $B_{z\text{-}GSM}$ (yellow).

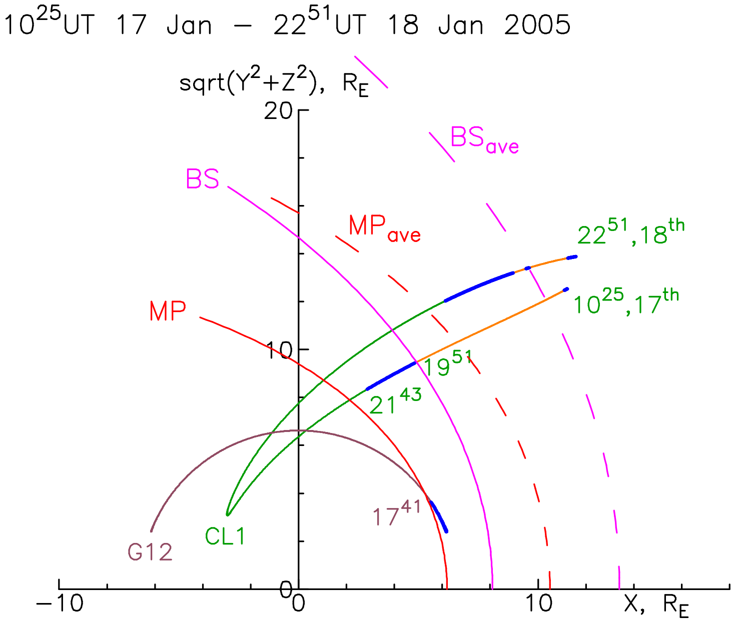

Figure 2.4 Cluster1 (CL1) and GOES12 (G12) orbit in cylindrical coordinates. Sections in the magnetosheath are marked in blue. Yellow sections: interplanetary field. Dashed curves: model bow shock (lilac line) and magnetopause (red line) for average solar wind parameters, solid lines for BS and MP calculated from parameters at 17:41 UT when G12 reentered the magnetopshere. Times of bow shock and magnetopause crossings are marked for Cluster1 inbound pass.

Figure 2.4 shows that Cluster1 spent a short time in the magnetosheath after 10:25 UT on its inbound pass on 17 January. The next inbound bow shock crossing was at 19:51 UT when solar wind dynamic pressure was decreasing after the peak and the magnetosphere was expanding. The model bow shock and magnetopause presented by the solid curves were calculated from a dynamic pressure of ~40 nP measured at 17:41 UT when GOES12 reentered the magnetosphere. When Cluster1 crossed the bow shock and the magnetopause, the dynamic pressure was much smaller meaning that these discontinuities were farther upstream according to the models.

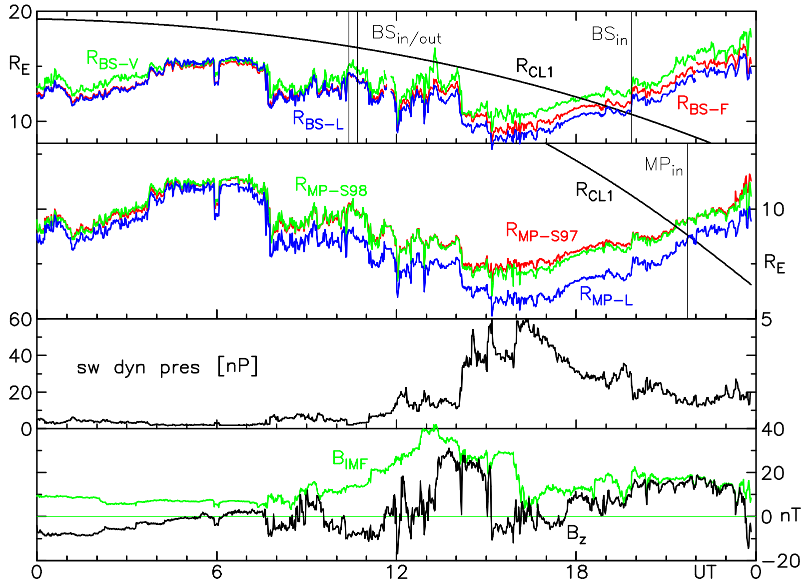

Figure 2.5 Top panel: model bow shock locations: Verigin (green line); Farris with Shue's R_{MP0} (red); Farris with Lin's R_{MP0} (blue) for Cluster1 trajectory (R_{CL1} in black line). Panel 2: model magnetopause locations: Shue 1997 (red line); Shue 1998 (green); Lin (2010) (blue) for Cluster1 trajectory (black). Panel 3: solar wind dynamic pressure. Bottom panel: IMF total value (green) and B_z (black curve).

-

Figure 2.5 presents the results of three different models providing the bow shock and magnetopause location observed by Cluster1. The model of Verigin et al. (2001, 2003) predicts the bow shock at a distance of about 2 R_E farther out than it was observed at 19:51 UT. The best prediction for the bow shock is provided by the model of Farris (1991) with R_{MP0} from the model of Lin et al. (2010). The observed magnetopause location at 21:43 UT is in very good agreement with the model of Lin et al. (2010), while the magnetopause is farther away from the Earth according to the models of Shue et al. (1997) and Shue et al. (1998).

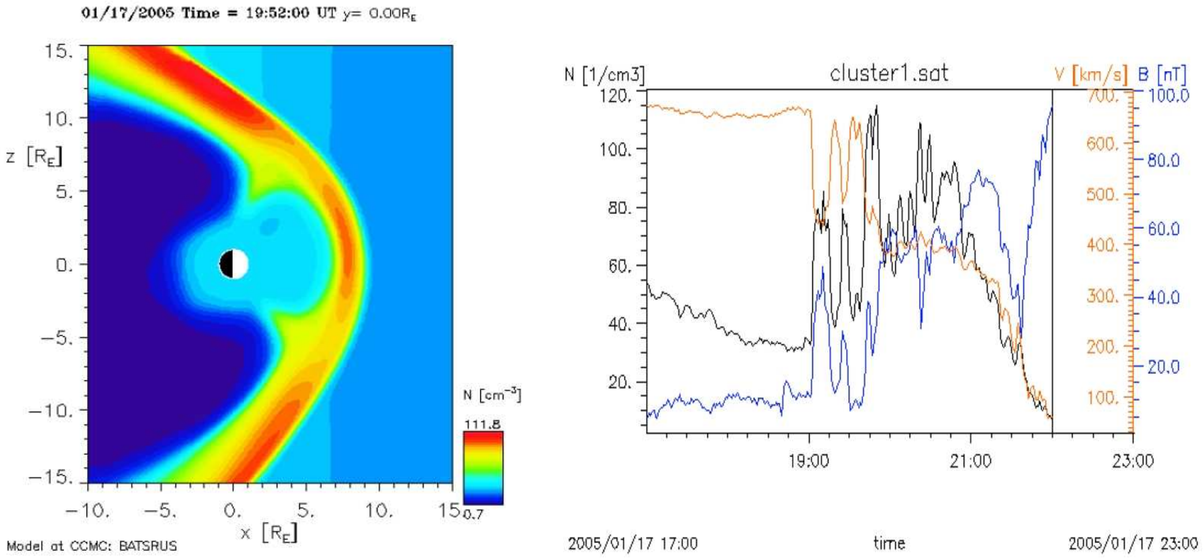

Figure 2.6 Left-side panel: density distribution in the Z-X GSM plane provided by the 3D BATS-R-US for 19:52 UT. Right-side panel: density (black curve), velocity (red) and magnetic field (blue) profiles along the Cluster1 trajectory from 17:00 to 22:00 UT.

We requested a three-dimensional MHD model run from the Community Coordinated Modeling Center of NASA using the BATS-R-US model for the time interval from 10 UT to 22 UT on 17 January 2005. The Earth's magnetic field was approximated by a dipole with updated axis orientation during the run. Figure 2.6 shows some of the results. As seen in the right-hand side figure, this time consuming real 3D model calculation predicts two in- and outbound bow shock crossings between 19:00 UT and 19:30 UT and a final inbound pass around 19:50 UT. The latter time is in good agreement with the observation. The multiple bow shock crossings may be the result of variations in solar wind dynamic pressure and IMF values. The simple 2D models also predict changes in the bow shock location after 19:00 UT (see Fig. 2.5). According to the 3D MHD model, the magnetopause is around 21:40 UT (in good agreement with the observation) when magnetic field increases, while velocity and density decrease. However, the MDH model cannot resolve the thickness of the discontinuity, the magnetopause was much thinner according to the observation compared to the model prediction.

2.5.2 20 November 2003 (Event 5 of D4.1)

During this event the interplanetary magnetic field had an unusally large negative north- south component ($B_z < -30$ nT) for almost 5 hours as seen in Figure 2.7. Two GOES satellites were on the dayside (within about 45^{o} from the nose of the magnetopause) when solar wind dynamic pressure and the IMF reached their maximum values. GOES12 spent more than 6 hours, GOES10 spent 5.5 hours continuously in the magnetosheath. Figure 2.7 presents three different model predictions for the location of the magnetopause for the trajectory of both satellites. It is obvious that the Sue et al. (1997) model overestimates the displacement of the magnetopause towards the Earth, while the Sue et al. (1998) model slightly underestimates it. The results of the model by Lin et al. (2010) provide the best agreement with the observations. The models predict the magnetopause crossings a few minutes earlier than observed (marked with the vertical green lines) as the models use interplanetary parameters upstream of the nose of the bow shock and the propagating time to the GOES satellites is not taken into account.

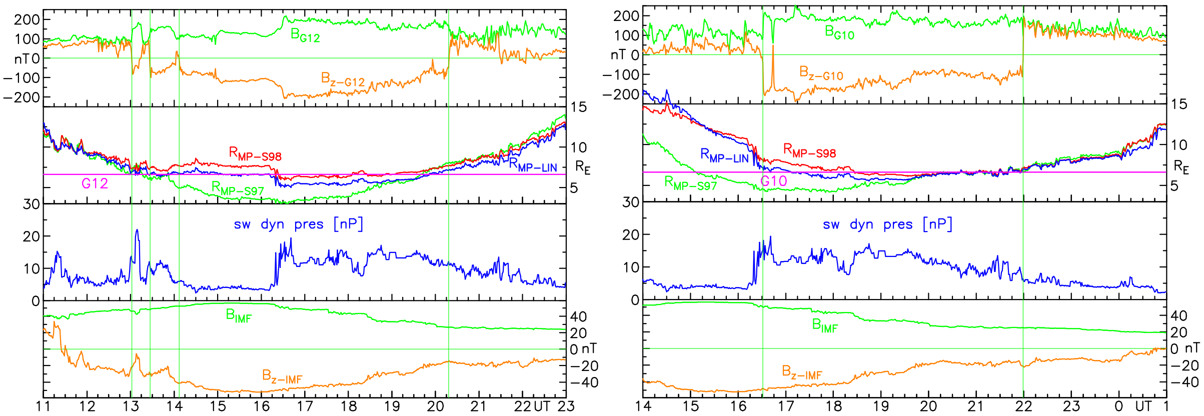

Figure 2.7 Top panels: GOES magnetic field observations (GOES12 on left-hand side, GOES10 on right-hand side) total value (green), $B_{z\text{-}GSM}$ (yellow). Panel 2: model magnetopause locations: Shue et al., 1997 (green); Shue et al., 1998 (red); Lin et al., 2010 (blue) for satellite's trajectory (marked in lilac). Panel 3: solar wind dynamic pressure. Bottom panel: IMF total value (green), $B_{z\text{-}GSM}$ (yellow).

2.5.3 29-31 October 2003 (Event 3 of D4.1)

On 29-31 October 2003 (Halloween storm), several large solar events were observed which were followed by large geomagnetic storms. Due to the extreme values of the interplanetary parameters, there are large gaps in the OMNI data set (based on Geotail measurements). From the ACE spacecraft, α velocity, α density, and IMF (total and B_z) are available for all 3 days showing the large disturbances. However, proton velocity and proton density are provided only for the last 23 and 14 hours, respectively (see Fig. 2.8).

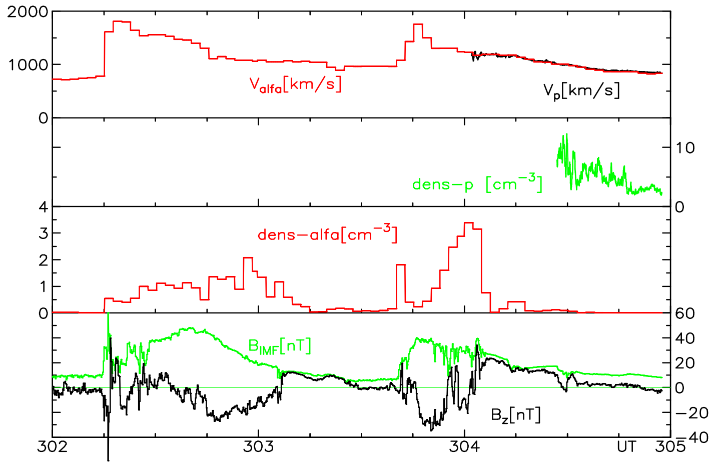

Figure 2.8 Interplanetary parameters measured by the ACE spacecraft on 29-31 October (doy 302-304) 2003.

Top panel: α velocity (red line) and proton velocity (black). Panel 2: proton density (green). Panel 3: α density (red). Bottom panel: IMF total (green) and B_z (black).

Both GOES10 and GOES12 were on the dayside in the afternoon hours of Universal Time on 29 and 30 October, and they spent several hours in the magnetosheath as the magnetosphere was compressed due to the large negative values of IMF B_z and supposedly large solar wind dynamic pressure. These events were widely discussed in several papers (e.g. Lopez et al., 2007; Dmitriev et al., 2005) in spite of the insufficient interplanetary data coverage.

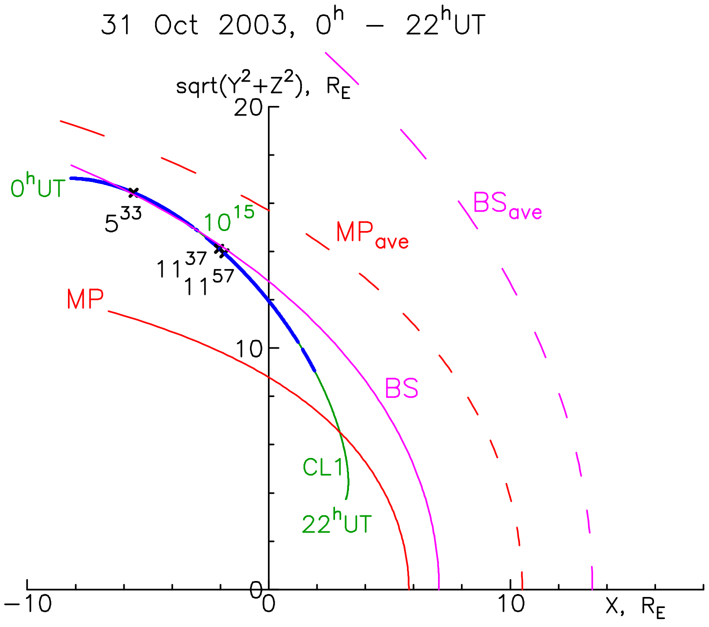

Figure 2.9 Cluster1 inbound orbit on 31 October in cylindrical coordinates. Sections in magnetosheath are marked in blue. Green sections: in magnetosphere. Dashed curves: model bow shock (lilac line) and magnetopause (red line) for average solar wind parameters, solid lines calculated with standoff distances $R_{BS0}=7R_E$ and $R_{MP0}=5.8R_E$. Times of bow shock crossings are marked in black, magnetopause inbound crossing at 10:15 is marked in green.

The four Cluster spacecraft observed several out- and inbound bow shock and magnetopause crossings on 31 October between 5:00 and 12:00 UT when the orbit was almost parallel to these discontinuities as seen in Fig. 2.9. The Cluster satellites were upstream of the bow shock from 5:33 to 5:43 UT, but they were in the magnetosphere from 9:52 to 10:02 UT and from 10:15 to 10:40 UT. Just 1 hour later, at 11:37 UT and at 11:57 UT, the Cluster satellites were upstream of the bow shock again for about 1 min in both cases. In the rest of the time, magnetosheath field was observed (marked in blue in Fig. 2.9).

As seen in Fig. 2.9, the possible displacement of the bow shock and the magnetopause from the average location to positions during large disturbances together with the geometry of the orbit can easily explain that the Cluster spacecraft could sample the interplanetary space, the magnetosheath, and the magnetosphere between 5:00 UT and 12:00 UT several times. From the times of the bow shock crossings observed by the four spacecraft, the velocity of the shock can be determined. Around 11:37 – 11:56 UT, the bow shock certainly stayed close to the satellites as there was no significant change in the interplanetary parameters (see Figs. 2.8 and 2.10). The inbound crossing followed the outbound crossing within about 1 min in both cases and the transit velocity was low, between 3 km/s and 17 km/s during the four crossings. The displacement of the bow shock was significantly faster at 5:33 and 5:42 UT when the velocity was about 430 km/s and 500 km/s, respectively. In that case, the bow shock supposedly moved far downstream of the position of the spacecraft due to rapid changes in solar wind parameters (the IMF did not change much at that time).

No proton density data are provided by any of the spacecraft monitoring the interplanetary field before about 11:00 UT, but magnetic field and proton velocity data are available from ACE for the whole time interval investigated here. Proton densities were estimated from the value of solar wind dynamic pressure provided by the best fitting bow shock model (Farris et al., 1991) and magnetopause model (Shue et al., 1998), respectively, based on the observed location of the discontinuities as shown below:

UT	s/c location	dyn. pres. [nP]	N_p [cm^{-3}]	R_{BS0} [R_E]	R_{MP0} [R_E]
5:33 – 5:43	upstream of BS	>95	>37	6.95	5.83
9:52 – 10:02	downstream of MP	<4.7	<2	10.9	9.1
10:15 – 10:40	downstream of MP	< 4.3	<2	11.6	9.26
at 11:37	at BS	>100	>50	6.8	5.6

The dynamic pressure values estimated from the bow shock crossings at 5:33 and 5:43 UT are in good agreement with the results of Dmitriev et al. (2005) who estimated solar wind dynamic pressure from magnetopause crossings of the LANL geosynchronous satellites. Unfortunately, there are no LANL data for the time interval 10 – 11 UT, and neither of the GOES satellites was around the nose of the magnetopause at that time.

Proton density data measured by ACE after 11 UT were propagated to the nose of the bow shock and together with solar wind velocity; they were used to determine dynamic pressure enabling model calculations for the bow shock position. The model of Farris et al. (1991) was used taking the bow shock standoff distance as R_{BS0} = 1.25 R_{MP0} where the magnetopause standoff distances were determined from the models of Shue et al. (1998) and Lin et al. (2010) shown by the red and blue curves in Fig. 2.10, respectively. Neither of the models provides a good prediction for the bow shock location at 11:37 and 11:57 UT, the difference in distance between model calculations and observations is larger than 2 R_E. As discussed above, the model of Farris et al. (1991) provides the observed bow shock locations when solar wind dynamic pressure is ~100 nT. According to ACE measurements, however, this parameter was about 4 times smaller.

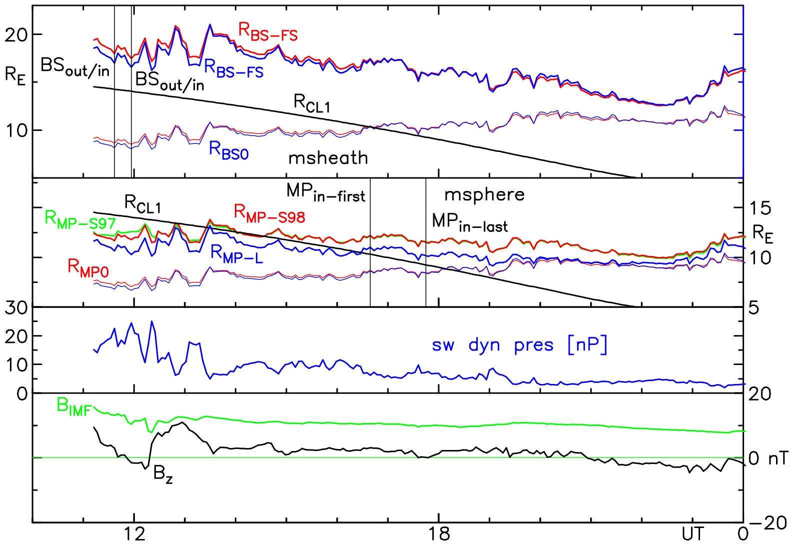

Figure 2.10 Top panel: model bow shock locations: Farris with Shue's R_{MP0} (red); Farris with Lin's R_{MP0} (blue), R_{BS0} standoff distances for Cluster1 trajectory (R_{CL1} in black). Panel 2: model magnetopause locations: Shue 1997 (green); Shue 1998 (red); Lin 2010 (blue line), R_{MP0} standoff distances for Cluster1 trajectory R_{CL1}. Panel 3: solar wind dynamic pressure. Bottom panel: IMF total (green), B_z (black curve). Interplanetary data are from ACE propagated to bow shock nose.

In Panel 2 of Fig. 2.10, the calculated magnetopause locations are presented. Black vertical lines indicate the first and last observed magnetopause crossing. The predictions of the 3D model by Lin et al. (2010) agree much better with the observations (difference in distance $< 0.5\ R_E$) compared to the results of the models by Shue et al. (1997) and Shue et al. (1998).

2.6 Summary and results

Cluster observations of the terrestrial magnetopause and the bow shock were presented here for 17 January 2005 and 31 October 2003 when these boundaries were unusually close to the Earth. The 2D model of Farris et al. (1991) with different standoff distances and the semi-empiric 3D model combined with MHD solution of Verigin et al. (2001, 2003) were used for calculating the bow shock location. The 2D models of Shue et al. (1997) and Shue et al. (1998), and the 3D model of Lin et al. (2010) were used for predicting the magnetopause location. The same models were applied for calculating the magnetopause distance for the geosynchronous orbit of the GOES satellites for 17 January 2005 and 20 November 2003. For the event on 17 January 2005, a full 3D MHD model was also applied using the BATS-R-US model at the Community Coordinated Modeling Center of NASA and the size and shape of the bow shock and those of the magnetopause were determined.

GOES12 magnetopause observations agreed better with the predictions of the 2D models of Shue et al. (1997 and 1998) on 17 January 2005 when dynamic pressure was very large, but B_z values were not extreme, the 3D model of Lin et al. (2010) slightly overestimated the displacement of the magnetopause towards the Earth. For 20 November 2003, however, when the north-south component of the IMF had extremely large negative values ($B_z < -40$ nT), the 3D model of Lin et al. (2010) provided the best prediction.

The Cluster spacecraft usually observed the bow shock and the magnetopause closer to the Earth than predicted by models. The best prediction for the magnetopause was provided by the 3D model of Lin et al. (2010) in every case. On 17 January 2005, the model of Farris et al. (1991) gave a good prediction for the bow shock location when the magnetopause standoff distance was taken from the model of Lin et al. (2010) to calculate the bow shock standoff distance.

Obviously, the full 3D MHD BATS-R-US model provided the best predictions for the location of the bow shock and the magnetopause. According to the results of this model, however, the magnetopause was a much thicker boundary than it was observed.

Conclusions: The three-dimensional asymmetric model of Lin et al. (2010) provides good predictions for the location of the magnetopause at higher geomagnetic latitudes and in case of extreme solar wind parameters. It is easy to use and fast compared to global 3D MHD modelling.

A three-dimensional model which is easy to use for determining the size and shape of the bow shock is also needed. It should take into account the shape of the 3D magnetopause in addition to the interplanetary parameters, as there are more and more spacecraft on polar orbit around the Earth and the cusp regions of the bow shock are often sampled.

3 Magnetospheric currents and Dcx – separating the contributions

3.1 Background

Geomagnetic storms are the most prominent disturbances in the Earth's magnetic environment (for a review, see, e.g., Gonzalez et al., 1994). They are characterized by a fast enhancement of the ring current, which is formed of energetic ions and electrons drifting around the Earth typically at radial distances of about 3-6 R_E (Earth radii). The energetic ions drift westward and the electrons eastward thus creating a westward net current. The enhancement of the ring current results from an increased rate of energy input from the solar wind into the magnetosphere, which is mostly due to enhanced reconnection at the dayside magnetopause during a steady southward interplanetary magnetic field. The dominant source of ring current particles is the nightside plasma sheet from where the particles are injected towards the Earth and energized by substorms and/or enhanced magnetospheric convection. During major magnetic storms the ionospheric oxygen ions can be the dominant ion species in the ring current (Daglis et al., 1997). After the energy input from the solar wind decreases sufficiently the loss processes of ring current particles start to dominate and the ring current begins to decay. The most important loss processes for ring current particles are collisions with neutral particles of the geocorona (extension of Earth's neutral atmosphere into space), convective losses where the energetic particles drift on open trajectories and escape through the dayside magnetopause, and wave-particle interactions which scatter energetic particles into the atmosphere.

The Dst index (Sugiura and Kamei, 1991) was developed to measure the average reduction of the horizontal magnetic field component on the ground caused by the ring current. According to the Dessler-Parker-Sckopke (DPS) relation (Dessler and Parker, 1959; Sckopke, 1966) the magnetic field created by the ring current on the ground is directly proportional to the total kinetic energy contained within the ring current. Thus, if the disturbance measured by the Dst index is purely caused by the ring current the index can be considered as a direct proxy for the ring current energy.

However, it has been known for a long time that the Dst index is contaminated by the magnetic effect of other major magnetospheric and ionospheric current systems, as well as currents induced within the Earth. Several early studies of the Dst index (see, e.g., Burton et al., 1975) have pointed out that the currents flowing at the dayside magnetopause produce a northward magnetic field on the ground and thus give a positive contribution to the Dst index that is roughly proportional to the square root of the solar wind dynamic pressure. The effect of the magnetopause currents is typically seen as an increase in Dst, often to highly positive values, when the solar wind dynamic pressure is rapidly enhanced due to a solar wind disturbance (e.g., a shock wave related to a coronal mass ejection or to a corotating interaction region). Before using Dst as a true measure of the ring current one has to correct it for the effect of the solar wind pressure by removing the contribution of the magnetopause currents. One of the most used expressions for the magnetopause contribution to Dst is given by O'Brien and McPherron (2000) as $b\sqrt{P_{SW}} - c$ where P_{SW} is the solar wind dynamic pressure, b=7.26 nT/nPa$^{1/2}$ and c=11 nT. In addition to the magnetopause current, the Dst index has been shown to include a significant contribution from the magnetotail current, especially during large storms (e.g., Kalegaev et al., 2005, Tsyganenko and Sitnov, 2005 and Ganushkina et al., 2004). Turner et al. (2000) concluded that for small storms about 25% of the peak Dst value is caused by the tail current. However, this is only a rough average value, which can not be used to correct the Dst index for tail current effects.

As mentioned above, the Dst index (after the contributions from other current systems have been removed) is a widely used indicator of the ring current intensity and inner magnetospheric energy content. Therefore, it is an important tool in monitoring the development of magnetic storms. However, the official Dst index has been shown to contain both random and systematic errors (Karinen et al., 2002; Karinen and Mursula, 2005, 2006; Mursula and Karinen, 2005; Mursula et al., 2008, 2010). Among the systematic errors are the incorrect latitude normalization of the station disturbances, the excessive seasonal variation, and the unequal weighting of the individual stations in the index. A version of the Dst index called the Dcx index, which has been corrected for these errors, has been developed at the University of Oulu (UOulu).

3.2 Monitoring the tail current

In order to monitor the dynamics of the tail current and to evaluate its effect on the Dcx index we have constructed a proxy describing the intensity of the tail current at any given time. The pitch angle distribution of energetic particles measured at low-altitude satellites provides information about the configuration of the magnetic field. In the inner magnetosphere where the field lines are roughly dipolar the pitch angle distribution of energetic particles at low altitudes is typically anisotropic with more particles observed at 90^o pitch angle than at 0^o and 180^o. However, at slightly higher L-shells (especially in the magnetotail) where the field lines are highly stretched due to a strong cross-tail current sheet, the energetic particle distribution is isotropic. This is due to strong pitch angle scattering in the highly curved field lines of the tail current sheet (Chen, 1992; Sergeev and Tsyganenko 1982). Accordingly, while the pitch angle distribution is typically anisotropic at low L-shells, it becomes isotropic poleward of a rather sharp boundary which is called the isotropic boundary (IB).

The IB location can be monitored using energetic particle observations at the low-altitude polar orbiting NOAA/POES satellites. These satellites are sun-synchronous with an altitude of about 850 km. The MEPED instrument onboard the NOAA/POES satellites measures energetic particles above 30 keV. MEPED contains two orthogonally directed detectors that measure the particle flux in local horizontal direction (0^o detector) that points radially away from Earth and in the local azimuthal direction (90^o detector) that points antiparallel to spacecraft velocity. Although the pitch angles of the detectors change along the orbit the IB can easily be detected by comparing the fluxes of these two orthogonal detectors. Similarly as Sergeev et al. (1995) we have identified the IB by measuring the corrected geomagnetic latitude (CGMLat) where the normalized difference of the count rates of the two orthogonal detectors measuring 80 keV protons drops below a threshold value of 0.15, i.e., $(I_{90} - I_0)/(I_{90} + I_0) < 0.15$.

It is important to note that the proton detectors in the MEPED detectors degrade in time due to radiation damage, leading to erroneously low measured fluxes already some 2 years after the satellite launch. Asikainen and Mursula (2010) have recently made an extensive study of the effect of radiation on these detectors and introduced a set of calibration factors that must be used to correct the MEPED fluxes of all NOAA/POES satellites, covering 30 years of energetic particle observations. The correction of MEPED fluxes is also relevant for the determination of the IB location since the 0^o and 90^o detectors do not degrade at the same rate (typically the 90^o detectors degrade faster). This difference distorts the flux ratios determining the IB. Without flux correction, the IB location would shift poleward in time and, after sufficient degradation, the IB would not be observed any longer. For a more detailed discussion on the correction of radiation damage effects on NOAA/MEPED detectors see Section 6.2.

The usefulness of the IB location as an indicator of the tail current was demonstrated by Sergeev et al. (1993) who showed that the IB latitude measured by the MEPED instruments correlates very well with the magnetic field direction measured by GOES near the tail current sheet. The magnetic inclination angle in the tail near the current sheet decreases as the measured IB latitude decreases, i.e., when the magnetic field becomes more stretched, the IB shifts to lower latitudes. Since the inclination angle is proportional to the current intensity, the IB latitude reflects the intensity and location of the magnetotail current sheet. However, as Sergeev et al. (1993) and Sergeev et al. (1995) showed, the IB location varies with magnetic local time (MLT), being generally at lower latitudes at midnight and shifting to higher latitudes towards the evening and morning sectors. Sergeev et al. (1995) used one month of NOAA-6 data to determine the MLT dependence of the IB latitude. They constructed a measure of the tail current, the so called MT-index, by removing the MLT dependence from the measured IB latitudes. Asikainen and Mursula (2010) used the corrected fluxes of NOAA-15, 16, 17 and 18 satellites in 1999-2007 to determine the MT-index. They separately determined the IB location for the northern and the southern hemispheres and found that the MLT variation of the boundary is best removed by the following expressions

$$MT_N = \lambda_{IB,N} - 3.49\left[1-\cos\left(\frac{\pi}{12}(MLT-23)\right)\right]$$

$$MT_S = \lambda_{IB,S} - 3.40\left[1-\cos\left(\frac{\pi}{12}(MLT-23)\right)\right] - 0.09^{\circ}$$

where the MT_N and MT_S are the MT indices for the northern and southern hemispheres, and $\lambda_{IB,N}$ and $\lambda_{IB,S}$ denote the measured IB CGMLat latitudes for the two hemispheres. The offset value of -0.09° in MT_S depicts an average systematic difference between the northern and southern MT values. Finally, the average hourly MT value was calculated by taking the average of all northern and southern MT values measured between 18 and 06 MLT in each UT hour.

3.3 Model for the Dcx index

UOulu has also studied the dynamics of the Dcx index and developed a new semi-empirical model that is capable to determine the individual contributions of ring current, tail current and magnetopause current to the Dcx index (Asikainen et al., 2010). In the model we express the Dcx index as a sum of contributions from the ring, tail and magnetopause currents and a constant offset c, i.e., $Dcx=D_{RC}+D_T+D_{MP}+c$. Following the work of Burton et al. (1975) and O'Brien and McPherron (2000) we describe the time evolution of the ring current with a differential equation

(Eq. 3.1) $$\frac{dD_{RC}}{dt} = Q - \frac{D_{RC}}{\tau}$$

where Q describes injection of energy into the ring current (in units of nT/h) and τ is the ring current decay time.

Combining the expression for the Dcx index with this differential equation yields the model equation

(Eq. 3.2) $$\frac{dDcx}{dt} = Q + \frac{c}{\tau} - \frac{Dcx}{\tau} + \frac{D_{MP}}{\tau} + \frac{D_T}{\tau} + \frac{dD_T}{dMT}\frac{dMT}{dt} + \frac{dD_{MP}}{d\sqrt{P_{SW}}}\frac{d\sqrt{P_{SW}}}{dt}$$

where we have assumed that the tail current contribution is a function of the MT index and the magnetopause contribution is a function of the square root of solar wind dynamic pressure. We also assumed that Q and τ are functions of the solar wind dawn-dusk electric field and solar wind dynamic pressure. The unknown model parameters and functions (Q, τ, D_T, D_{MP} and c) can be determined using advanced inversion methods and measured data. The time interval studied here (1.1.1999-31.12.2007) contains the most active time of solar cycle 23 as well as most of its descending phase, being ideally suited to study the solar wind magnetosphere connection during very different levels of geomagnetic activity and solar wind conditions. The hourly solar wind and IMF data were obtained from the OMNI2 database (http://omniweb.gsfc.nasa.gov). We used the MT index constructed as described above, and the most recent version of the hourly Dcx index. The time derivatives appearing in the model equation were computed from the hourly values using the symmetric two-point formula for the numerical derivatives, i.e., $y'[i] = (y[i+1] - y[i-1])/2$.

In the analysis of Equation 3.2 we have applied the local linear regression which is a non-parametric estimation method. In the case of a simple regression $y=ax+b+\varepsilon$ (y=response variable, x=explaining variable and ε=random error) the idea is to consider the unknown regression parameter functions a and b within small ranges of the variable they depend on, i.e., a third variable z. The parameter functions can be approximated as Taylor series around some point $z=z_0$, e.g., $a(z)=a(z_0)+a'(z_0)(z-z_0)$. Then the regression equation becomes $y=a(z_0)x+a'(z_0)(z-z_0)x+b(z_0)+b'(z_0)(z-z_0)+\varepsilon$ which can be solved for constants $a(z_0)$, $b(z_0)$ and the corresponding derivatives $a'(z_0)$ and $b'(z_0)$ using standard linear regression and assuming that these remain constant when the data points used in the regression are chosen so that the values of z are close to z_0. Repeating the regression for several different values of z_0 we can obtain the parameters a and b as functions of z. In practice the data points in the regression are weighted by an amount that depends on how much their z values deviate from z_0. We used the tri-cube window

$$w(z)=\left(1-\left|2\frac{z-z_0}{W}\right|^3\right)^3 \text{ for } |z-z_0|\le\frac{W}{2}$$

$$w(z)=0 \text{ otherwise}$$

to compute the weights where W is the length of the window determining the data points to be included in the regression.

We now assume that in Equation 3.2 the explaining variables are Dcx and the time derivatives of MT index and $\sqrt{P_{SW}}$, while the response variable is the time derivative of Dcx. Applying the local linear regression for a range of MT values we obtain, among other things, the derivative of the tail current contribution with respect to MT index (dD_T/dMT**)**. Integrating the estimated derivative numerically gives the tail current contribution D_T. The coefficient of integration was set so that D_T=0 for MT=75.5° (maximum MT value observed). Figure 3.1 shows the estimated derivative (left) and D_T (right) with corresponding error estimates. The right side plot also includes the following fit to D_T:

$$D_T(MT)=-5.495\times10^7\left[\frac{1}{\cos^2 MT}+2.633\right]^{-7.871}, \text{ when MT} \le 75.5^{\circ}$$

$$D_T=0, \text{ otherwise}$$

The most striking feature of the D_T function is its large range extending from 0 nT to about –160 nT. This indicates that the tail current can cause a very significant contribution to the Dcx index.

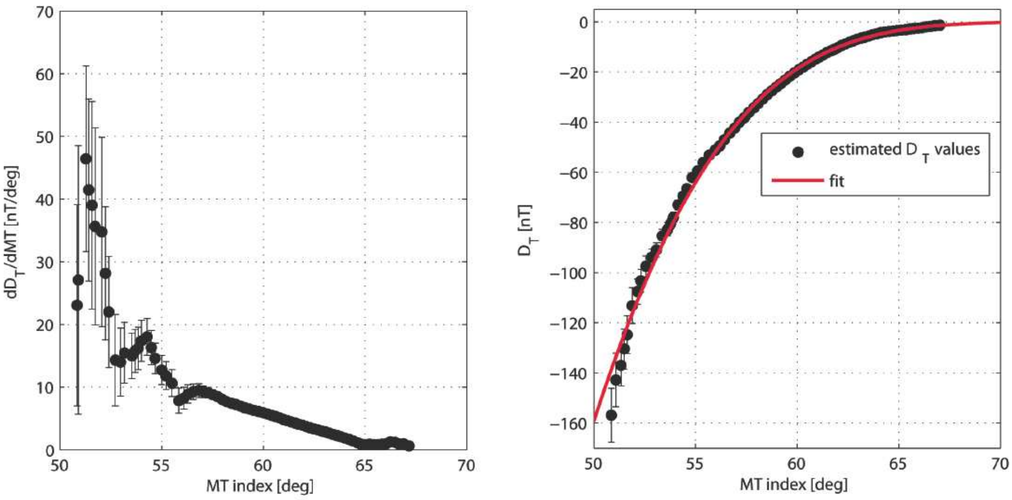

Figure 3.1 Left: Derivative dD_T/dMT as a function of MT index. Right: Tail current D_T as a function of MT index.

After estimating the tail current contribution we can now transform the model equation to a simpler form

$$\frac{d(Dcx - D_T)}{dt} = Q + \frac{c}{\tau} - \frac{(Dcx - D_T)}{\tau} + \frac{D_{MP}}{\tau} + \frac{dD_{MP}}{d\sqrt{P_{SW}}}\frac{d\sqrt{P_{SW}}}{dt}$$

and use local linear regression to estimate the magnetopause current contribution similarly as above for the tail current contribution.

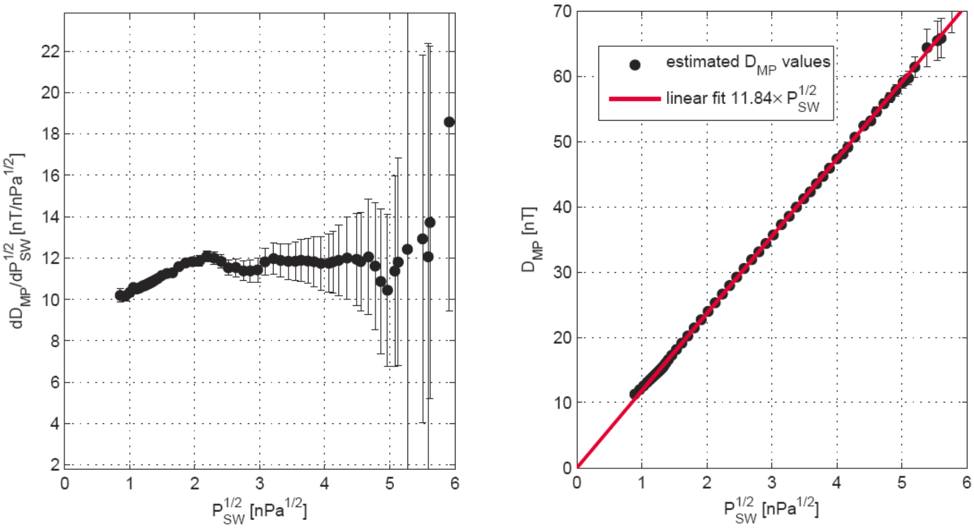

Figure 3.2 Left: Derivative $dD_{MP}/d\sqrt{P_{SW}}$ as a function of $\sqrt{P_{SW}}$. Right: The magnetopause current D_{MP} as a function of $\sqrt{P_{SW}}$.

Figure 3.2 shows the magnetopause current contribution D_{MP} (right side) and its derivative (left side). The right side confirms the well known fact that the magnetopause contribution is a linear function of the square root of the solar wind dynamic pressure.

Finally, knowing D_{MP} we can transform the model equation into the following form

$$\frac{d(Dcx - D_T - D_{MP})}{dt} = Q + \frac{c}{\tau} - \frac{(Dcx - D_T - D_{MP})}{\tau}$$

which allows us to estimate the ring current energy injection function Q and decay time τ by using local linear regression. In this case the slope of the regression is $-1/\tau$ and the intercept term (to be called β) corresponds to $Q+c/\tau$. After experimenting with several combinations of solar wind electric field and dynamic pressure as the controlling variable we found that the combination $E_{SW} P_{SW}^{1/6}$ produced the best results.

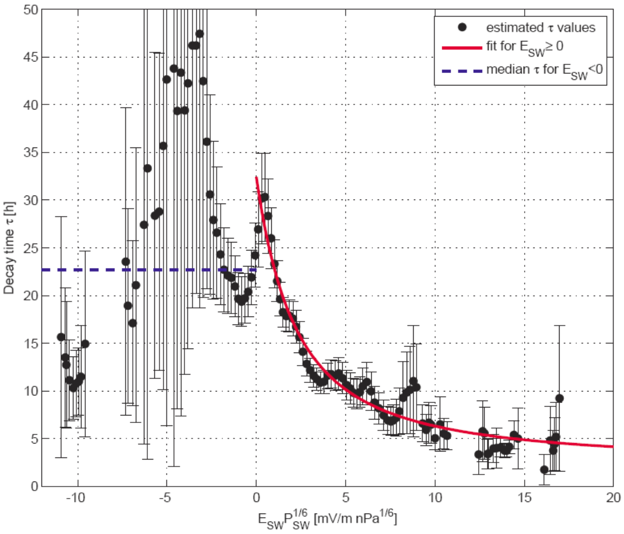

Figure 3.3 Ring current decay time τ as a function of a combination of solar wind electric field and dynamic pressure. The plot also shows the fit for positive electric field (southward IMF) and constant τ for negative electric field (northward IMF), as depicted in Equation 3.3.

For positive electric field values (southward IMF) we found that the decay time decreases with increasing electric field and solar wind dynamic pressure. The decay time is best described by the function

(Eq. 3.3)
$$\tau = 2.031 \exp\left(\frac{19.199}{6.929 + E_{SW} P_{SW}^{1/6}}\right), \text{ for } E_{SW} \geq 0$$
$$\tau = 22.7 \text{ h, for } E_{SW} < 0.$$

The decay time and the corresponding fit, as depicted in Equation 3.3, are shown in Figure 3.3.

The energy injection function Q can be determined from the intercept β of the local linear regression, $Q=\beta-c/\tau$. Assuming that for negative solar wind electric field Q=0, one can obtain the average value c=$\beta\tau$=–6 nT, after which the function Q is known. We found that Q is best described by the function

(Eq. 3.4)
$$Q = -1.23\left(E_{SW} P_{SW}^{1/6}\right)^{1.283}, \text{ for } E_{SW} \geq 0$$
$$Q = 0, \text{ for } E_{SW} < 0.$$

The estimated ring current energy injection function and the corresponding fit, as depicted in Equation 3.4, are shown in Figure 3.4.

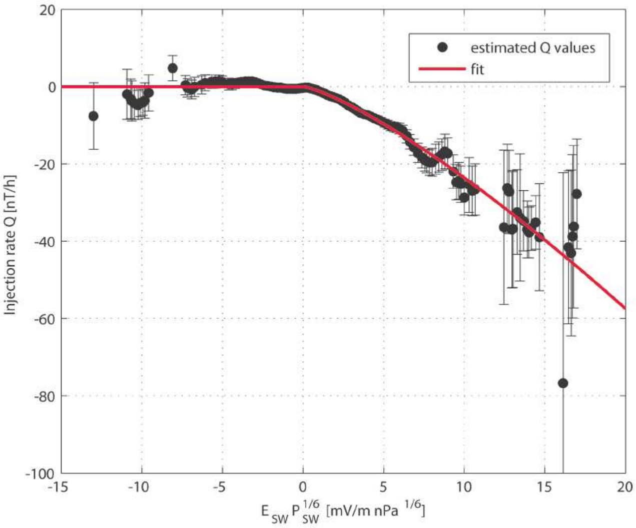

Figure 3.4 Ring current energy injection function Q and the fit, as depicted in Equation 3.4.

After estimating all the model parameters the modelled ring current contribution D_{RC} (model) can be estimated by numerically integrating the Equation 3.1 by the 4th order Runge-Kutta algorithm using the functions given in Equations 3.3 and 3.4. On the other hand, the true ring current contribution can also be directly estimated from the measured Dcx index by removing the estimated contributions of the other two current systems. This gives us the true experimental ring current contribution, also called here the purified Dcx index, $Dcx^{*}=Dcx-D_{T}-D_{MP}-c$.

We computed a model Dcx index using the modelled ring current contribution D_{RC}(model) in Dcx(model) = D_{RC}(model)+D_{T}+D_{MP}+c, and compared this with the original measured Dcx index. The comparison is shown at the left side of Figure 3.5. The correlation coefficient between the two indices is 0.904 and the RMS deviation is 10.1 nT. One can see that the variance of the model Dcx is roughly the same for all levels of activity and there is no bias in the model for Dcx>–200 nT. For Dcx<–200 nT the model seems to slightly overestimate the disturbance level of the index.

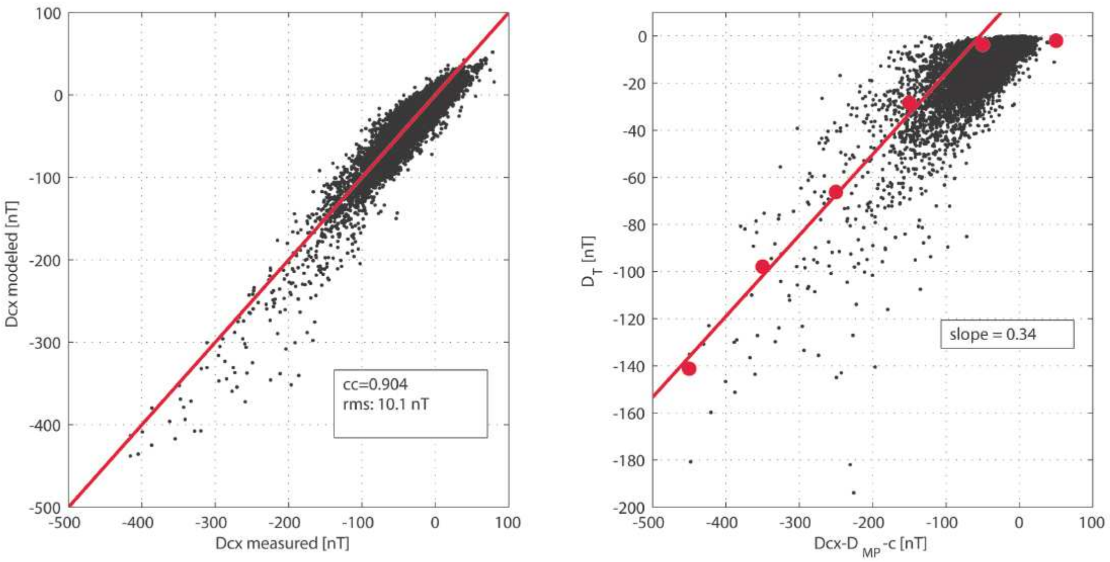

Figure 3.5 Left: The Dcx (model) index vs. the measured Dcx index. Right: The tail current contribution vs. the pressure and offset corrected Dcx index.

The right side of Figure 3.5 shows the tail current contribution compared with the pressure and offset corrected Dcx. The red circles denote the median D_T values within 100 nT wide bins and the line is a fit to these median values. One can see that there is a roughly linear relation between the pressure and offset corrected Dcx and the tail current contribution although the scatter in the tail current contribution is very large. The slope of the linear fit is 0.34 which indicates that on average about 34% of the pressure corrected Dcx is caused by the tail current. However, it is important to note that during any individual storm the relative contribution of the tail current can vary a lot since the time evolutions of the ring current and the tail current are generally different. This average percentage is somewhat larger than previous estimates (e.g., Turner et al. 2000) of about 25% for smaller storms.

3.4 A few case studies

The top panel in Figure 3.6 shows the different contributions to the Dcx during the widely studied storm of 31 March 2001 (see, e.g., Asikainen et al., 2005), including the model ring current contribution D_{RC} (model), the tail current, the magnetopause current as well as the measured, modelled and purified Dcx indices. For comparison, the middle panel of Fig. 3.6 shows the solar wind pressure, density and velocity, and the bottom panel shows the solar wind dawn-dusk electric field. One can see that during this major storm the model reproduces the observed Dcx rather well. The largest deviation by about 80 nT (with model Dcx below observed Dcx) occurs during the secondary enhancement of the Dcx in the latter half of 31 March. There is some similar systematic deviation during the storm recovery phase. By far, the largest contribution to the Dcx index during this storm comes from the ring current. However, the tail current contribution is also quite large, reaching up to -130 nT. Note also how the tail current contribution rapidly increases during the storm main phase but also starts to first level off and then drop back very fast, even before the storm recovery begins, reacting to changes in both the solar wind pressure and the solar wind electric field very sensitively.

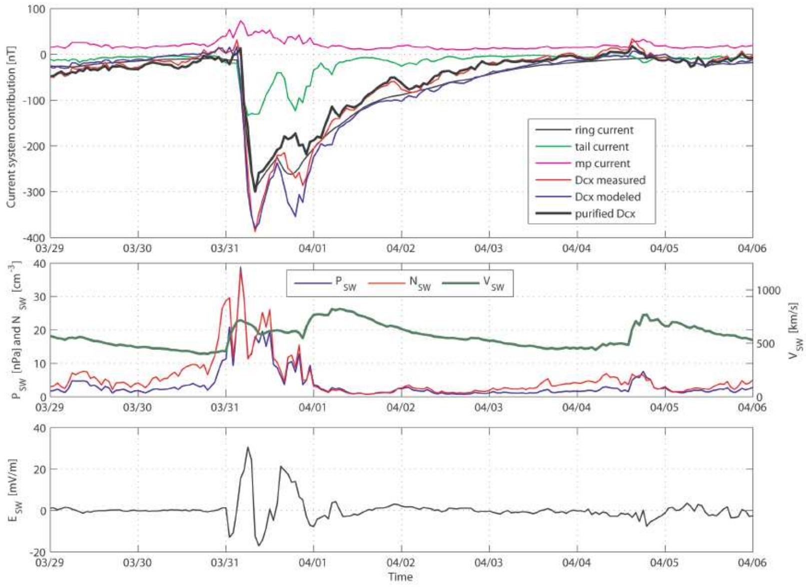

Figure 3.6 Top panel: Contributions of the different current systems to Dcx during March 29 - April 5, 2001: modeled ring current (thin black line), tail current (thin green line), magnetopause current (thin magenta line), measured Dcx (thin red line), modeled Dcx (thin blue line), purified Dcx (thick black line). Middle panel: solar wind pressure (P_{SW}, thin blue line), density (N_{SW}, thin red line) and velocity (V_{SW}, thick green line). Note that the pressure and the density have the same numerical scale.

The purified Dcx, which is a more reliable estimate for the ring current, is smaller in magnitude than the Dcx index during main and early recovery phase, with the largest difference of about 100 nT found during the secondary enhancement of the Dcx. During the quiet times and during the later recovery phase the purified Dcx and the measured Dcx indices agree well. This indicates that the strongest contributions of the tail and magnetopause currents to Dcx are mainly restricted to the storm main phase and early recovery phase. We note that the contributions of the ring, tail and magnetopause currents to the Dst index have earlier been modelled for this storm using an analytic model of the magnetospheric current systems parameterized by solar wind/IMF conditions (Kalegaev et al., 2006). The time development of the tail current in their model shows the same fast variations as here. Also the maximum contribution of the tail current to Dst was about -100 nT in that model, which is rather close to the maximum value found here.

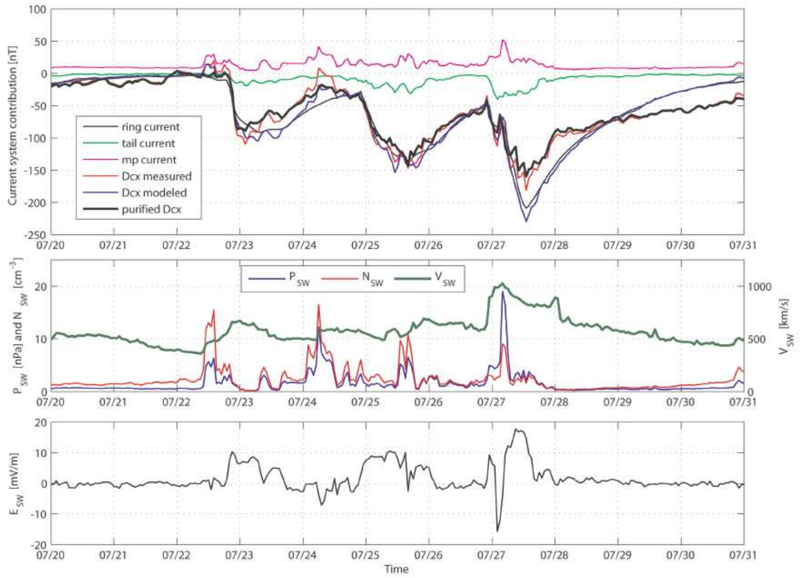

Figure 3.7 Top panel: Contributions of the different current systems to Dcx during July 20-31, 2004. Panels and notations as in Fig. 3.6.

Figure 3.7 shows the different Dcx contributions and the solar wind parameters during the three-storm period of 22-30 July, 2004. In this case the contribution of the tail current remains quite small (below -50nT) throughout the event and is largely cancelled out by the magnetopause current. The modelled Dcx roughly follows the measured Dcx until the last enhancement on 27 July when the magnitude of the modelled Dcx seriously overestimates the measured Dcx index by about 65 nT. During the last recovery phase the model also fails by first overestimating and then underestimating the observed Dcx. Interestingly, during the three successive storms the solar wind density decreases while the velocity increases especially during the last storm main phase to over 1000 km/s compared to the speed of about 600 km/s during the first two storms. This indicates that the model injection term Q, whose magnitude is severely overestimated during the third storm, probably depends on solar wind velocity, density and IMF B_Z in a more complicated way than given by the functional relationship suggested above. A probable explanation is that the near-Earth space including the ionosphere is significantly preconditioned by the two previous storms in a way which our model, based on simultaneous values of the Dcx, MT and solar wind parameters, fails to capture. One effect of such preconditioning could be that the plasmasheet and/or ionospheric source population of ring current ions is significantly depleted by the time the third main phase starts. It is likely that the diminished solar wind density (which partly controls the plasmasheet density) limits the injection term in the last storm. We note that we also tried to find an injection function and decay time that explicitly depend on solar wind density. However, all such functions produced a slightly smaller correlation coefficient and larger RMS error between the model and the measured Dcx than the dependence presented above. Accordingly, solar wind pressure seems to be, overall, a more important factor in determining the ring current injection and decay than solar wind density, emphasizing the unique conditions during the final main phase of the three-storm event of Fig. 3.7.

4. Solar wind energy input and partitioning

The solar wind energy input into the magnetosphere is well known to be strongly enhanced during periods of southward interplanetary magnetic field. Large scale magnetic reconnection occurs at the dayside magnetopause during these times, transporting magnetic flux and solar wind plasma to the magnetospheric tail lobes where energy is stored mostly in the form of magnetic energy (e.g., Akasofu, 1981). Some of this energy is released during substorms, enhancing field aligned currents which close through the auroral ionosphere, increase particle precipitation into the ionosphere and cause energetic particle acceleration and injection into the inner magnetosphere. We have studied different aspects of this energy cycle within the magnetosphere and discuss briefly how the solar wind affects the energy injection and dissipation, e.g., in the ring current as viewed by the Dcx index and energetic proton observations by the NOAA/POES satellites, and in the ionosphere where the energy is dissipated as Joule heating by field aligned currents closing through the ionosphere.

4.1 Ring current and energetic particles

In Section 3 we discussed the model that separates the contributions to the Dcx index from the ring, tail and magnetopause currents. We also determined there the functions that describe energy injection into the ring current and ring current decay time. As discussed above, the ring current energy injection function (Eq. 3.4) and the ring current decay time (Eq. 3.3) are best described in the model by the product of solar wind electric field and solar wind pressure (to the power 1/6). The effect of pressure in energy injection becomes most visible during great magnetic storms where energy injection functions based only on solar wind electric field fail to correctly reproduce the Dcx (or Dst) index during the main phase. So, on the basis of the Dcx index study described above we conclude that while the dominant factor causing energy injection into the ring current is the solar wind electric field, the injection of energy further enhanced during times of strong solar wind pressure.

As another aspect of the solar wind-magnetosphere energy coupling we have studied the energetic proton fluxes observed by low-altitude NOAA/POES satellites. The NOAA/MEPED energetic proton dataset calibrated by UOulu (see Section 6.2) is currently one of the longest uniform particle datasets in space physics, covering nearly three solar cycles from 1978 to present. Using this dataset we have calculated daily averages of 80-250 keV protons using observations of the NOAA-6, 7, 8, 10, 12, 15, 16, 17, 18, 19 and METOP-02 satellites at any local time sector. In order to remove the effect of the South Atlantic Anomaly, above which the particle fluxes are greatly enhanced (see, e.g., Asikainen and Mursula, 2008), we excluded the data from L-shells below L=2 and from geographic longitudes between -50^o and $+50^o$ in the southern hemisphere.

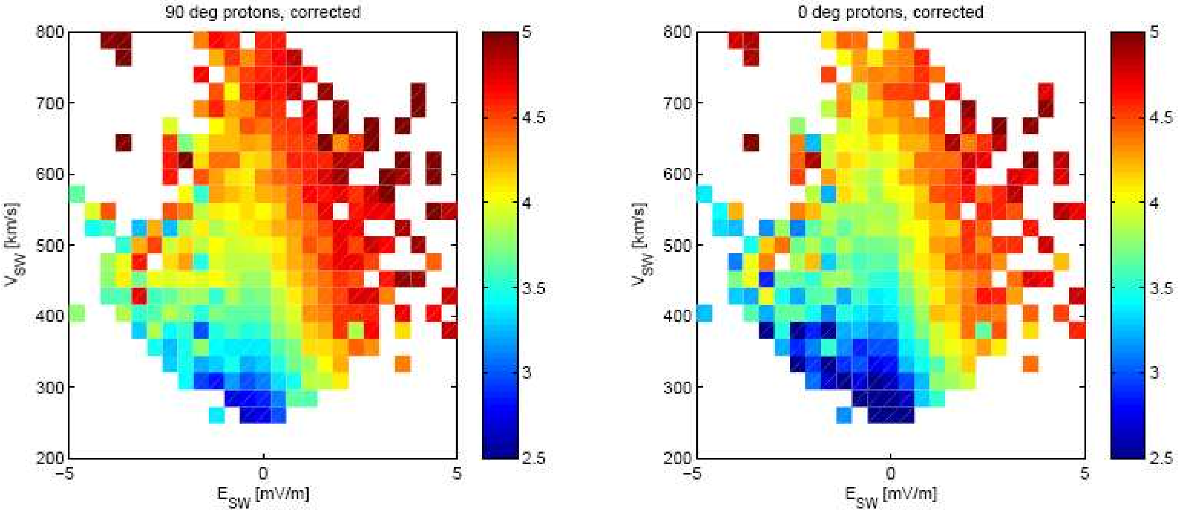

Figure 4.1 Daily averages of corrected proton fluxes in the 90^o (left) and 0^o (right) direction as a function of solar wind electric field and solar wind speed.

Figure 4.1 shows the daily averages of the corrected proton fluxes in 90^o (left) and 0^o (right) direction as a function of daily averaged solar wind electric field and solar wind speed (for explanation of detector directions see Section 6.2.1). As the ring current energy injection function, the fluxes strongly depend on the solar wind electric field. For a fixed solar wind speed and positive electric field (southward IMF), the fluxes increase strongly with electric field. The fluxes also depend independently on solar wind speed. For a constant value of electric field the fluxes increase with increasing solar wind speed. Even for northward IMF (negative electric field) the fluxes increase as a function of solar wind speed. However, for northward IMF and constant solar wind speed, the fluxes stay relatively constant as a function of electric field. Although it is possible that the negative values of daily solar wind electric field contain short intervals where the IMF is southward, the effect of such intervals can hardly produce the systematic distribution of fluxes depicted in Fig. 4.1. Most flux values for negative electric fields and $V_{SW} > 450$ km/s are as high as those observed during similar speeds but positive electric field values. It is very unlikely that a few short periods of southward IMF embedded within the negative daily averages of electric field would cause such a systematic pattern of high fluxes during high solar wind speeds. Therefore, it seems more probable that large values of solar wind speed (high-speed solar wind streams) can cause enhancements in low-altitude proton fluxes even during periods of northward IMF.

4.2 Field-aligned currents, high-latitude ionospheric currents and Joule heating

Large scale currents, on the order of a few MA, driven by the solar wind, follow the geomagnetic field lines to the ionosphere where they close, depositing energy in the form of Joule heating ranging from a few of GW during quiet times to around a TW during the largest magnetic storms. The field-aligned currents (FACs) are easily observed by low-earth-orbiting magnetic field observing satellites such as the Ørsted and Champ satellites, the latter now sadly deceased, and the upcoming Swarm satellites. The most direct observations of the field-aligned currents occur when the satellites fly directly through them, giving rise to strong perturbations mainly in the magnetic east component, due to the arrangement of the currents along magnetic latitudes. One way to derive the FACs has therefore been to assume infinite current sheets and compute the current density directly from dB/dx with x going along magnetic longitude. A number of versions of this approach exist the first being Iijima and Potemra (1976). Another approach is statistical, collecting data for many passes where solar wind conditions are similar, and then deriving the full field-aligned current system. Both methods have their drawbacks, the first method only uses one of the magnetic field components, albeit the most important, while the second assumes that like solar wind conditions give like field-aligned currents causing sharper details to be smoothed out.

We will here give the first results of a method that utilizes the full 3-d magnetic field perturbations observed from single passes of LEO satellites to derive the large scale structure of the FAC system. We parameterize the field-aligned currents and solve the potential equation in the ionosphere, thereby closing the current system. The ionospheric currents contribute significantly to the magnetic perturbations, particularly of the field-aligned component which is hardly perturbed by the FACs. As a bonus the solution of the ionospheric potential equation immediately gives us the ionospheric Joule heating. We use the magnetic observation from Ørsted and Champ. Unfortunately, the star camera on Ørsted has had a tendency to fall out during magnetic storms, and the only event chosen for examination by the SOTERIA WP4 group for which there exist both Ørsted and Champ data is the November, 2003 event. Even for this event, Ørsted data are missing at the height of the storm.

4.2.1 The method in brief

1) Parameterize field-aligned currents
2) Close current system in the ionosphere with given ionospheric conductance
3) Compute magnetic perturbations from the full current system at satellite track
4) Compare to observed magnetic perturbations by satellites
5) Fit FAC parameters using least squares
6) Compute ionospheric Joule heating

4.2.2 Parameterization of field-aligned currents

We have divided the field-aligned currents (FACs) into 8 segments: Region 1/2, day/night, and dawn/dusk, plus an additional Region 0 current. Each segment is described by 6 parameters: MLT start/end, cgm-latitude start/end, width in latitude, and current density. In total 54 parameters for the 9 segments. The number of parameters is cut to 36 by enforcing that Region 1 and 2 currents are adjacent and that the day and night sectors must be connected. Figure 4.2 shows an example. Such a relatively crude parameterization does of course not capture the full variations of field-aligned currents, but it delivers the important differences in strength and position in the various sectors.

4.2.3 Closing current system in the ionosphere with given ionospheric conductivity

The FACs flow freely along the magnetic field lines above the ionosphere. In the higher density of the ionosphere the currents close according to the ionospheric conductivity. To derive the ionospheric currents we have to solve for the ionospheric potential Φ (in a flat spherical shell) (Vennerstrom et al., 2004):

$$\nabla \cdot \Sigma^T \cdot \nabla\Phi = -j_{par} \sin I$$

where I is the magnetic field line inclination, j_{par} is the field aligned currents, and Σ^T is the ionospheric conductance tensor. Σ^T depends on the Pedersen and Hall conductances, Σ_P and Σ_H:

$$\Sigma^T = ((\Sigma_{\theta\theta}, \Sigma_{\theta\lambda}), (\Sigma_{\theta\lambda}, \Sigma_{\lambda\lambda})); \Sigma_{\theta\theta} = \Sigma_P/\sin^2 I; \Sigma_{\theta\lambda} = \Sigma_H/\sin I; \Sigma_{\lambda\lambda} = \Sigma_P$$

where θ is the magnetic co-latitude and λ is the magnetic longitude. The horizontal ionospheric currents are then given by:

$$j_\perp = (j_\theta, j_\lambda) = \Sigma^T \cdot (-\nabla\Phi).$$

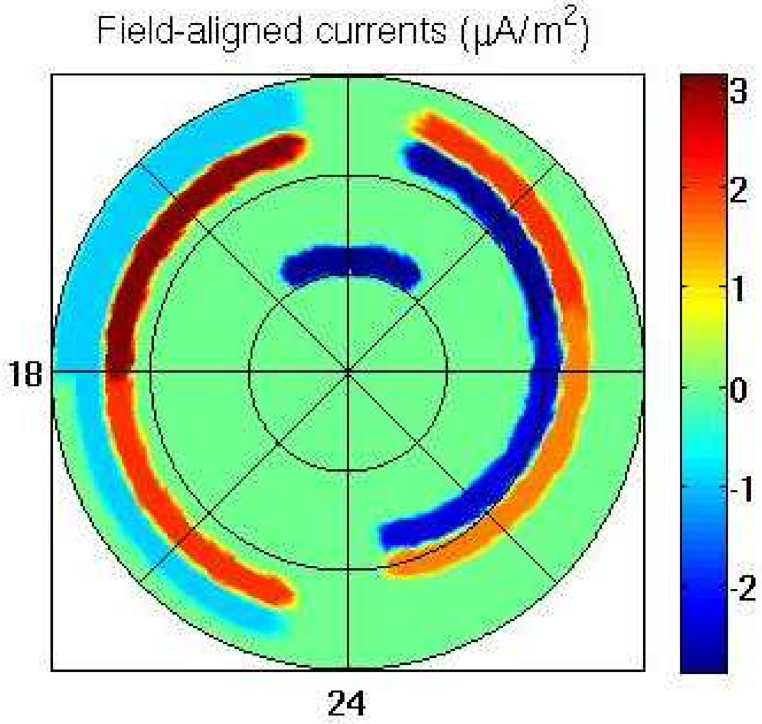

Figure 4.2 Parameterization of the field aligned currents. The currents are seen in a polar plot down to 60^o corrected geomagnetic (cgm) latitude, and in magnetic local time (MLT) with midnight at the bottom.

4.2.4 Ionospheric conductances and TEC maps

An integral part of this procedure is the height integrated Pedersen and Hall conductances, which primarily depend on solar irradiation (on the day side) and precipitating particles (mainly in the auroral region). Moen and Brekke (1993) derived the solar dependence based on the F10.7 measurements. An example of the conductance dependence on precipitating particles is given by Hardy et al. (1987) based on the Kp index. In this work we will use the Moen and Brekke solar dependence, but for the precipitating particles dependence we will utilize the Total Electron Content (TEC) maps developed from GPS data (for detailed description see Section 5.2). Conductances are not readily derived from TEC values, since the majority of the electrons are in the F layers, while the ionospheric currents run in the D and E layers of the ionosphere. It is clear though, that higher TEC values must influence ionospheric conductances. The TEC maps have a background level of non-disturbed TEC values on the night side away from the auroral oval. The ionospheric conductances have a similar background level. We have fitted these two background levels to match each other with the result that $\sum_{\text{particles}} = 0.66*\text{TEC}$.

Figures 4.3a and 4.3b show the ionospheric Pedersen conductance around noon UT on November 20, 2003 based on F10.7 only and on F10.7 with TEC, respectively. A background conductance of 5 Ω^{-1} is assumed.

4.2.5 Computing magnetic perturbations from the full current system at satellite track

From the full field-aligned/ionospheric current system the magnetic perturbations can be derived at any point directly from Biot-Savart's law. However, this is computationally very heavy, since it involves integrating the current density over the entire 3-dimensional source region for each point where we wish to compute the magnetic field. A faster method, the Poloidal-Toroidal Decomposition Method, was developed by Engels and Olsen (1998). The current density is given on a spherical grid, and for each spherical layer a spherical harmonics transformation is performed up to degree and order 60. From the expansion coefficients the magnetic field is derived. The spherical harmonics analysis is computationally heavy, but has to be done only once, and the transformation to the B-field is swift.

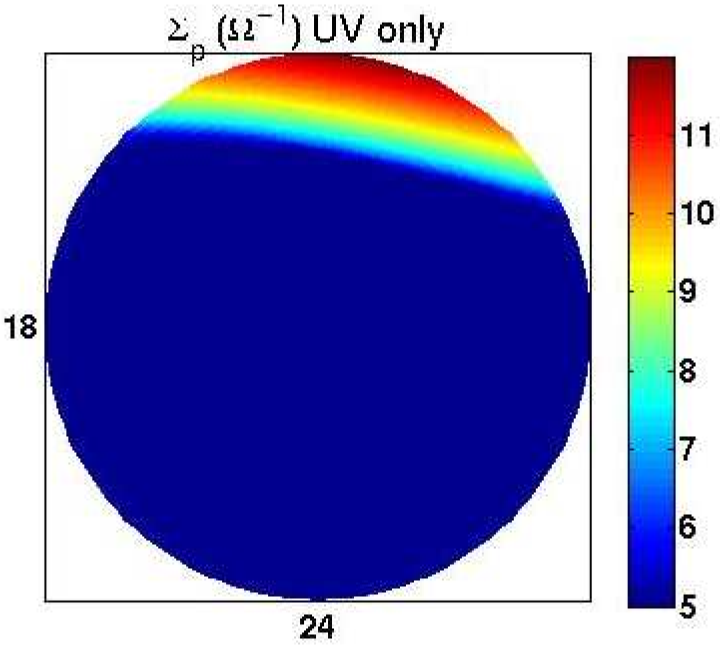

Figure 4.3a Ionospheric conductance with F10.7 for noon UT November 20, 2003

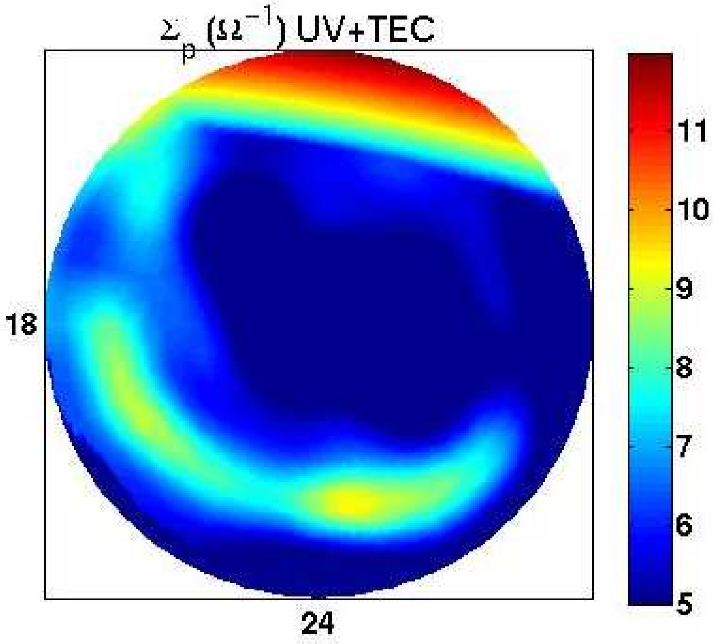

Figure 4.3b Ionospheric conductance with TEC and F10.7 for noon UT November 20, 2003

4.2.6 Comparing to observed magnetic perturbations

We use magnetic field observations from the Ørsted and Champ satellites, from which we subtract the internal magnetic field to get high-latitude magnetic perturbations. These are transformed to geomagnetic coordinates and compared to the modelled perturbations and a mean square deviation computed.

4.2.7 Fitting FAC parameters using least squares

The dependence of the magnetic perturbations on the FAC parameters is highly non-linear and to a large extent local. The magnetic perturbations strongly depend on the distance to a current segment. For this reason a direct least squares iteration, numerically computing the derivatives of the error function with respect to the parameters and using the Gauss-Newton algorithm, is not very effective. Instead we have utilized a random walk in parameter space – always descending in least squares deviation. This method does not guarantee to get out of a local minimum in parameter space and is therefore, as implemented at the moment, somewhat "hand-held". The use of a random walk in parameter space does point in the direction of a full implementation of a simulated annealing method or similar.

4.2.8 Compute ionospheric Joule heating

When deriving the ionospheric currents we computed the ionospheric electric potential and therefore also have the ionospheric electric field, E, readily available. The ionospheric Joule heating is then computed from $j \cdot E$ integrated over the polar ionosphere.

4.2.9 An example

Below we show the results for Champ orbit #18970 and Ørsted orbit #24981, November 21, 2003, 17:00.

During the November 2003 event Ørsted and Champ were both in near noon-midnight orbits. Ørsted was at a mean altitude of 750 km, while Champ was at a mean altitude of 395 km. Figures 4.4a and 4.4b show the observed magnetic perturbations for November 21, 17:00 UT.

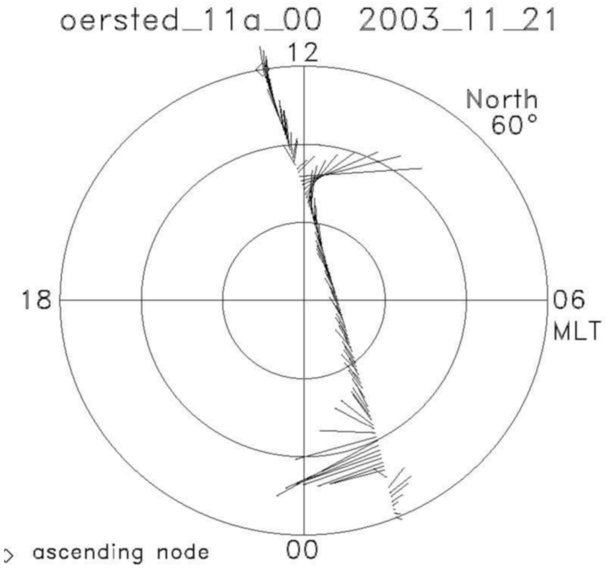

Figure 4.4a Magnetic perturbations observed for Ørsted on November 21 2003, 17:00 UT.

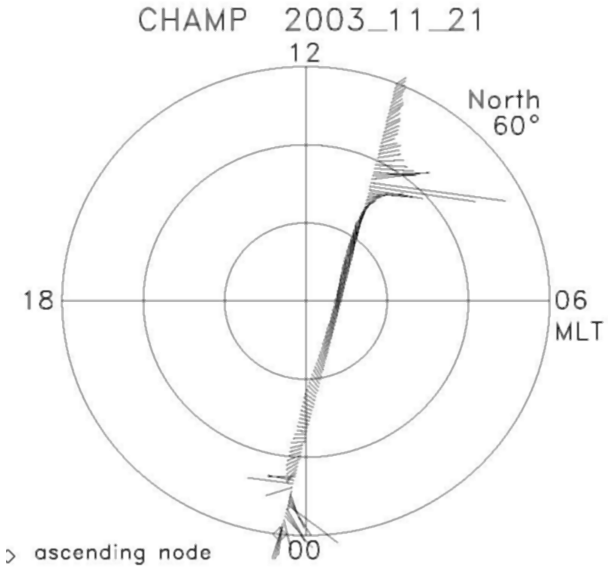

Figure 4.4b Magnetic perturbations observed for Champ on November 21 2003, 17:00 UT.

Based on an initial guess mainly derived from the longitudinal component of the observed perturbations we arrived at the field-aligned currents shown in Figure 4.5. Some artefacts of the parameterization is readily seen with the abrupt change of current density in the dusk Region 2 current near 18 MLT as the most noticeable. The noon-midnight orbits of both Ørsted and Champ makes the estimation of the currents at dawn and dusk more difficult.

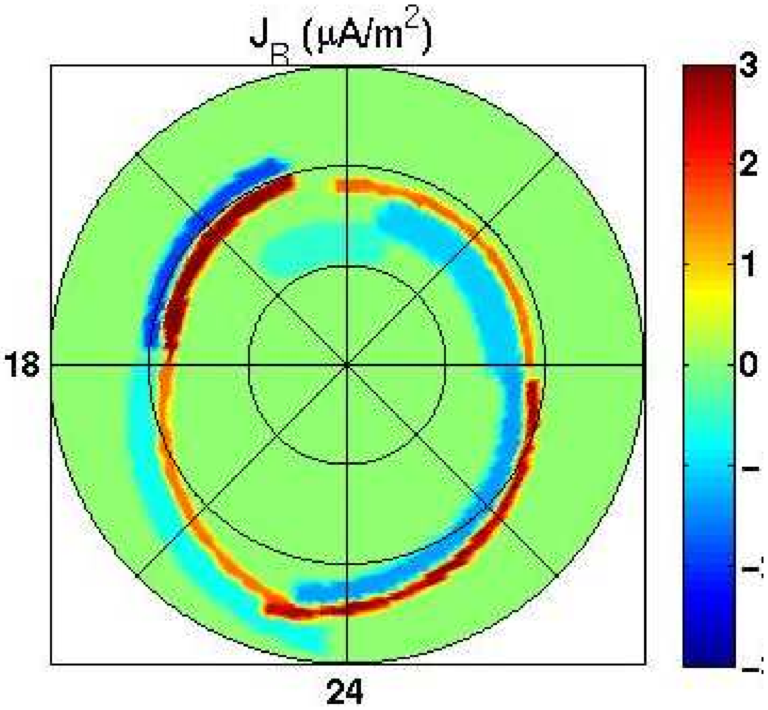

Fig 4.5 Field-aligned currents in MLT/cgm-latitude coordinates on November 21 2003, 17:00 UT. Noon at top of figure.

In Figure 4.6 the ionospheric Pedersen conductance, electric potential, and longitudinal and azimuthal currents are shown for November 21 17:00 UT. At the time no noticeable auroral precipitation was observed in the TEC values. Compared to Figure 4.3 the magnetic pole is clearly tilted further towards the sun giving a more significant contribution from UV to the conductance. The potential shows a more pronounced asymmetry than expected, a sign that something may not be entirely correct in the field-aligned currents. J_ϕ clearly shows the auroral electrojets, while J_θ shows some cross-polar current on the day side.

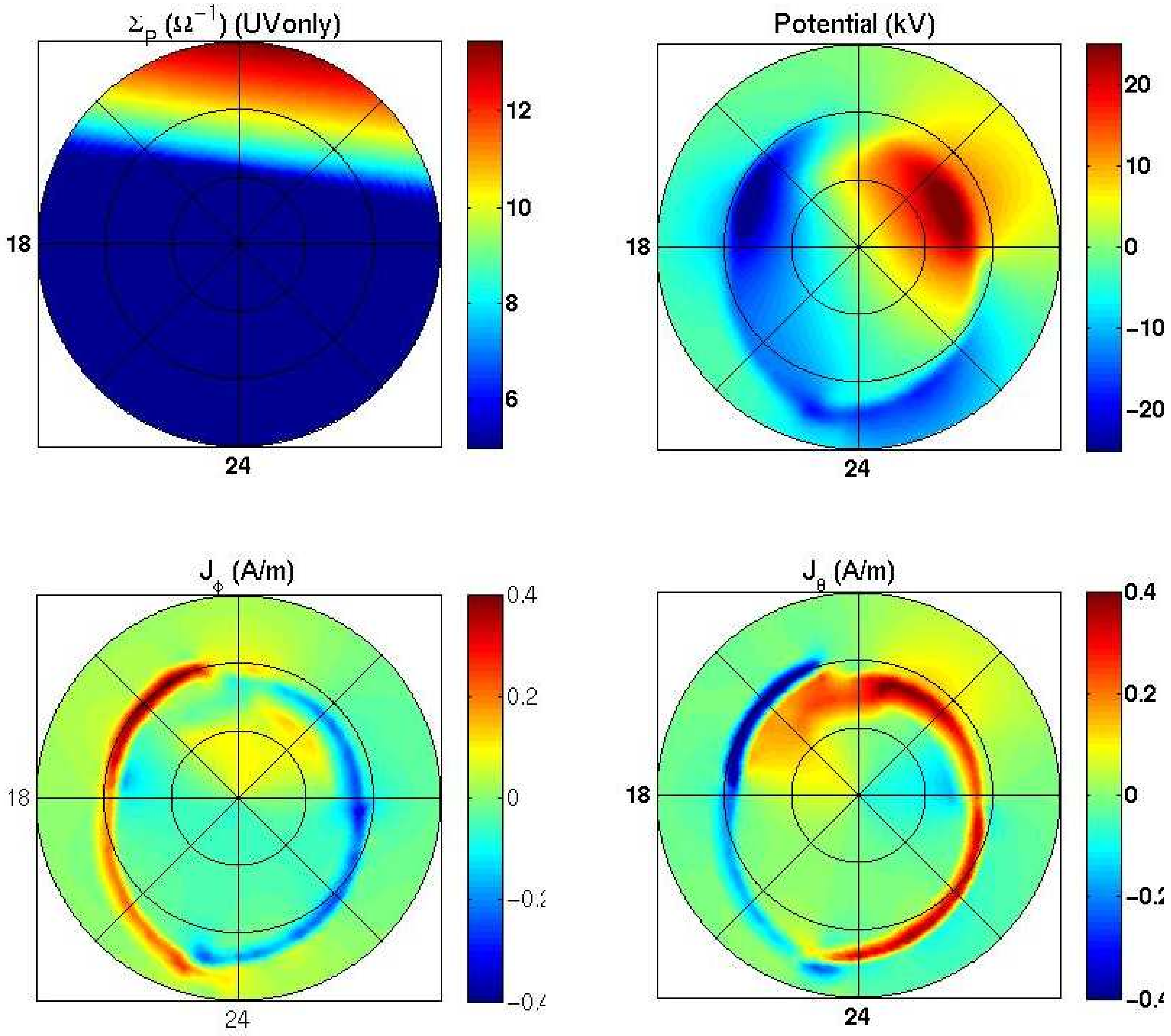

Figure 4.6 Top: Pedersen conductance
Bottom: longitudinal ionospheric current
Top: Electric potential
Bottom; azimuthal ionospheric current.

Comparisons of the observed and modelled magnetic perturbations are shown in Figures 4.7. We see that the longitudinal (east) component is modelled excellently. The longitudinal component has both the largest perturbations and is most directly linked to the current segments passed by the satellites. It is therefore somewhat favoured in the fitting procedure. The azimuthal (south) component is well modelled though some observed spikes are not seen in the modelled data. The radial (up) component has the least correspondence between model and observation. On the day side the model does a reasonable job, but on the night side the large observed dip is not modelled at all. There is a clear indication that something is not quite right in the modelled ionospheric currents, possibly the cross-polar currents are not strong enough on the night side.

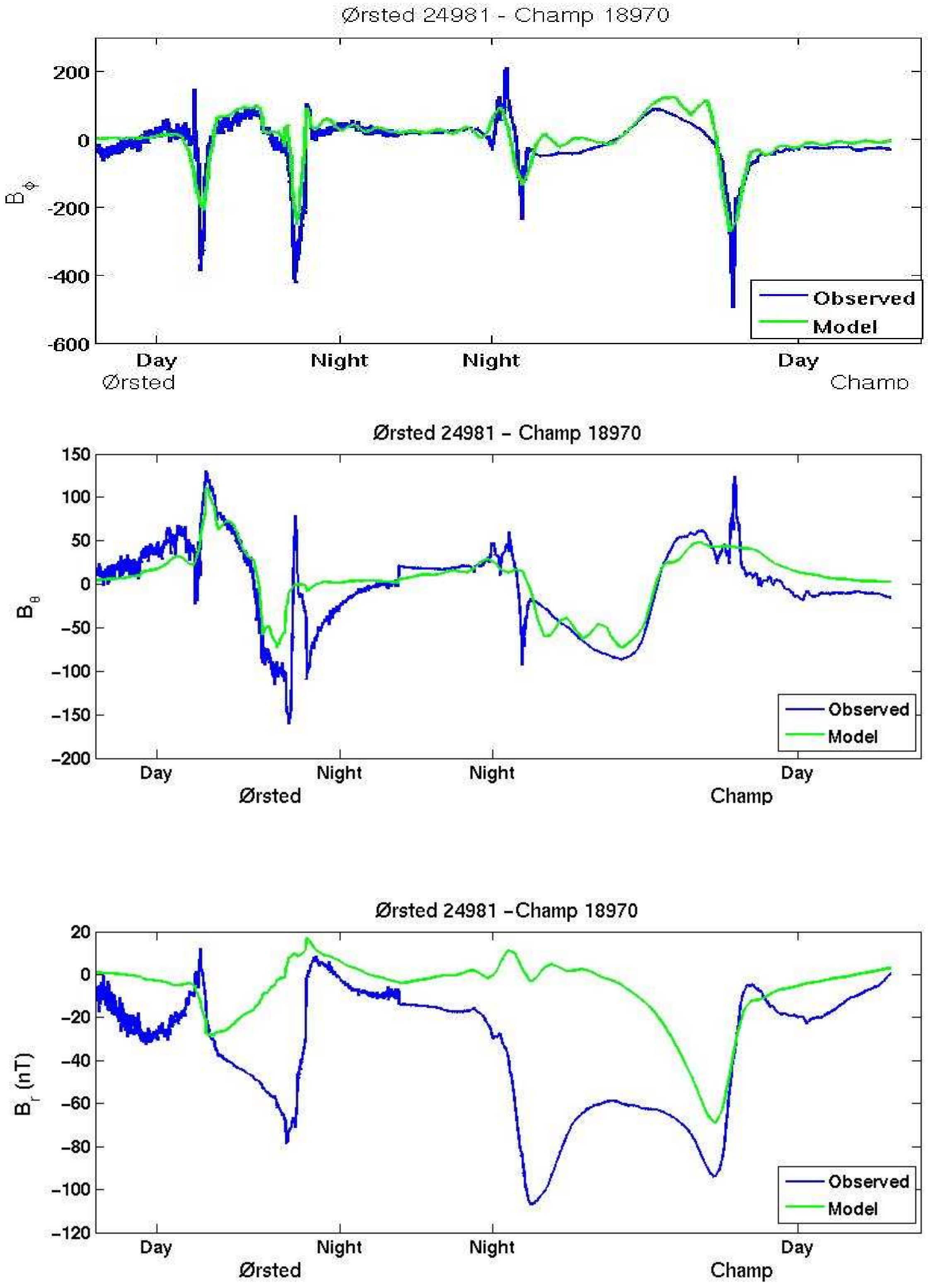

Figure 4.7 Modelled (green) and observed (blue) magnetic perturbations in magnetic east (top), magnetic north (middle), and radial (bottom) components. Ørsted data are shown on the left, Champ on the right.

4.2.10 Joule heating

We have computed the field-aligned/ionospheric currents and ionospheric electric potential from Ørsted and Champ magnetic perturbation data, and from ionospheric conductances based on F10.7 and TEC maps, for the period November 19-22, 2003, when a strong geomagnetic storm took place, Dst reaching -422 nT on November 20. From the ionospheric potential and currents we have computed the Joule heating based on constant ionospheric conductance, UV-based conductance, and UV+TEC conductance. Figure 4.8 shows the result, also shown is the heating derived Knipp et al. (2004) based on a combination of the PC and Dst indices (see Section 6.3). The same data are shown in a log-plot in Figure 4.9.

Relatively little difference is seen between the constant and UV-based conductances due to season (early winter, northern hemisphere), except late afternoon every day, when the magnetic pole tilts towards the sun.

Some differences, approximately 10%, are seen at the most disturbed times between the UV-based and the UV+TEC based conductances, when the TEC values are high in the auroral oval. The conductance based on total electron content is simply based on a proportionality factor. A more realistic TEC-conductance might show greater differences.

All the Joule heating curves follow each other nicely increasing from 10's of GW before the storm to about 2000 GW at the height of the storm. Note that the exact values depend strongly on the background conductance that we here have put at 5 Ω^{-1}. The Joule heating from Knipp et al. (2004) follows our computed values nicely except that it drops far below just before the storm. The Joule heating computed from the ionospheric currents never drops below a few 10's of GW.

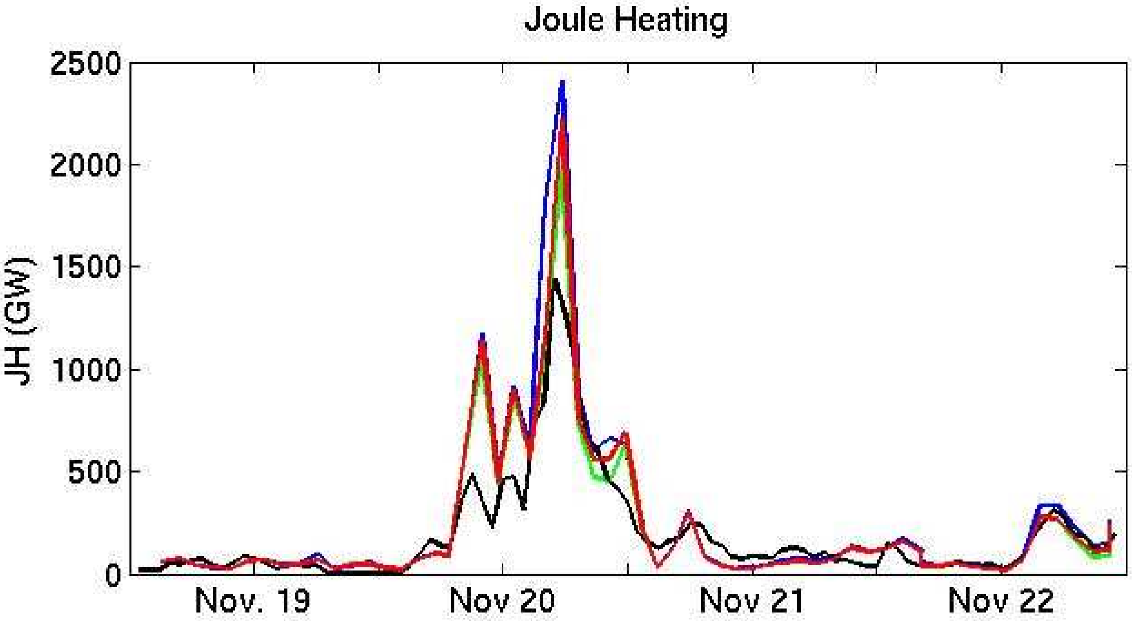

Figure 4.8 Joule heating: constant conductance (5 Ω^{1}) (blue), UV-based conductance (red), UV+TEC based conductance (green), Knipp, 2004 (black).

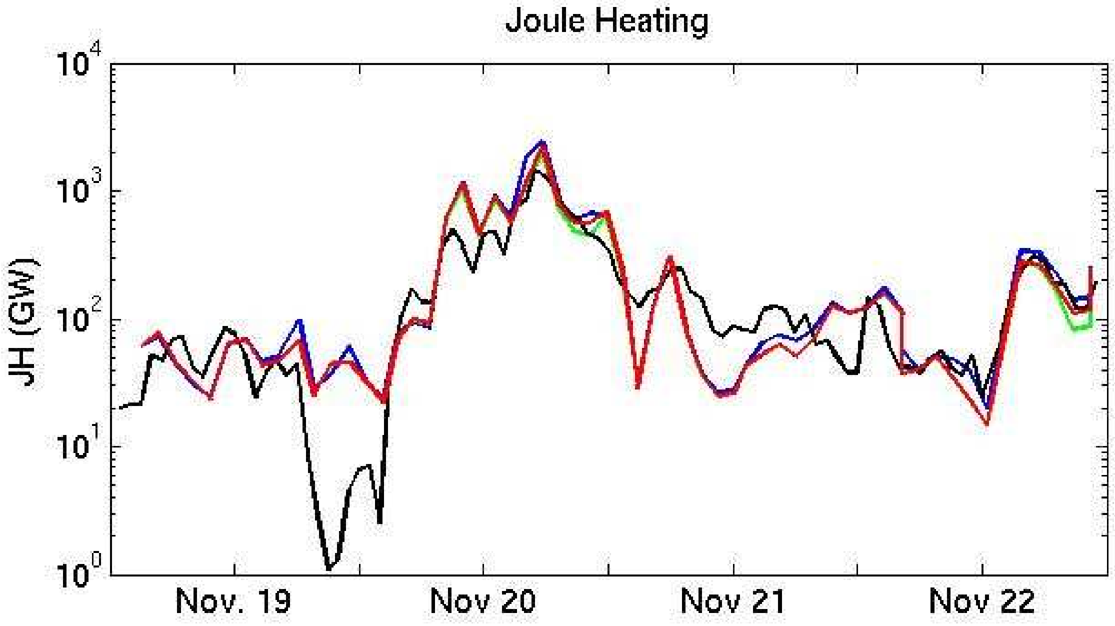

Figure 4.9 Joule heating: constant conductance (5 Ω^{1}) (blue), UV-based conductance (red), UV+TEC based conductance (green), Knipp, 2004 (black)

4.2.11 Summary

We have derived the large scale structure of full ionospheric/field-aligned current system from magnetic observations from single passes of the Ørsted and Champ satellites, along the way also getting the ionospheric currents, electric potential and Joule heating. The Joule heating thus derived fits nicely with a PC-Dst based derivation even though some of the features of the current system are clearly artefacts from the chosen parameterization of the field-aligned currents.

The aim is to develop this method into an operational tool that may be run automatically on reception of data from single passes of the upcoming Swarm satellites, delivering position and strength of the Region 1 and 2 currents as well as Joule heating and other ionospheric parameters.

5. Magnetic activity and radiation

5.1 Solar Energetic Particles cut-off latitude and magnetic activity

An important property of the Earth's magnetic field in the context of space weather is its ability to shield spacecraft located well within the magnetosphere from solar energetic particles (SEP's). During solar particle events highly energetic particles are accelerated at the sun and in the heliosphere and impinge upon the Earth's magnetosphere. How deep into the magnetosphere these particles penetrate that depends both on the magnetic latitude and longitude of the particular location and of course also on the type and energy of the particles.

For polar orbiting spacecraft in low-Earth orbit a particular important aspect is the so-called cut-off latitude. Low energy ions from the solar wind have a direct access to low Earth orbit along open magnetic field lines that map directly from the interplanetary space to the polar cap. These particles will therefore reach spacecraft in low Earth orbit when the spacecraft pass the polar cap defined as the region poleward of the open/closed field-line boundary. More energetic ions can, however, penetrate deeper into the magnetosphere and can therefore reach lower latitudes. When high energy ions are observed by a polar orbiting space craft during solar energetic particle events a characteristic steep drop in particle flux is seen in a narrow latitude band, when the spacecraft fly from high to low latitudes. This steep drop defines the so-called cut-off latitude of SEPs. It is illustrated in Figure 5.1 for high-energy protons detected with the Solar Anomalous and Magnetospheric Particle Explorer (SAMPEX) Proton Electron Telescope (PET).

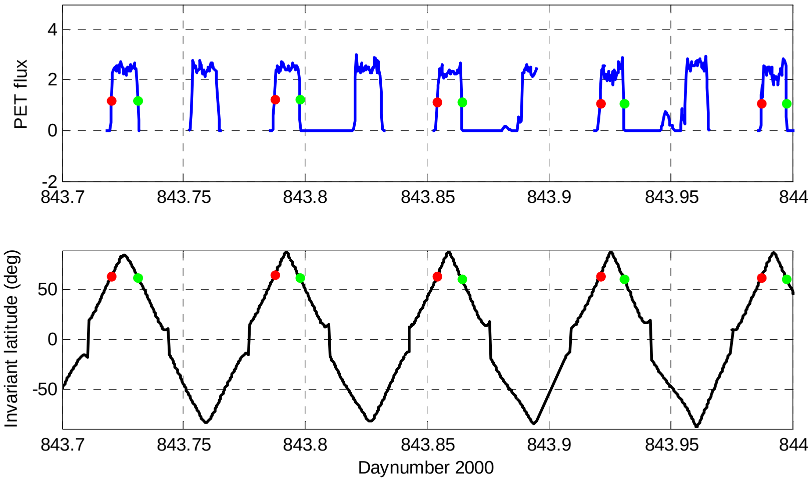

Figure 5.1 Top: Variation in flux of high energy protons ($cm^{-2}s^{-1}sr^{-1}MeV^{-1}$) as measured by the SAMPEX in the 19-27MeV band. The red and green dots represent the determined cut-off points for entry and exit of the northern polar region respectively. The points are defined by a flux level of 50% of the central polar cap level. Bottom: Magnetic invariant latitudes in degree for the SAMPEX orbit. The red and green dots represent the determined cut-off latitudes.

Maps of cut-off latitude for particles of different rigidity (momentum pr. unit charge) are regularly calculated based on the International Reference Geomagnetic Field (IGRF) model of the intrinsic part of the Earth magnetic field. However, geomagnetic disturbances are known to create significant deviations in cut-off latitude. In particular the weakening of the field due to the build-up of the ring current and partial ring-current, as quantified by the Dst index, has been shown to be closely associated with equatorward movement of the cut-off latitude (Leske et al. 2001). So during strong geomagnetic storms, where SEPs also often are present, spacecraft in low Earth orbit are less protected than normal. This variability is naturally of importance when estimating radiation dose for spacecraft - satellites as well as the international space station (Leske et al. 2001). Recently Mertens et al. (2010) also demonstrated that the effect of magnetospheric currents can have significant influence on the radiation exposure for high-latitude air-craft routes.

The close relation between Dst and cut-off latitude has, however, also been shown not always to apply. During strong compression of the magnetosphere, e.g. associated with storm sudden commencements, significant deviations are observed that appear to be very local time dependent (Kress et al. 2004, Belov et al. 2005, Lee and Kress 2008). In two recent paper Kress et al. 2010 and Mertens et al. 2010) used a combination of IGRF and the Tsyganenko model for magnetospheric current systems to model the influence of magnetospheric currents systems on the cut-off latitude for a specific event, namely the October 2003 so-called Halloween storm. They found a nice correspondence between the model and SAMPEX PET observations of cut-off latitude. Their results also strongly indicate that the partial ring current creates significant local time variations of cut off latitude.

In SOTERIA two important goals are directly connected to Dst and local time variations of low latitude magnetic activity:

- to create new measures of geomagnetic activity based on magnetic observations from polar orbiting satellites,
- to make a new ground-based Dst like index, Dcx, based on a more dense ring of low latitude ground magnetic observatories than utilized for Dst.

Both of these types of measurements, satellites and ground-based networks, can naturally be used to monitor local time variations of low-latitude magnetic disturbances. We have therefore made a study of the association between cut off latitude variations for different local times and the variation of the local magnetic field magnitude at these local times; the perspective being that real-time monitoring or fore-casting of low-latitude "Dst-like" perturbations might be used to monitor or forecast cut-off latitude of SEPs for different local time regions.

In order to estimate the cut off-latitude we used a method similar to that described in Kress et al. (2010). Following Kress et al. (2010) we utilized the SAMPEX PET observations of the energetic protons (19-27 MeV energy band), but in order to get a better local time coverage we also used simultaneous observations of omni-directional energetic protons from the Medium Energy Proton and Electron Detector (MEPED) onboard NOAA's Polar Orbiting Environmental Satellites (POES) POES-15, POES-16 and POES-17. The SAMPEX spacecraft was in a low Earth orbit at approximately 600 km's altitude and an orbital inclination of 8 degrees. The PET data used was the series of 30 s averaged proton flux provided by Glenn Mason (JHU/APL) through the Coordinated Data Analysis Web (CDAWeb) site. The POES satellites are a series of near sun synchronous LEO satellites orbiting in different local time planes in the altitude range of roughly 800-870 km.

We have performed two detailed event studies. The first event studied was a large SEP event which occurred in April 2002 during the recovery phase of a medium size but complex magnetic storm. This event was selected partly because it was a large SEP event of significant duration, which allowed for determination of cut-off latitude for ~10 days following the event, and partly because a good coverage of magnetic satellite measurements was available. Figure 5.2 provides an overview of the event, showing variations in energetic proton flux measured by SAMPEX-PET in top, Dst in the middle panel and the so-called auroral boundary index in the bottom. The auroral boundary index is determined from the flux of precipitating electrons as measured by the DMSP satellites. It is constructed to provide a measure of the equatorward boundary of the auroral oval at magnetic midnight (Gussenhoven et al. 1981, 1982, 1983).

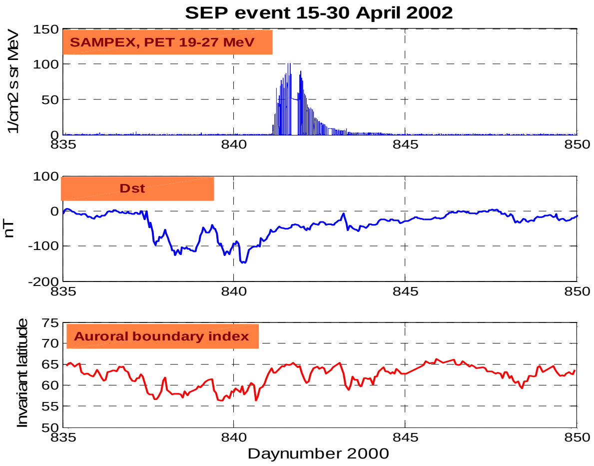

Figure 5.2: Overview of Event 1. Top: SAMPEX PET high energy proton flux. Middle: Dst Bottom: Auroral boundary index

Figure 5.3 shows the cut-off latitude determined from PET during entry (red dots) and exit (green dots) of the northern polar region. These values are determined as the magnetic invariant latitude at which the PET proton flux has decreased to 50% of its value in the central polar region as illustrated in Figure 5.1. The cut-off latitudes are displayed in both the top and the middle panel. In the top panel they are compared to the Dst index (in a scaled version to facilitate the comparison) and in the middle panel they are compared to the auroral boundary index. The bottom panel shows the local time (in MLT) where SAMPEX enters and exits the polar region. Although this event occurs during the recovery phase of a storm, and also covers a relatively quiet period, it is clear that even minor changes in the Dst index are associated with changes in cut-off latitude. It is however also clear, from the difference between the red and green dots, that significant local time differences occur. The question is whether these local time differences can be directly linked to local time differences in the low-latitude magnetic disturbance.

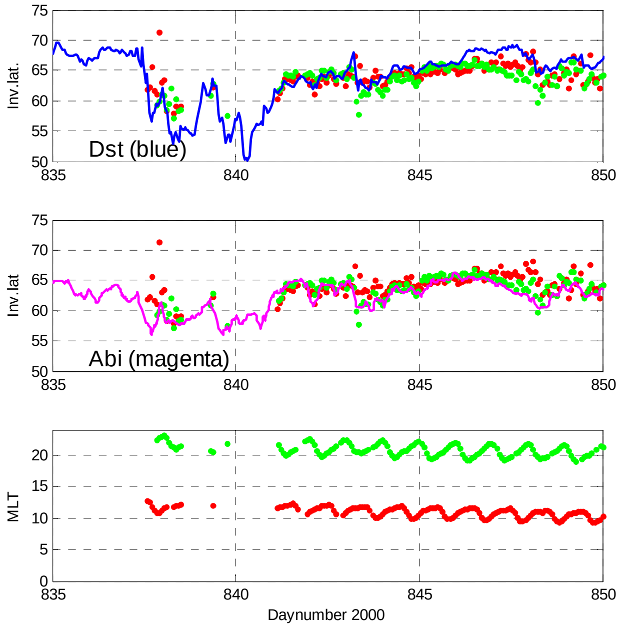

Figure 5.3: Comparison between cut-off latitudes determined from SAMPEX with Dst (top) and ABI (middle). The red dots show the entry points into the northern polar region, and the green dots the exit points. The lower panel shows the magnetic local time at entry and exit respectively.

The low latitude magnetic disturbance can be monitored either from ground, as it is customary done for Dst, but also from satellites in a low Earth polar orbit. During April 2002 three satellites, each equipped with high precision magnetometers were operating: Ørsted, SAC-C and CHAMP. When these satellites cross the latitude band where Dst stations are typically located the main observed disturbance will be due to magnetospheric currents, and “Dst-like” variations can be observed. Figure 5.4 illustrates this point. The figure shows the average magnetic disturbance measured by the 3 satellites when passing the 20-25 degree invariant latitude band. Only measurements of the field intensity relative to the internal main field was used, and the disturbance was normalized with the factor 1/cos(α), where α is the angle between the local main field direction and the magnetic dipole axis. For each satellite two time series are thus derived covering two local time sectors roughly 12 hours apart. In Figure 5.4 these time-series are compared to each other and to the ground based Dst index. It is seen that the satellite and ground based data are highly related, but it is also obvious that large local time variations exist in the magnetic disturbance.

The bottom two panels in Fig. 5.4 show the ground based Dcx index for specific local times corresponding to the orbits of the satellites. The differences between the disturbances at different local times are similar in the ground based Dcx indices to the local time differences measured by the satellites. The largest differences are seen roughly between the dawn and dusk (local times 4 h and 16 h) corresponding to CHAMP orbit. Also in the CHAMP time series one sees the largest variations from one value to the next. Overall the satellite disturbances and the ground based Dcx indices resemble each other quite well in this case.

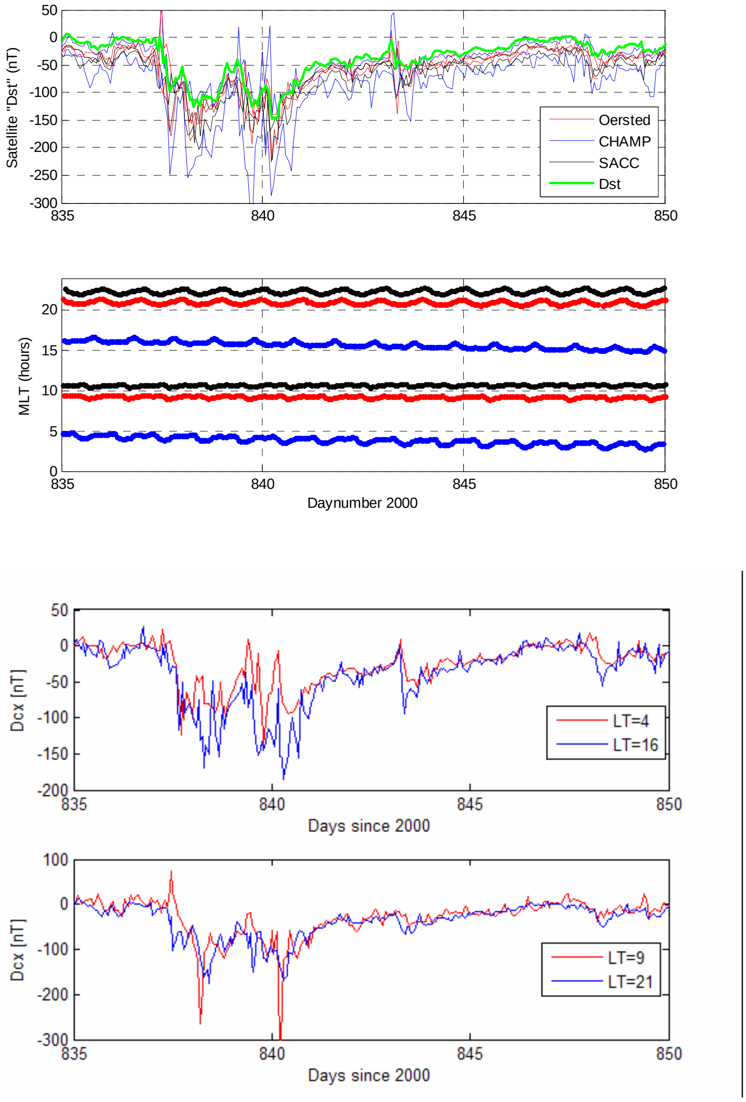

Figure 5.4: Satellite derived low latitude magnetic disturbance derived from B-field intensity measurements from the three satellites Ørsted, CHAMP and SAC-C compared to the ground based Dst index and the Dcx index at specific local times. Panels from top to bottom are: the magnetic disturbances, MLT of the three satellites when passing the 20-25 degrees invariant latitude region in the northern hemisphere, the ground based Dcx index at local times 4 h and 16 h corresponding to CHAMP orbit and the Dcx index at local times 9 h and 21 h corresponding to Ørsted and SAC-C orbits.

The local time-variations between the magnetic disturbance and the cut-off latitude can now be compared. During this event the Ørsted satellite is orbiting at magnetic local times (~21h and ~9h) very close to the MLT where SAMPEX passes the cut-off latitude (~21h and ~11h). It would therefore make sense to compare directly the variation in cut-off latitude with the variation in local "Dst-like" disturbance. Figure 5.5 illustrates this with SAMPEX data shown in the top, Ørsted data in the middle and the local Dcx indices corresponding to Ørsted local times at the bottom. The green curves are for the 21h local time region and the red curves are for the 9 and 11h region. It is seen that the local time difference in cut-off latitude at a given time corresponds closely to a similar local time difference in local magnetic disturbance. Periods where the night/dusk-side cut-off latitude is lower than the day/dawn side, most notably during the two minor storm intervals at Julian Day (JD) 843 and 848 are observed as periods where the night/dusk side magnetic perturbation is more strongly negative than the day/dawn side perturbation. But also the opposite behaviour, that the day/dawn side perturbation is more negative/at lower latitude than the night/dusk side, is observed in both types of data, e.g. in JD 841-843 and 845-847. In general also here the magnetic disturbances measured at the ground (Dcx) and by the satellite roughly a like. Especially the dawn dusk difference during JD 843-844 is evident both in the Dcx and the satellite Dst index.

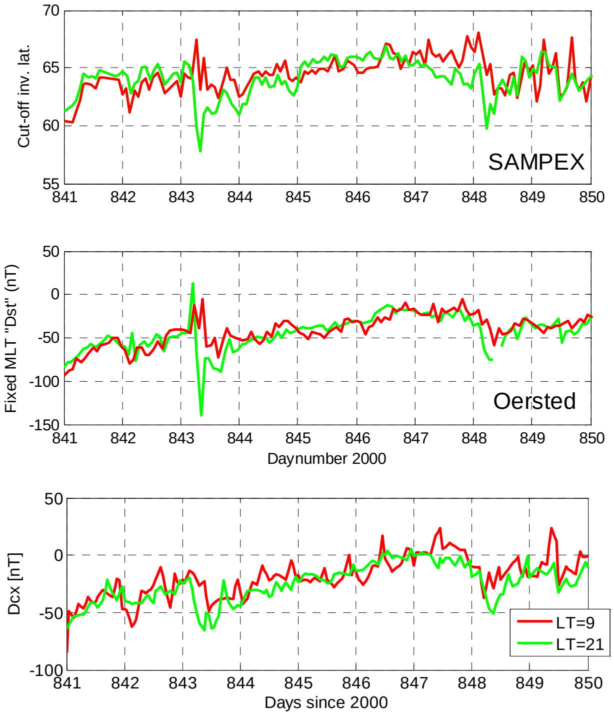

Figure 5.5. Cut off latitude variations as measured by SAMPEX (top), compared to low latitude magnetic perturbation variations as measured by Ørsted (middle) and the Dcx indices at local times corresponding to Ørsted orbit (bottom) during recovery and following minor storms of the April 2002 event.
Red: day/dawn MLT sector
Green: night/dusk MLT sector.

For examination of a more disturbed event we have chosen to investigate the great magnetic storm of October 2003, the so-called Halloween storm. This event also has the advantage that during this period three POES satellites POES15, POES16 and POES17 were operating, i.e. three satellites in different local time sectors, which should be directly comparable. Likewise also all three magnetic field measuring satellites were operating. Figure 5.6 shows the variation in cut-off latitude for entry and exit of the northern polar region determined independently for the three POES satellites during the part of the storm when there was the most continuous estimation of the cut-off (i.e. the most prominent SEP flux). This provides time series for six local time sectors shown in black. The curve shown in green in the background is the auroral boundary index ABI. It is clear from this that significant deviations are observed for different local times. Particularly noteworthy is the fast decrease in latitude around jd 1398.8 for the crossings in the dayside 7.9MLT, 11.0MLT and 17.0MLT compared to the slower decrease at the night side (3.2MLT and 20.6MLT) where the minimum latitude is reached much later close to 1399. Also interesting is the differences observed during the recovery phase between 1399 and 1399.6. In this case it is the morning side crossings (7.9 MLT, 11MLT and 11.5MLT) that appear to occur at significantly higher latitudes than the other local time sectors. The dusk/night local time sector on the other hand follows nicely the auroral boundary index, similarly to what was observed in the first event (Figure 5.3).

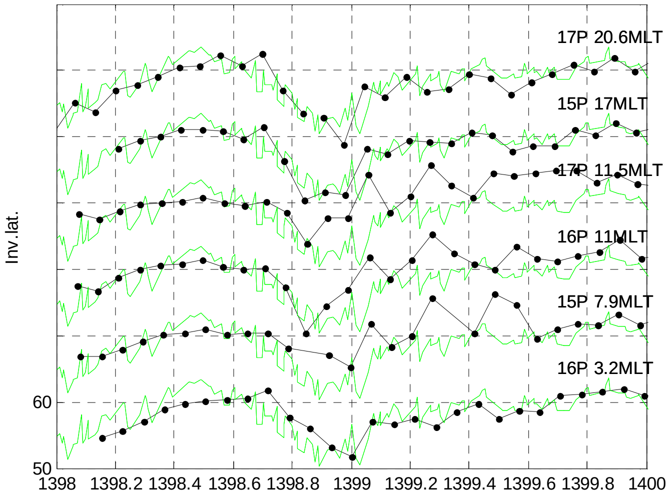

Figure 5.6 Cut-off latitude as observed by the POES, MEPED omni-directional high energy proton flux during part of the Halloween storm, 29-30 October 2003 (black). To the right of each curve it is written from which satellite (POES16, POES16 or POES17) the data are derived as well as the MLT of the crossing point. Green curves (6 identical curves) show the auroral boundary index.

Figure 5.7 illustrates the same time-interval, but for the magnetic perturbations. The green curves are now simply Dst. Unfortunately all three satellites are during this event orbiting close to noon-midnight MLT, and Ørsted and CHAMP are very close in MLT. Nevertheless the day/night difference in the timing of the main phase of the storm observed for the cut-off latitude is nicely reproduced in the magnetic disturbance. The dawn/dusk asymmetry observed in cut-off latitude during the recovery is, however, not evident. This on the other hand is to be expected since these satellites are orbiting close to the noon-midnight meridian.

Another interesting feature is observed when comparing CHAMP and Ørsted. Due to the fact that these two satellites during this particular event are in very similar local time sectors, one would expect almost identical perturbations. This appears to be the case concerning the relative variations (i.e. the form of the profile) but not the amplitude. Since CHAMP has a significantly lower orbit than Ørsted, this could indicate that the contribution from possible local ionospheric currents cannot be neglected. This is a serious problem that requires careful consideration before the satellite data can be used as a possible indicator of local time variations in cut-off latitude.

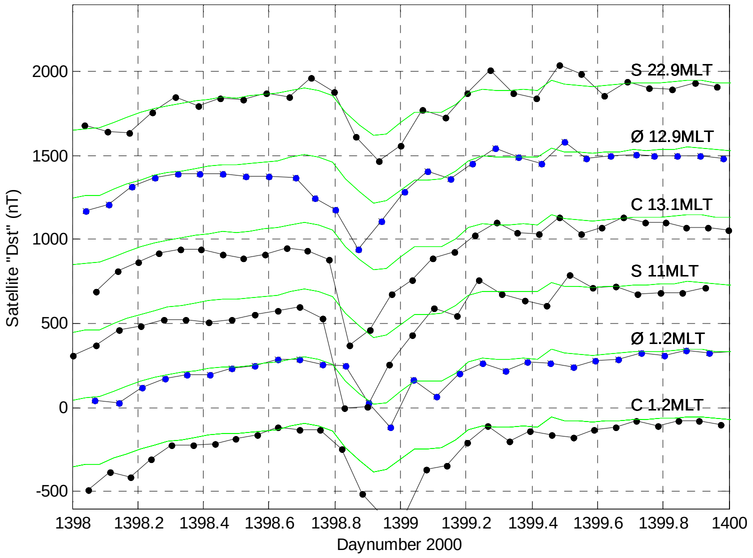

Figure 5.7 Low latitude magnetic disturbances during the Halloween storm for Ørsted, SAC-C and CHAMP in the same format as Figure 5.6 (black for CHAMP and SAC-C, blue for Ørsted). The green curve in the background is here the Dst index.

A statistical study of the cut-off latitude will necessarily be limited to the time periods during which significant fluxes of SEPs are present. However, the strong association between cut-off latitude variations in the dusk/night sector and variations of the auroral boundary index indicating that the variations in cut-off latitude and in the auroral boundary index share a common physical background (i.e. primarily variations in the large-scale magnetic shielding) makes it interesting to compare the ABI and the magnetic disturbance statistically in this context of cut-off variations.

Figure 5.8 shows on top a scatter-plot of the local-time Dst derived from the Ørsted observations as a function of ABI for two different local time sectors 6MLT (blue) and 18MLT (red). The magnetic perturbation evidently behaves systematically different in the two local time sectors when compared to the auroral boundary index (determined mainly from dusk-side observations). In the bottom plot the linear correlation between Dst and ABI is calculated as a function of local time. The highest correlation ~0.8 is, not surprisingly, seen for the dusk-sector. This is also an improvement of the correlation obtained by using the, ideally, non-local time dependent Dst index. The linear correlation coefficient between Dst and ABI during the Ørsted period is 0.66.

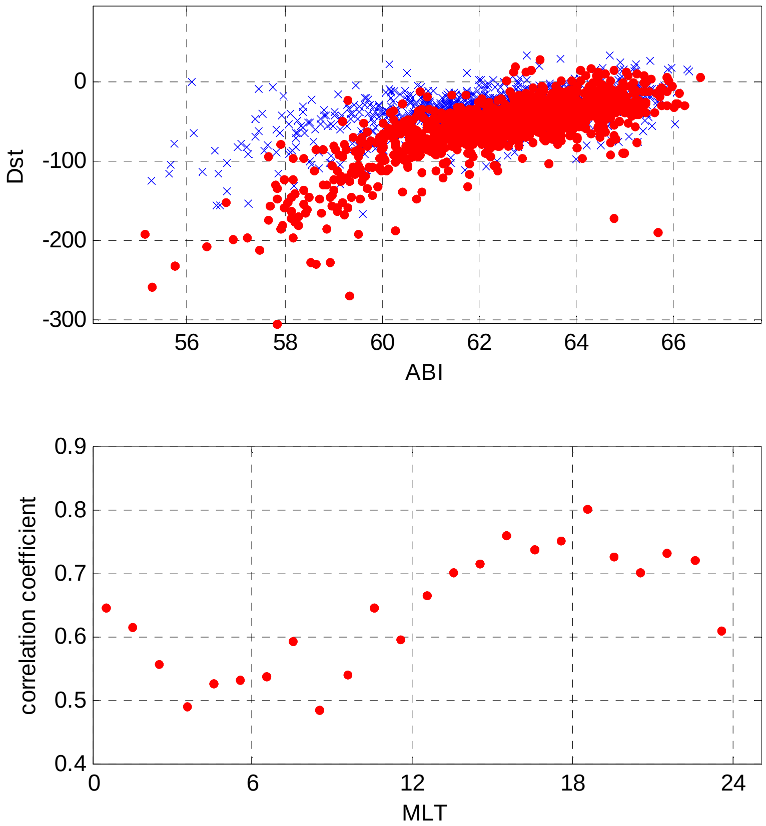

Figure 5.8 Top: Scatter plot of ABI versus local time Dst as determined from the Ørsted satellite for the 5-6MLT interval (blue) and the 17-18MLT interval (red).
Bottom: Linear correlation coefficient between ABI and Ørsted "Dst" as a function of magnetic local time of Ørsted during low latitude passage.

In summary we have examined cut-off latitude variations of high energy protons as determined from SAMPEX - PET and POES –MEPED in comparison with local magnetic low-latitude disturbances as determined from Ørsted, CHAMP and SAC-C and in comparison with Dst and the auroral boundary index determined from DMSP electron precipitation data. We find:

- The cut off magnetic latitude of high energy protons is both time variable and local time dependent. Differences in cut-off latitude for different local times are found both during the main phase of large storms and during storm recovery and more quiet intervals.

- The cut-off latitude variations in time are highly correlated with variations in the auroral boundary index ABI. The correlation with ABI is highest for cut-off latitude observed in the dusk and midnight sectors.
- Satellites in low Earth polar orbit measuring magnetic field intensity variations may be used to provide information on Dst variations, at least in specific local time intervals.
- We confirm previous findings that cut-off latitude variations in time are also strongly associated with Dst variations, but the correlation is improved when local time dependence of the near Earth magnetic perturbation is taken into account.
- The results indicate that local time magnetic field observations both from satellite or ground could be useful for monitoring cut-off latitude. However, more work is needed to adequately subtract local perturbations in the magnetic field not associated with large-scale magnetospheric currents, such as local ionospheric currents.

5.2 Auroral electrojets and particle precipitation

One of the most spectacular indicators of space weather is the auroral display – the significant increase of auroral activity and the tendency for the auroral region to move equatorward during geomagnetic storms. Apart from the public interest due to the impressiveness and beauty of the phenomena, the activity and migration of the auroral region is interesting in a space weather context for a number of reasons:

- The aurora is created by particles that are being accelerated to medium energies above the atmosphere, and which may constitute a risk for polar orbiting spacecraft.
- As shown in the previous section, the decrease in geomagnetic shielding of solar energetic particles during space storms - as evidenced by the equatorward migration of cut-off latitudes - is closely related to the equatorward migration of the auroral oval.
- The intense ionospheric currents flowing in the auroral region - the auroral electrojets - are known to be associated with Ground Induced Currents (GIC's) at high to mid latitudes.
- In association with these ionospheric currents, a significant Joule heating of the upper neutral atmosphere is observed, the size of which naturally depends on the intensity and extent of the currents. The Joule heating is associated with expansion of the neutral atmosphere, and hence density variations and orbital decay of LEO spacecraft.
- The auroral oval is often associated with ionospheric disturbances which frequently cause problems for radio-communication.

The location (latitude) of the auroral region is therefore also one of the WP4 focus parameters. It is currently being monitored using the signatures of particle precipitation, by NOAA using the POES satellites and by JHU/APL using the DMSP satellites. These data are used to define and locate a number of different precipitation boundaries. An important example is the midnight auroral boundary index ABI described in the previous section (Gussenhoven 1981,1982 1983), but also a number of other characteristic boundaries such as the electron isotropy boundary (Sergeev et al. 1983), the b2e boundary defined as the maxima in average energy of the precipitating electrons and interpreted to be mapping to the start of the central plasma sheet in the magnetotail, and also the boundaries defined by the most poleward and most equatorward electron acceleration events (b3a, b3b). The strict definition of these boundaries can be found in Newell et al. (1996).

Complementing the effort to monitor the auroral oval by monitoring the precipitating particles we have in SOTERIA investigated two alternatives:

- To monitor the location and intensity of the auroral electrojets using magnetic measurements from LEO polar orbiting satellites such as CHAMP and Ørsted.

- To monitor the location of the total electron content (TEC) enhancement observed in the night-side auroral region, believed to be associated with the precipitating particles, using GPS measurements.

In this section we will describe the results of this investigation on the basis of event studies, where we compare the different phenomena: precipitation, electrojets and TEC and also compare the estimated variations in the intensity of the electrojet current with the well known ground-based high latitude auroral electrojet indices AL and AU.

5.2.1 The auroral electrojets

Polar orbiting satellites pass right through the sheets of field-aligned currents (FACs) flowing from the magnetosphere to the ionosphere and feeding the ionospheric auroral electrojets. Being aligned with the magnetic field these currents produce strong magnetic perturbations perpendicular to the Earth’s main field direction. Being perpendicular to the much more intense main field (100’s of nT versus ~50.000nT) the disturbance field contribute very little to the local field intensity. The ionospheric auroral electrojets, on the other hand contribute significantly to the perturbation of the total field intensity. Monitoring the total field intensity from a polar orbiting spacecraft therefore carry potential to monitor the position and intensity of the auroral electrojets. This further has the advantage that no monitoring of the instrument attitude is necessary, since all that is needed is the total field intensity, and not its direction.

A classical method to determine the location of an ionospheric current is to examine latitude profiles of the vertical disturbance field. Ideally a line current will be located where the largest latitudinal gradient is observed. This is illustrated in Figure 5.9 for a pass of the CHAMP satellite. The blue line shows the disturbance in magnetic field intensity, and the red line the latitudinal gradient. The two dark points mark the estimated positions of the two electrojets as the satellite traverses the northern polar region. For a continuous current distribution, in place of a line current, this is of course not entirely true, but the method will nevertheless in most cases give a good estimate of the location of the most intense current. Another point that needs consideration is that the magnetic field intensity perturbation can be significantly different from the vertical field component of the disturbance field, unless the main field is vertical. The inclination of the main field, and therefore of the perturbation therefore introduces small, but systematic errors in the estimated location which need to be corrected for. The error will increase with altitude of the satellite, but for CHAMP it is only about 0.5-1 degrees, depending on magnetic latitude.

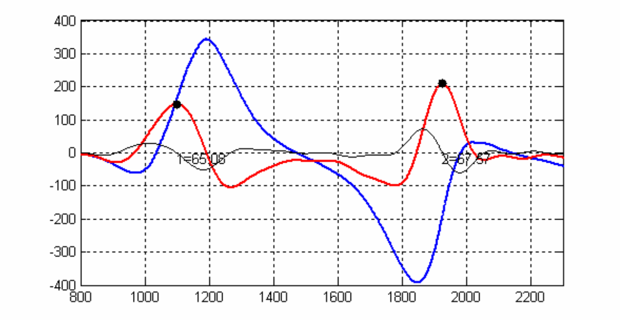

Figure 5.9 Example of observed magnetic perturbation by CHAMP when passing the northern polar region and the two electrojets. Blue: the measured perturbation in field intensity (nT). Red: the latitudinal gradient in field intensity. Time is in seconds.

Using consecutive passes of the polar region, it is then possible to monitor latitudinal migration of the electrojets. This is illustrated in Figure 5.10 showing a series of passes through a magnetic storm interval. In this representation westward currents are seen as a maximum in the field gradient and eastward currents are seen as a minimum. The blue dots show the location of the strongest observed westward current when passing the region of the westward electrojet located roughly at the dawnside (left part of the figure), and the also strongest observed westward current when passing the region of the eastward electrojet (right part of the figure). A very clear equatorward migration of the westward electrojet is observed during the storm.

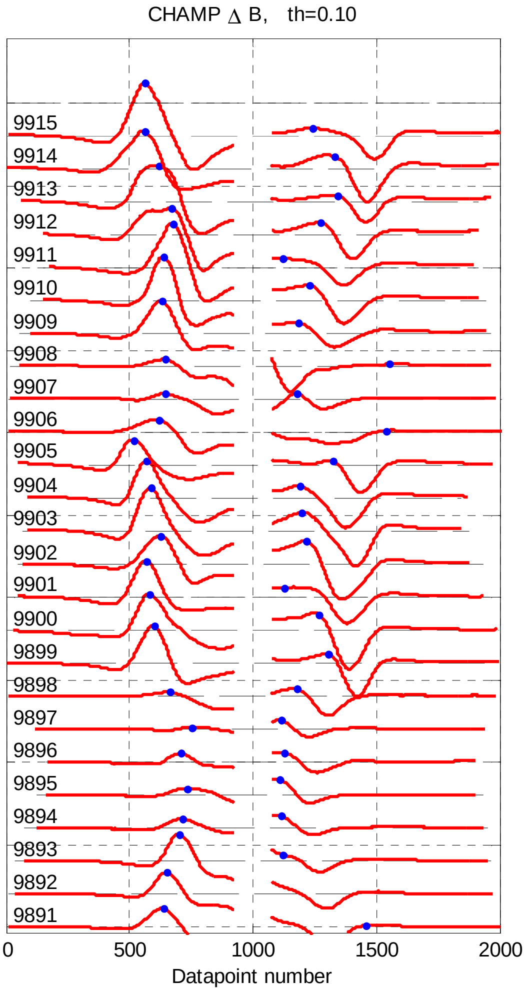

Figure 5.10 Observed latitudinal gradient in the magnetic field intensity for a series of consecutive passes of the northern polar region during the storm event in April 2002. The number to the left is the CHAMP official orbit number. The blue dot indicates the location of the maximum ***westward*** *current both at the dawn and dusk side of the auroral region.*

In Figure 5.11 time-series of the location of the electrojet are displayed for one of the selected WP4 events, the 3-storm event of July 2004. During this time-interval CHAMP was in a noon-midnight orbit, and only time-series for the midnight pass are displayed. The red curve shows the maximum westward current and the blue curve the maximum eastward current. Clearly the westward current is the “auroral” electrojet in this time interval. In Figure 5.12 the variation in location of the westward electrojet is compared to the (midnight) auroral boundary index ABI. It is seen that the electrojet, as could be expected, is always located poleward of the equatorward auroral boundary, but ABI and the electrojet latitude nevertheless display similar variations.

In addition to the latitude of the electrojet the latitude profiles of the latitudinal gradients can also be used to monitor variations in intensity of the current. For a line current the maximum in the latitudinal gradient is simply proportional to the current intensity. For a more realistic current distribution, the size of the maximum will at least provide a rough estimate of the peak intensity of the current. In the bottom panel we have compared the estimated current intensity variations to the well known high-latitude geomagnetic index AL, generally used as a measure of variation in the intensity of the westward electrojet. Note that the latitudinal gradient has been scaled to facilitate the comparison. In general a very good correspondence is found between the two measures, indicating that a “satellite AL” as described here could provide a nice way to monitor auroral electrojet activity in real time. The satellite and ground-based indices would be also complementary. The ground-based index has the advantage of a high time-resolution, while the satellite index has the advantage that it can monitor more accurately the intensity and location during large equatorward migrations of the electrojet, because during such events the electrojets have a tendency to move out of the "field of view" of the ground-based magnetometers being located in a ring in the auroral region. The satellite index further has the advantage, illustrated in Figure 5.13, that it can monitor, not only the northern electrojets, but also the southern polar region.

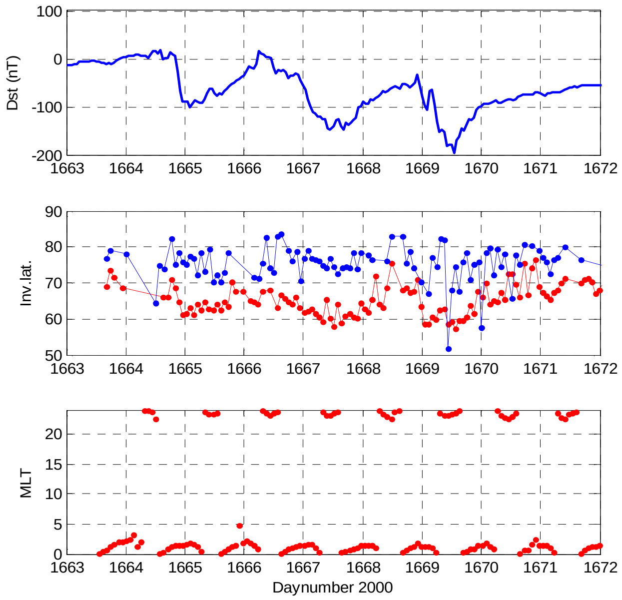

Figure 5.11 The July 2004 3-storm event.
Top: Dst
Middle: Latitudes of maximum westward (red) and eastward current (blue) during CHAMP passage of the midnight polar region.
Bottom: MLT of CHAMP during passage of the midnight auroral electrojet

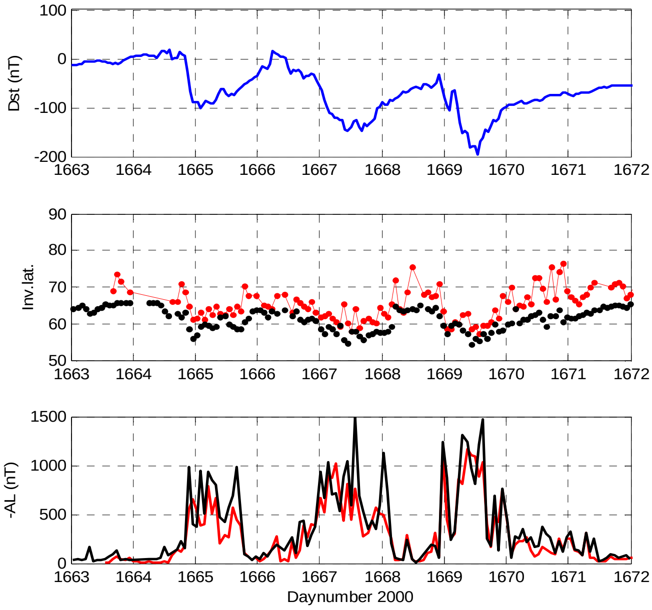

Figure 5.12 The July 2004 3-storm event.
Top: Dst
Middle: Latitudes of the westward electrojet (red) during CHAMP passage of the midnight polar region, compared to the midnight auroral boundary index ABI (black)
Bottom: Intensity variations of the westward electrojet as measured from CHAMP (red) compared to the ground based AL index (black). The satellite data has been scaled to facilitate the comparison.

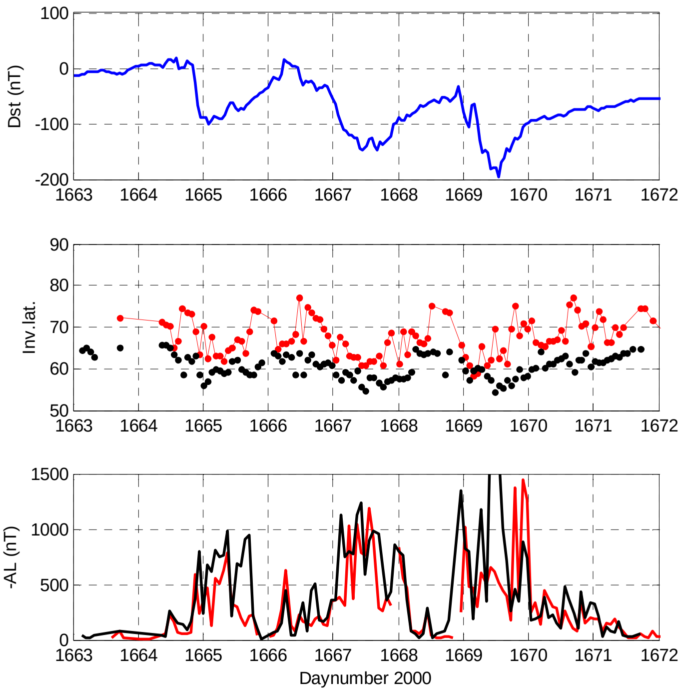

Figure 5.13 The same as Figure 5.12, but for the southern hemisphere midnight pass. (ABI is constructed to use data from both hemispheres, but AL is for northern hemisphere exclusively)

Figures 5.14 and 5.15 display similar parameters as Figure 5.12, for the entire month of April 2002, where CHAMP was in a primarily dawn-dusk orbit. Here we show the results for part of the pass over the northern polar region where the satellite was passing over the eastward electrojet region around 15 MLT. It is clear from Figure 5.14, that this is the region where the eastward electrojet is dominating the auroral region. The location of the electrojet is in this case further poleward with respect to the midnight auroral boundary than in the previous example. This is not unexpected since the latitude of the auroral oval is highly local time dependent, being much higher at the day-side than at the night-side. If an index for the electrojet location is to be created from the satellite data, in analogy with ABI for the particle precipitation, it is therefore necessary with a statistical investigation of the local time dependence of the electrojet latitude. Another difference between the two curves is the frequent poleward migrations of the electrojet to very high latitudes, seen most clearly after day 840 during storm recovery. These currents at very high latitude are normally associated with northward turnings of the IMF. They do not seem, however, to be accompanied by a poleward migration of the same magnitude of the equatorward (diffuse) auroral boundary as measured by ABI.

In Figure 5.15 the intensity of the eastward electrojet is compared to the AU index. In general there is a very good correspondence between the two, but there are also some differences. In particular it should be noted that while AU values almost go to zero during the strong poleward migrations of the electrojet, the electrojet intensity determined from satellite does not. The most straightforward interpretation of this is that the electrojet simply move out of view of the ground-based stations. In the bottom panel of Figure 5.15 we investigated whether it would be possible to monitor the westward electrojet intensity (AL) from the pass over the *eastward electrojet region*, i.e. from the intensity of the westward current observed significantly poleward of the eastward electrojet (red in second panel at Figure 5.14). The comparison with AL shows some resemblance, but the differences are in our opinion too significant for this to be an obvious possibility. We therefore envision a situation where the eastward and westward electrojets are observed once per orbit, both at the northern and southern hemisphere. This information could be folded into a single index, in analogy with ABI, or could be given for each hemisphere separately.

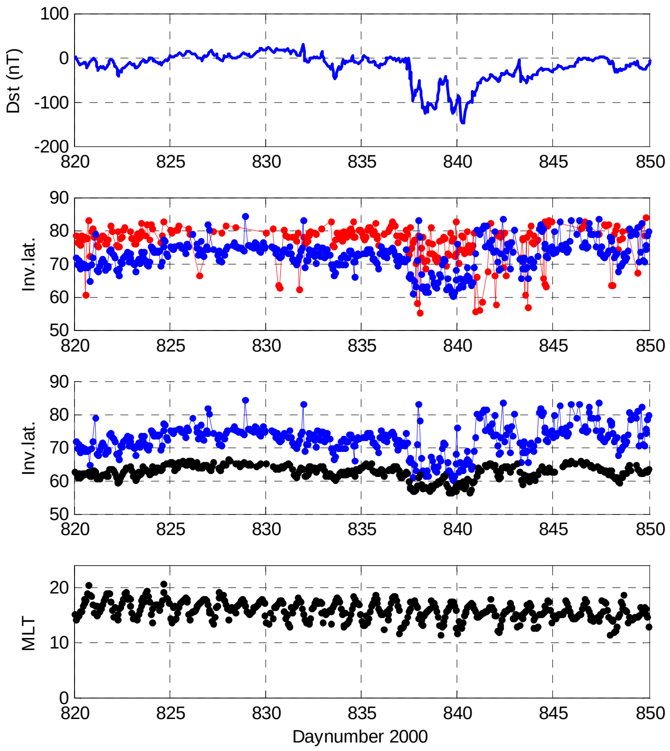

Figure 5.14 The electrojet latitudes during the entire month of April 2002
First panel: Dst
Second panel: Latitudes of maximum westward (red) and eastward current (blue) during CHAMP passage of dusk-side polar region.
Third panel: Latitudes of the eastward electrojet (blue) and the ABI (black)
Bottom: MLT of CHAMP during passage of the dusk-side auroral electrojet

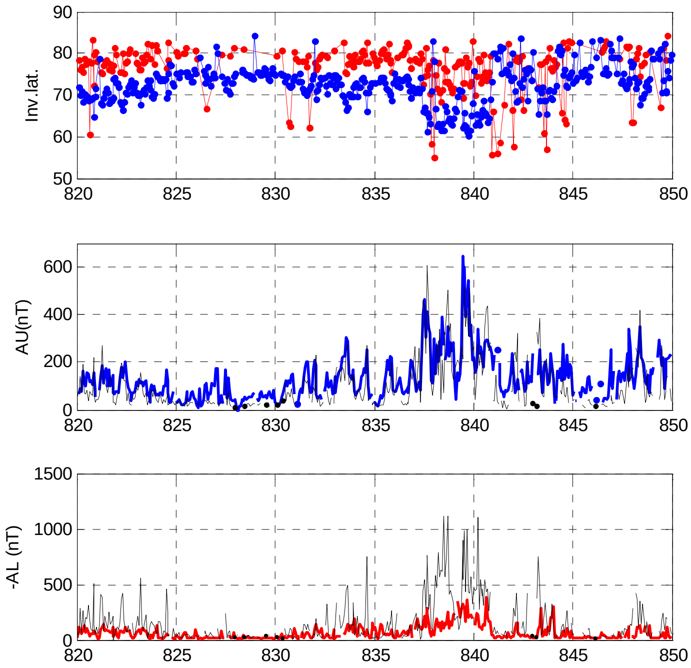

Figure 5.15 The electrojet latitude and intensity during the entire month of April 2002
First panel: Latitudes of maximum westward (red) and eastward current (blue) during CHAMP passage of dusk-side polar region.
Second panel: The intensity of the eastward electrojet (blue) compared to the AU index (black).
Third panel: The intensity of the maximum westward current during passage of the eastward electrojet region (red) compared to –AL (black).

5.2.2 Electrojets and particle precipitation

Herein above we have compared the electrojet location with the auroral boundary index. The particle precipitation in the auroral oval is, however, highly complex and a number of different precipitation boundaries have been defined, which would be relevant to compare to the electrojet variations. An obvious possibility is to compare with the isotropic boundary, which has been derived from POES and used in SOTERIA in connection with separation of the effect of tail- and ring current in Dst (see above sections). In Figure 5.16 this boundary is displayed for the 3-storm event in July 2004 together with the electrojet (red) and ABI (black dots). From first sight it seems that this index follows closely the electrojet, with a significantly better correspondence than ABI. It should however be noted, that the isotropic boundary displayed is derived from POES 15 crossing the oval around 15-18 MLT, while CHAMP is crossing near midnight.

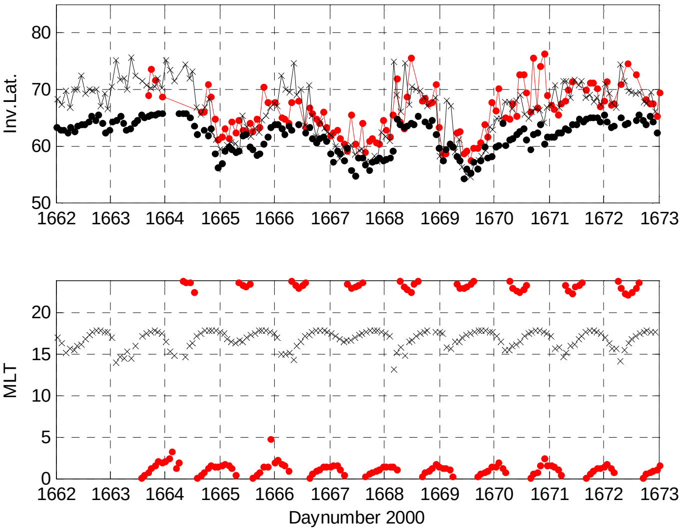

Figure 5.16 The July 2004 3-storm event.
Top: Comparison between precipitation boundaries, ABI (black dots), the isotropic boundary (black line and crosses) determined from POES 15, and the westward electrojet location (red).
Bottom: the magnetic local time of CHAMP (red) and POES 15 (black) while crossing the boundaries.

In order to draw definite conclusions about the relative locations of the various precipitation boundaries and the electrojet location we need to consider an event where the satellites orbit in similar local time planes. The April 2002 event was selected from exactly this criterion. As can be seen in Figure 5.17, during this event CHAMP, POES 15 and DMSP 13 were in almost identical orbits. In the top panel of Figure 5.17 various precipitation boundaries are displayed together with the latitude of the eastward electrojet (blue). The red dots show the isotropic boundary determined from POES 15. There are clear similarities between this and the electrojet curve, but the isotropic boundary is displaced systematically equatorward of the electrojet. A much more striking similarity is obtained between the electrojet and the b2e boundary determined from DMSP 13 (green dots). This boundary gives the latitude where the average energy of the precipitating electrons has a maximum. The striking similarity underlines the physical reality of the small deviations seen in electrojet latitude from one orbit to the next. These are clearly not just noise from uncertainty in the derived method, since the same deviations are observed in two completely different data sets. One physical explanation for the close correlation could be, that the precipitating electrons are creating a maximum in ionospheric E-region electrical conductance at this latitude, which then establishes a "flow-channel" for the ionospheric current. Alternatively, the physical origin of the two phenomena in the magnetosphere could simply be closely connected.

A similar striking association is found if we compare to the poleward and equatorward boundary of electron acceleration events believed to create discrete auroral arcs. In Figure 5.18 these two boundaries, b3a and b3b as described by Newell et al. (1996), are displayed with a line connecting the equatorward and poleward boundary during a single pass. It is seen that the equatorward boundary closely follows the variation in electrojet latitude. It therefore seems that the magnetic measurements may provide us with means to identify the equatorward boundary of the auroral acceleration and discrete auroral arcs.

In summary, these event studies indicate that magnetic field intensity observations from LEO satellite could be very useful to monitor space weather:

- It could be used to monitor the latitudinal migration of the main electrojets, both in the northern and southern hemisphere
- It could be used to monitor electrojet intensity with a high correlation to AL and AU
- It is closely associated with the various precipitation boundaries, in particular b2e measuring the latitude of the maximum average energy of electrons, and also the equatorward boundary of the electron acceleration events (discrete aurora).
- Further studies in other local time regions, and a statistical study of local time variations, however, is needed.

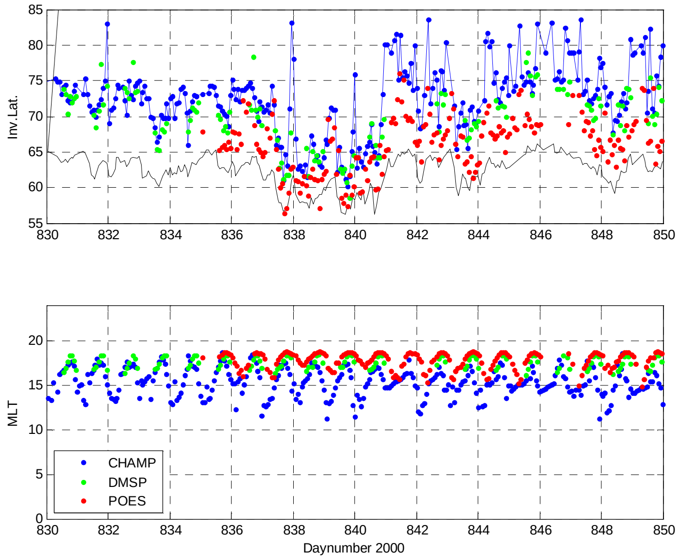

Figure 5.17 The storm event of April 2002. Magnetic and precipitation data compared.
Top: Latitude of the eastward electrojet (blue), isotropic boundary determined from POES 15 (red), maximum average electron energy boundary (b2e) determined from DMSP 13 (green) and ABI (black)
Bottom: Magnetic local time of the three satellites.

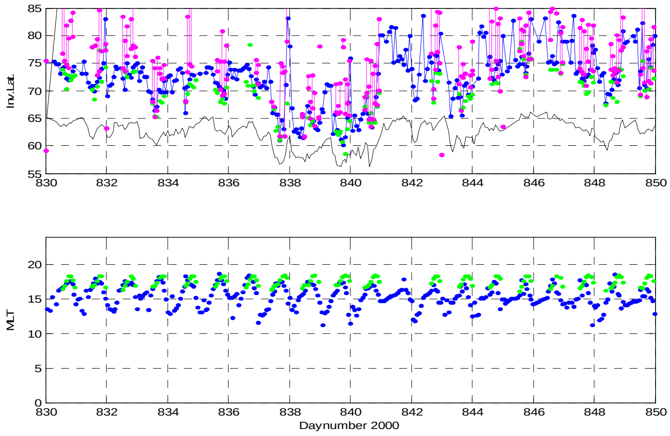

Figure 5.18 The storm event of April 2002. Magnetic and precipitation data compared.
Top: Latitude of the eastward electrojet (blue), maximum average electron energy boundary (b2e) determined from DMSP 13 (green), equatorward and poleward boundary of electron acceleration events (purple) and ABI (black)
Bottom: Magnetic local time of CHAMP (blue) and DMSP 13 (green).

5.2.3 High latitudes ionosphere

High latitudes ionosphere is highly affected by solar events that strike the Earth. During magnetic storms the energy transfer from solar wind to magnetosphere leads to enhanced polar electric fields and intensification of the polar and auroral electrojet and enhanced particle precipitation at auroral latitudes. Here we address the following question: can the auroral electrojets and particle precipitations (auroral boundary) be studied from high latitudes Total Electron Content (TEC) dynamics?

Since the advent of Global Navigation Satellites Systems, the worldwide deployment of GNSS receiver networks has been followed by numerous scientific applications. Among them the ionosphere mapping is of great interest to study geoeffectiveness of solar eruptions and high speed stream of solar wind. The International GNSS Service (IGS, http://igscb.jpl.nasa.gov/) proposes Global Ionosphere Maps (GIM), cf. Figure 5.19, with a time resolution of 2 hours and a spatial resolution of 5° for longitude and 2.5° for latitude. The geographic latitudes extend from -87.5° to 87.5°. GIM products offer the opportunity to study large scale dynamics like the equatorial fountain but also medium scale dynamics like the auroral oval.

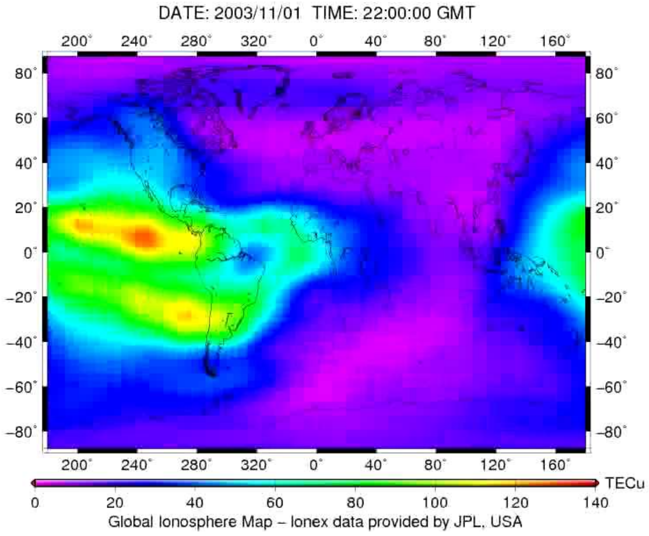

Figure 5.19 Global Ionosphere Map (GIM) from IONEX product generated by Jet Propulsion Laboratory and provided by IGS.

Here we are interested in the TEC on the night side and at high latitudes in order to focus on where particle precipitations occur and where the observation of related TEC variations is easier than on the day side. Figure 5.20 shows TEC enhancement between 20:00 and 4:00 local time at high latitudes during the Halloween 2003 storm. Night side maps have been produced by interpolation of GIM so that we generated maps with a time resolution of 6 minutes. The observation of such a pattern in TEC maps leads to a legitimate tentative: to use high latitudes TEC to estimate the equatorward auroral boundary but also to assess the mean TEC enhancement over this area.

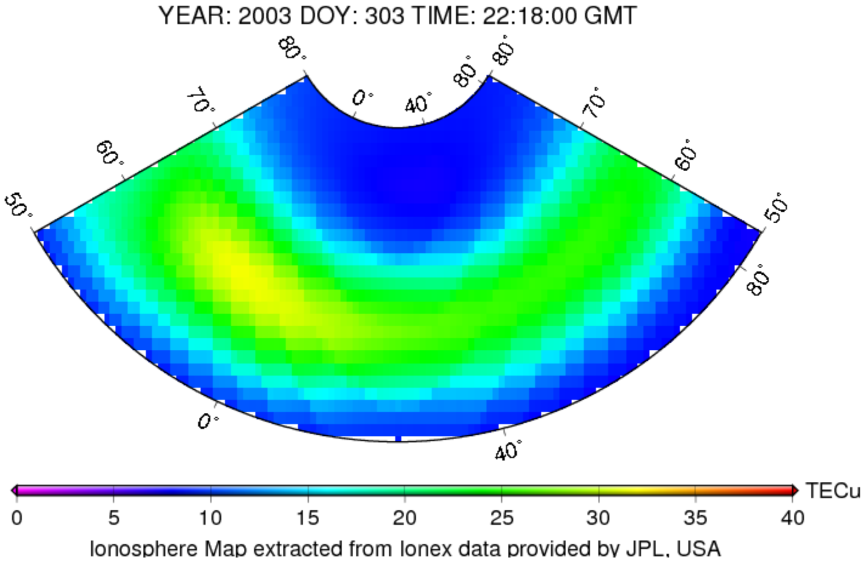

Figure 5.20: TEC map between 20:00 and 4:00 local time and 50° to 80° magnetic latitudes.

So we developed a method to compute an equatorward auroral boundary from TEC profiles at midnight. The algorithm detects the maximum value of TEC denoted "TEC max" in Figure 5.21. Then the equatorward and poleward minimum value of TEC are respectively detected ("TEC 'min'" marks). Finally the equatorward and poleward boundaries are defined as the position of the half value between "TEC max" and respective "TEC 'min'". These boundaries are noted "TEC 50% South" and "TEC 50% North". The magnetic latitude of "TEC 50% South" is the auroral boundary estimated from TEC maps called the TEC Auroral Boundary (TEC-AB). Moreover, a tracking procedure is implemented to take into account the time evolution of TEC profiles. In fact, at each time step the "TEC max" value is searched between TEC 50% South and North values of the previous instant. The use of this tracking feature showed slightly improved results.

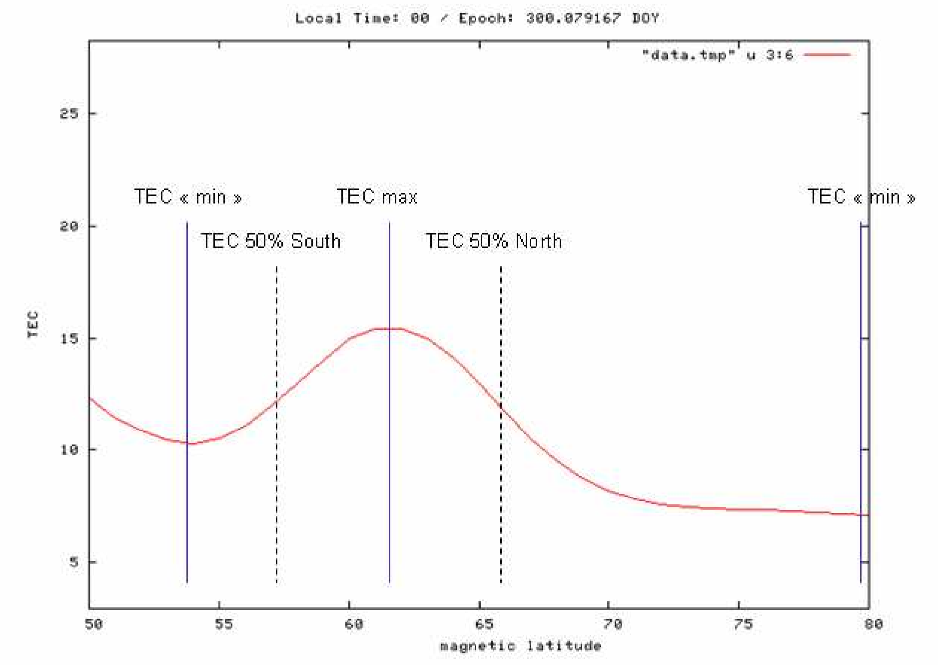

Figure 5.21 Example of midnight TEC profile and locations of “TEC max”, “TEC ‘min’”, “TEC 50% South” and “TEC 50% North”. TEC 50% South is defined as the TEC Auroral Boundary (TEC-AB).

In addition to TEC Auroral Boundary estimation we computed the mean TEC value over the whole zone defined at Figure 5.20 in order to assess the mean TEC variation at high latitudes on the Earth night side. Electron density is a key parameter of the ionosphere conductivity. Therefore the monitoring of the night side mean TEC should show coherences with auroral electrojet activity.

All these parameters have been computed for the seven solar events recalled below and described in the SOTERIA delivery D4.1:

- October 2003
- November 2003
- July 2004
- January 2005
- July 2006
- November 2006
- December 2006
- May 2007

The figures below show for each solar event the AE index (red curve top panel) provided by the Geomagnetic World Data Centre of Kyoto and the mean TEC on night side (blue curve, bottom panel) during the storm time period. Here we defined the storm time period as at least a one week window after the solar event. For longer storms the window was enlarged in order to illustrate the start and the end of the event as clearly as possible.

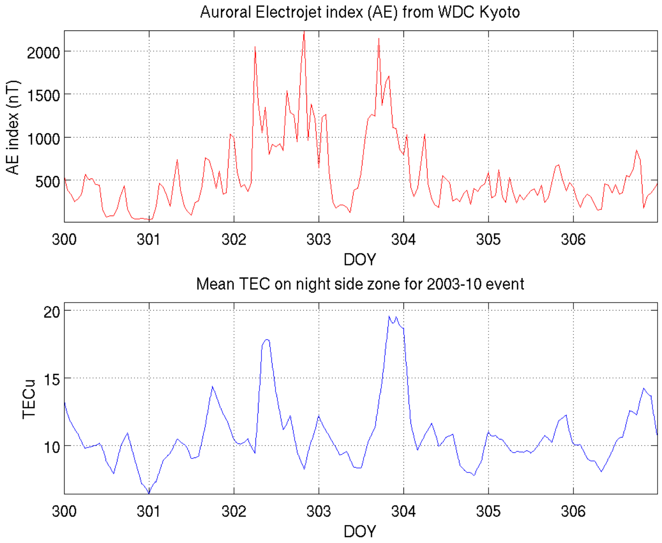

Figure 5.22 Auroral Electrojet index (red curve, top panel) and mean TEC over the night side zone [20:00 - 4:00 local time and 50°-80° magnetic latitude] from October 27 to November 02, 2003 (Day Of Year 300 to 306, ticks correspond to 00:00 UT).

For the October 2003 storm, well known as the 2003 Halloween storm, the background mean TEC value is about 10 TECu. During the early stage of the storm, afternoon of October 28, we can observe a mean TEC increase of +4 TECu just followed in the morning of October 29 by a strong and sudden enhancement of mean TEC (+7 TECu). On the same time frame the AE index becomes to increase slowly and then clearly peaks to nearly 2000 nT. A noticeable behaviour is the decrease of mean TEC to its background value while AE index stay high and even peak to its highest value. During the second event that marked this storm the TEC and AE index increases, respectively decreases, appear simultaneous.

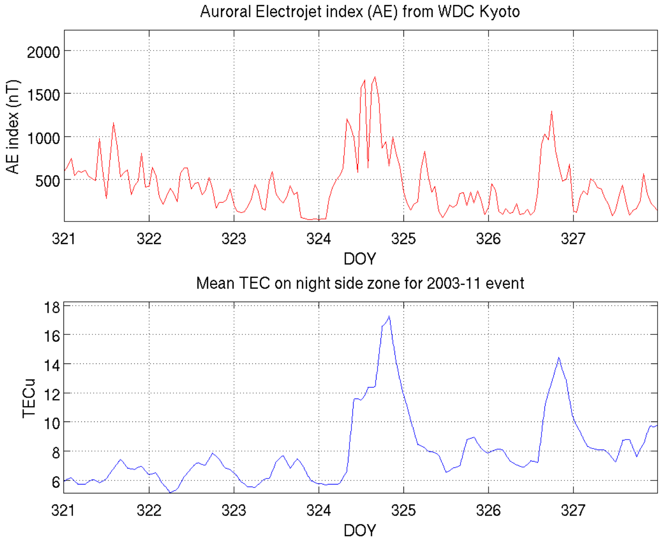

Figure 5.23: Auroral Electrojet index (red curve, top panel) and mean TEC over the night side zone [20:00 - 4:00 local time and 50°-80° magnetic latitude] from November 17 to 23, 2003 (Day Of Year 321 to 327, ticks correspond to 00:00 UT).

During the November 2003 storm the TEC and AE enhancements are quite simultaneous. We can notice the strongest TEC increase among studied storms with a jump of +11 TECu over the background value of 6 TECu during the last hours of November 20. Nevertheless, this strong TEC enhancement is correlated with a moderate AE increase reaching 1600 nT. A second storm occurs two days later with an increase of +7 TECu and to 1300 nT for TEC and AE index respectively.

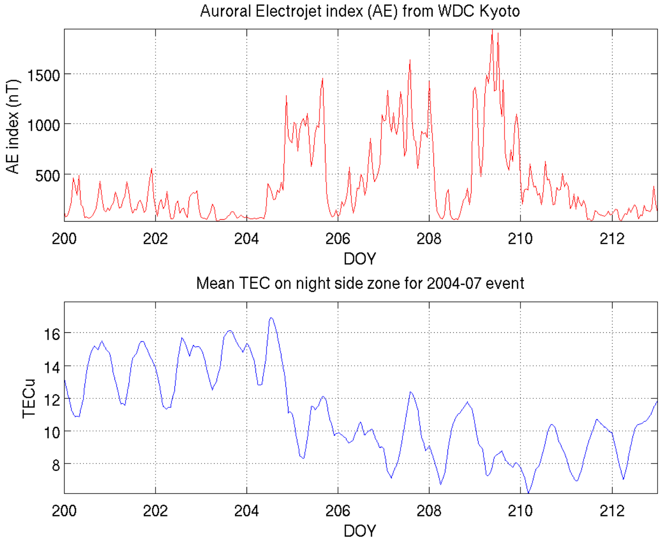

Figure 5.24: Auroral Electrojet index (red curve, top panel) and mean TEC over the night side zone[20:00 - 4:00 local time and 50°-80° magnetic latitude] from July 18 to 30, 2004 (Day Of Year 200 to 212, ticks correspond to 00:00 UT).

The July 2004 event presents the specific TEC pattern of negative ionospheric storms. It appears coherent because this type of storms occurs during summer (Prölss, 2004, Buresova *et al.*, 2007). Indeed, during the summer time, the regular wind circulation coincides with the equatorward storm-induced circulation. Therefore, the neutral gas density changes (mainly O and N2) due to energy injection at high latitudes move toward middle latitudes and induce an electron density decrease. Here, before the storms the TEC background is about 14 TECu with a slight and regular increase until 17 TECu. Then the TEC value fall down to 10 TECu at the start of the first storm. During the second storm the mean TEC seems to get a small increase with a peak value of 12 TECu and then a new fall to 8 TECu when the third storm occurs.

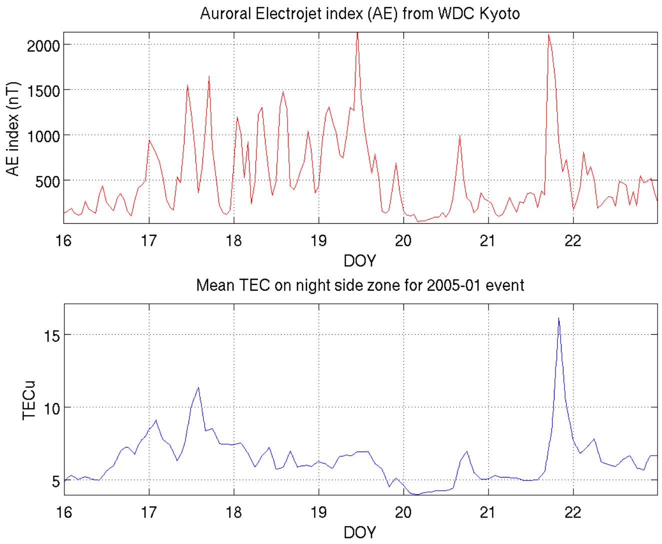

Figure 5.25: Auroral Electrojet index (red curve, top panel) and mean TEC over the night side zone [20:00 - 4:00 local time and 50°-80° magnetic latitude] from January 16 to 22, 2005 (Day Of Year 16 to 22, ticks correspond to 00:00 UT).

The January 2005 event presents two storms: the first occurs during several days with a progressive increase of intensity whereas the second one is sudden and presents a strong TEC peak. The first storm shows two TEC increases at the beginning with respectively +4 TECu and +7 TECu. TEC peaks appear to be correlated with the AE peaks. Then the TEC decreases but the AE index remains high and reaches its maximum value around 2000 nT. Second storm shows TEC and AE peaks with respective values of 16 TECu (+11 TECu) and 2000 nT.

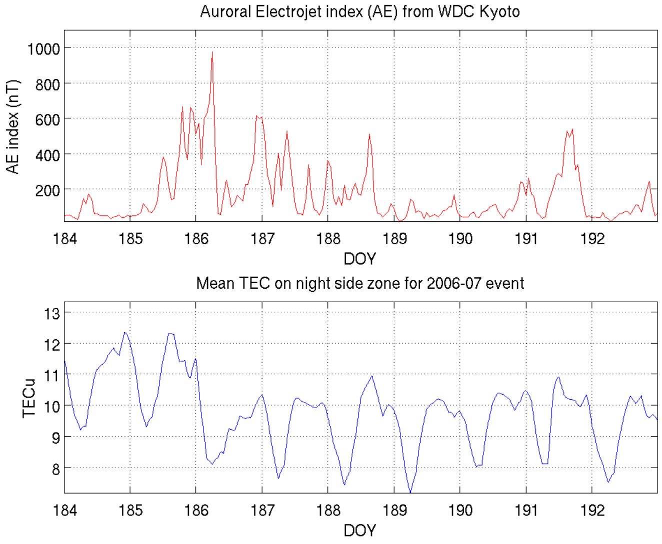

Figure 5.26: Auroral Electrojet index (red curve, top panel) and mean TEC over the night side zone [20:00 - 4:00 local time and 50°-80° magnetic latitude] from July 03 to 11, 2006 (Day Of Year 184 to 192, ticks correspond to 00:00 UT).

The July 2006 event is a negative ionosphere storm like the July 2004 storm. The difference is that the TEC decrease occurs with a delay in respect to the auroral electrojets activity increase. But it appears in phase with the maximum of auroral electrojet activity which reaches 1000 nT.

The mean TEC presents a small fall of 2 TECu that seems to remain a long time after the end of auroral electrojets disturbances. This behaviour is similar to the July 2004 storm.

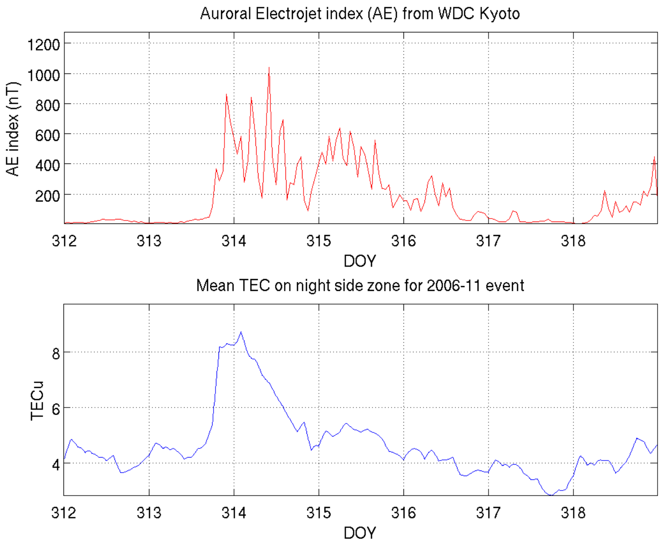

Figure 5.27: Auroral Electrojet index (red curve, top panel) and mean TEC over the night side zone [20:00 - 4:00 local time and 50°-80° magnetic latitude] from November 08 to 14, 2006 (Day Of Year 312 to 318, ticks correspond to 00:00 UT).

One particularity of the November 2006 storm is that it is a storm induced by a high speed stream arrival with Co-rotating Interplanetary Region (CIR) and not a CME-induced storm. We notice a sudden and simultaneous increase of AE index and TEC. It is similar to previous "non-negative" storms but maxima reach smaller values with +1000 nT and +4 TECu, respectively.

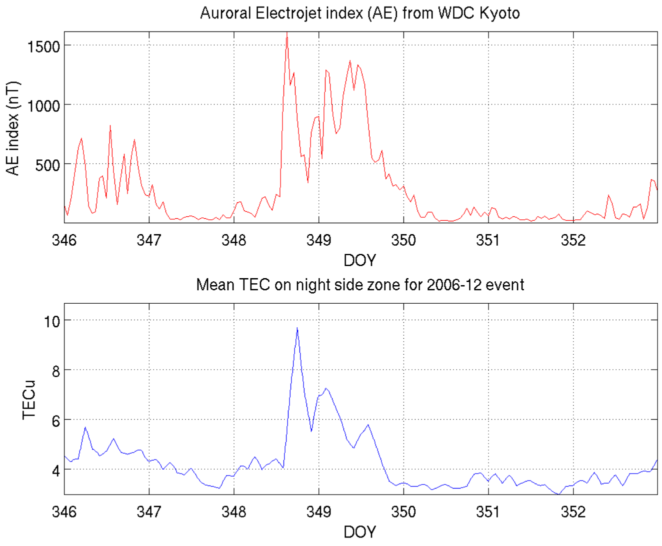

Figure 5.28 Auroral Electrojet index (red curve, top panel) and mean TEC over the night side zone [20:00 - 4:00 local time and 50°-80° magnetic latitude] from December 12 to 18, 2006 (Day Of Year 346 to 347, ticks correspond to 00:00 UT).

The December 2006 event is a storm with sudden start for auroral electrojets activity and night side mean TEC. They reach values of 1500 nT and 10 TECu with increases of +1400 nT and +6 TECu, respectively.

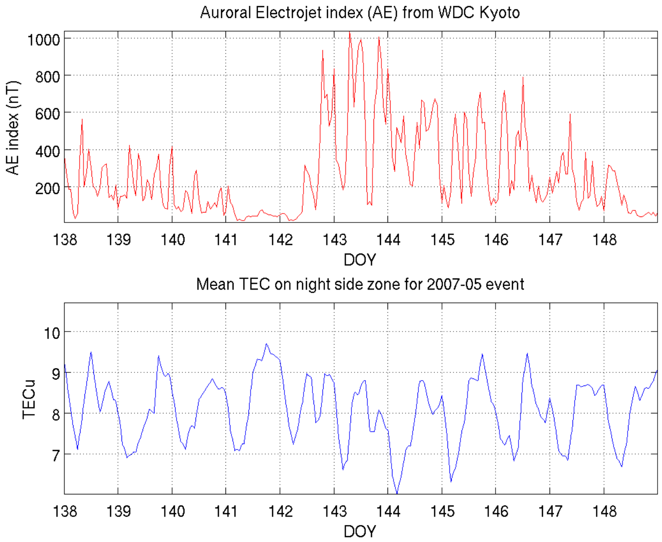

Figure 5.29 Auroral Electrojet index (red curve, top panel) and mean TEC over the night side zone [20:00 - 4:00 local time and 50°-80° magnetic latitude] from May 18 to 24, 2007(Day Of Year 138 to 148, ticks correspond to 00:00 UT).

The May 2007 storm seems to be a negative ionosphere storm which is coherent with the month of occurrence. But the TEC decrease is small with a change that appears to be around -1 TECu. Moreover the lowered mean TEC value remains several days after the end of the electrojets activity for the two other negative storms of the study whereas here TEC seems to recover its background value at the middle of the period of disturbed AE index. Finally this ionosphere storm is difficult to be analyzed more accurately because of the small TEC change and the occurrence of perturbations during the days before the identified storm. So we use only May 21 (day of year 141) to define the TEC background value whereas several quiet days would have been helpful.

Table 5.1 Synthesis of AE index and mean TEC peaks and disturbed period duration for all the studied solar events.

Event Date – Storm number	Max. AE index (variation) in nT	High AE index period	Max. mean TEC (variation) in TECu	Disturbed TEC period
2003/10 – 1	2000 (+1500)	~24 hours	17 (+7)	< 6 hours
2003/10 – 2	2000 (+1800)	< 24 hours	20 (+10)	< 6 hours
2003/11 – 1	1500 (+1500)	< 24 hours	17 (+11)	< 24 hours
2003/11 – 2	1300 (+1200)	< 24 hours	14 (+7)	< 12 hours
2004/07 – 1	1500 (+1500)	< 12 hours	10 (-4)	N/A
2004/07 – 2	1600 (+1600)	< 24 hours	N/A	N/A
2004/07 – 3	2000 (+2000)	< 24 hours	8 (-2)	N/A
2005/01 – 1	1500 (+1300)	~3 days	11 (+6)	~3 days
2005/01 – 2	2000 (+1700)	< 3 hours	16 (+11)	< 3 hours
2006/07	1000 (+1000)	~3.5 days	10 (-2)	> 7 days
2006/11	1000 (+1000)	~3 days	8 (+4)	> 1 day

2006/12	1500 (+1500)	~1.5 day	10 (+6)	~1.5 day
2007/05	1000 (+1000)	~5 days	8 (-1)	< 3 days

To conclude on the comparison between Auroral Electrojets index and mean TEC variations, we summarized few characteristics in Table 5.1. First, we have to warn that all values are defined from the analysis of the presented curves and not from rigorously computed procedures. So the accuracy is limited but is enough for the purpose. Moreover for negative ionosphere storms, the estimation of mean TEC values from curve is complex because of an apparent daily oscillation of a few TECu that is not present for events occurring during winter period (except for the November 2003 event).

Similarities and differences between mean TEC variations and AE index increases appear not sufficiently systematic to allow the use of TEC as an auroral electrojets activity indicator. The results confirm the complexity of high latitudes ionosphere storms. Nevertheless, mean TEC and AE index are clearly coupled through different mechanisms.

First, **the increase of mean TEC is a good indicator of higher conductivity**, reinforcement of ionosphere currents and auroral electrojets activity development. Here, the night side region covers an area of 20 million km^2 so that an increase of +1 TECu of the mean TEC equals the injection of 2.10^{29} electrons. Figure 5.30 shows a plot of the Auroral Electrojet index increases as a function of mean TEC enhancement and demonstrates the tendency.

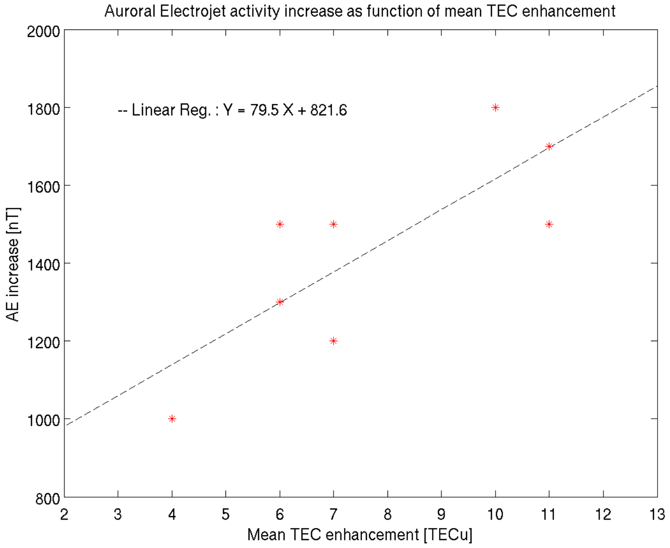

Figure 5.30 Linear regression of Auroral Electrojet index increase and mean TEC enhancement data reported in Table 5.1.

In addition **the events show a clear seasonal dependence** with the occurrence of negative ionosphere storms during summer period (enlarged from April to September) and winter period (enlarged to October to March). This behaviour was previously observed (Buresova *et al.*, 2007) within maximum electron density variations and is supported here within night side TEC average. Buresova's results and the limited number of events drove us to be careful and to interpret the results of this study as a probabilistic behaviour with respect to the season. Indeed ionosphere storms are not always strictly negative or positive and the occurrence of both phenomena is common during the different phases of ionosphere storms (Prölss, 1995).

Finally, the high latitudes mean TEC over night side region show clear but complex response to magnetic storms induced by geoeffective CME's and high speed stream arrivals. The night side TEC region defined here is coupled with the east-westward electrojet, the west-eastward electrojet and the midnight electrojet. This additional electrojet in the midnight sector is induced by current disruptions in the magnetotail and is responsible for magnetic substorms during the expansion phase of magnetic storms. **Night side TEC enhancements indicate electron precipitation and increase of electrojets activity** but the negative ionosphere storms show a limitation: non enhancement of TEC does not mean that there is no electrons precipitation.

Future works could consist in subdividing the night side region defined in Figure 5.30 in order to separate electrons precipitations' contributions and to try to point out asymmetric features in polar TEC response.

5.2.4 TEC auroral boundary

The TEC maps give also the opportunity to try to detect the auroral boundary and so to provide geographical information on particle precipitations. The figures below present the results for the equatorward auroral boundary estimation from TEC maps (TEC-AB) and a comparison with the Auroral Boundary (AB) index derived from the Defense Meteorological Satellite Program (DMSP) satellites data.

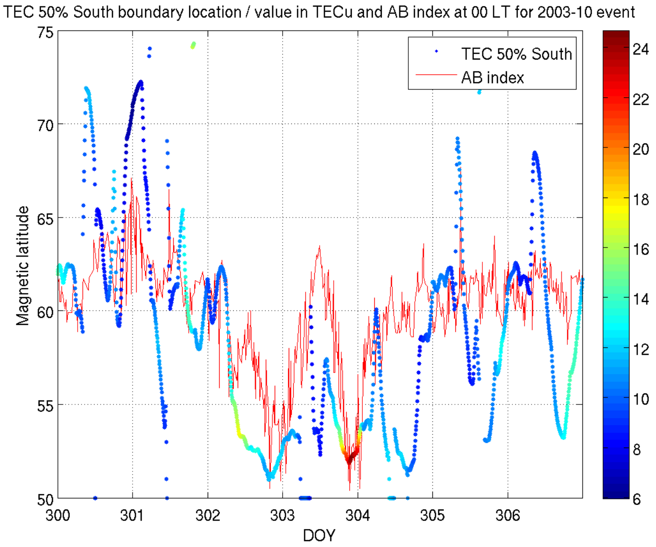

Figure 5.31 AB index from DMSP satellite (red curve) and TEC auroral boundary (dotted-coloured curve, colour bar indicates TEC value) from October 27 to November 02, 2003 (Day Of Year 300 to 306, ticks correspond to 00:00 UT).

The Halloween 2003 storm presents two strong deviations (~ -10°) of the AB index. Both reach magnetic latitude of approximately 53°. The TEC 50% south curve (TEC-AB) presents an important variability without any correlation to the AB index dynamics but, during the storm, it shows behaviour clearly coherent in respect to the AB index deviations. Moreover, we notice that coherent variations occur when the TEC value of the auroral boundary presents significant increase in comparison with TEC value before and after the period of disturbances. This is more evident for the second AB deviations than for the first one.

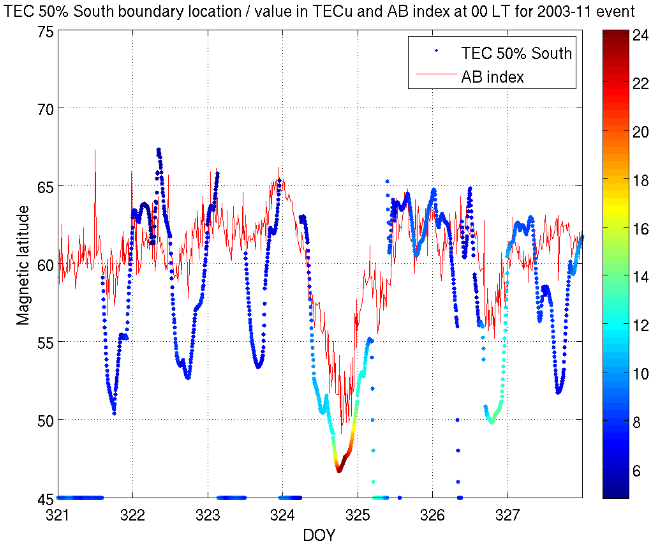

Figure 5.32 AB index from DMSP satellite (red curve) and TEC auroral boundary (dotted-coloured curve, colour bar indicates TEC value) from November 17 to 23, 2003 (Day Of Year 321 to 327, ticks correspond to 00:00 UT).

The TEC auroral boundary for the November 2003 event shows similar characteristics to the Halloween 2003 event. Indeed, the AB index presents a strong deviation (~ -15°) which is simultaneous to an equivalent TEC-AB deviation and a strong TEC value increase. In addition, a second AB index deviation, smaller than the previous (~ -7°), is also observed in the TEC-AB curve (latitude deviation and TEC enhancement) but the latitude deviation is stronger with approximately -13°.

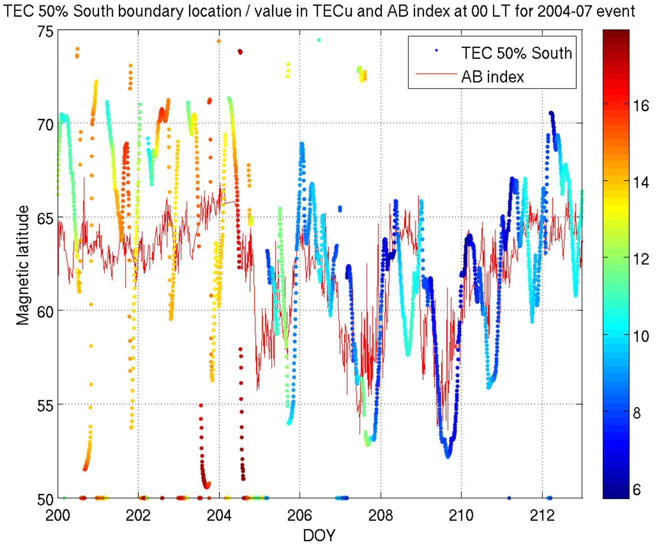

Figure 5.33 AB index from DMSP satellite (red curve) and TEC auroral boundary (dotted-coloured curve, colour bar indicates TEC value) from July 18 to 30, 2004 (Day Of Year 200 to 212, ticks correspond to 00:00 UT).

The July 2004 event presents different characteristics. First, before the 3 storms the TEC-AB curve shows extreme oscillations with high TEC values. Then the TEC-AB curve describes 3 significant negative deviations and a positive trend coherent with the AB index dynamics during the storms (doy 205 to 209) and the recovery phase (doy 210-212), respectively.

However, the TEC-AB curve doesn't show clear TEC intensifications when deviations happen. This difference with previous events is certainly due to the specificities of negative ionosphere storms.

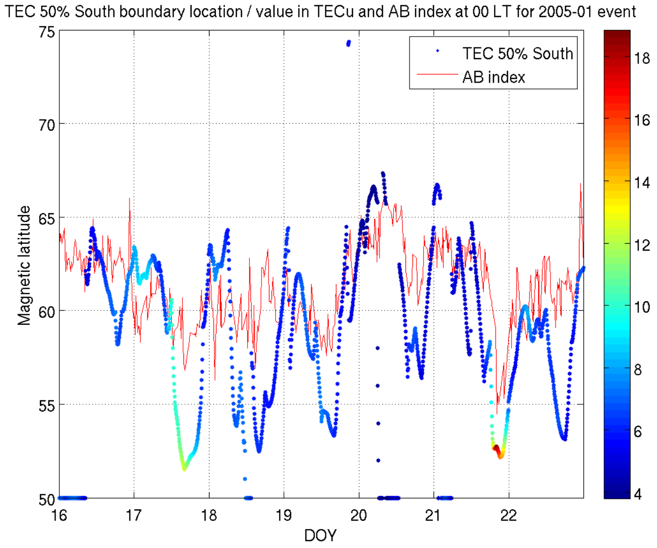

Figure 5.34 AB index from DMSP satellite (red curve) and TEC auroral boundary (dotted-coloured curve, colour bar indicates TEC value) from January 16 to 22, 2005 (Day Of Year 16 to 22, ticks correspond to 00:00 UT).

During the January 2005 event the TEC-AB curve shows two TEC intensifications with auroral boundaries around 52° of magnetic latitude. The second AB-TEC deviation is coherent with the AB index whereas the first one doesn't fit the AB index dynamics: the AB index deviation is smaller (reaching only 59°) and occur apparently during a longer period.

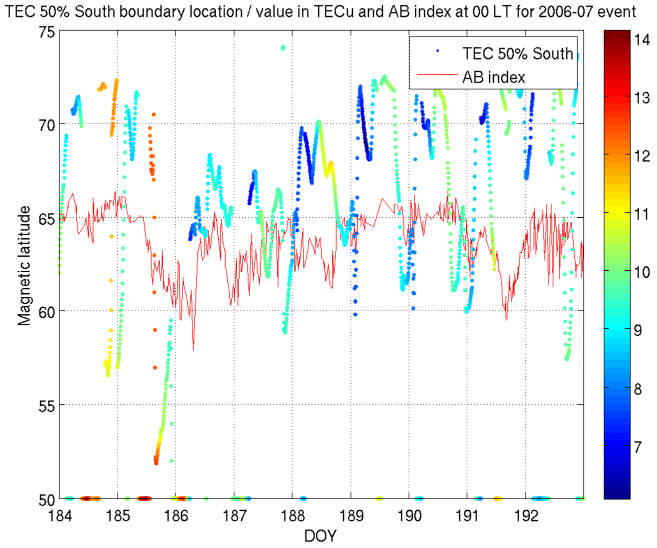

Figure 5.35 AB index from DMSP satellite (red curve) and TEC auroral boundary (dotted-coloured curve, colour bar indicates TEC value) from July 03 to 11, 2006 (Day Of Year 184 to 192, ticks correspond to 00:00 UT).

The July 2006 event is a negative ionosphere storm for which the AB index presents two small deviations (~ -5°) reaching 60° of magnetic latitude. As for the July 2004 event the TEC-

AB curve shows stronger oscillations before rather than during the storm but here the coherence between TEC-AB curve and AB index is not apparent.

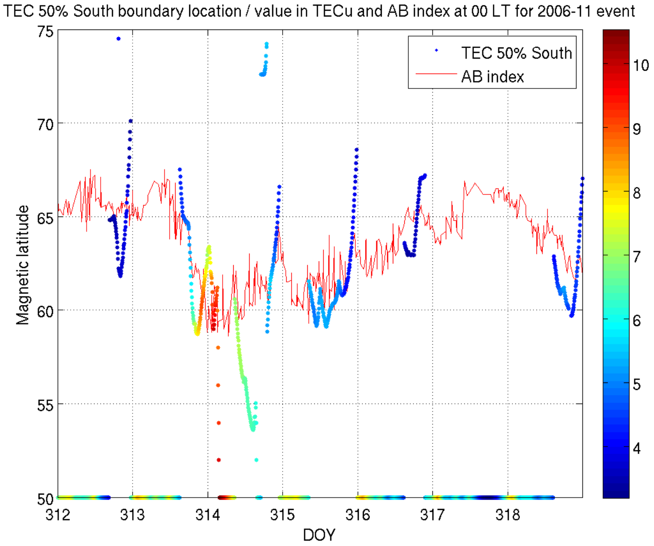

Figure 5.36 AB index from DMSP satellite (red curve) and TEC auroral boundary (dotted-coloured curve, colour bar indicates TEC value) from November 08 to 14, 2006 (Day Of Year 312 to 318, ticks correspond to 00:00 UT).

The TEC-AB detection algorithm gives poor results for the November 2006 event. However, we notice a TEC enhancement and a deviation of TEC-AB curve when AB index comes down to 60° of magnetic latitude.

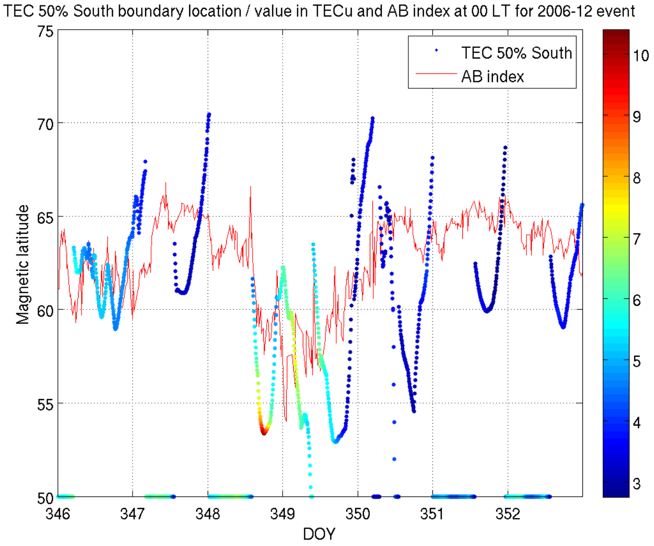

Figure 5.37 AB index from DMSP satellite (red curve) and TEC auroral boundary (dotted-coloured curve, colour bar indicates TEC value) from December 12 to 18, 2006 (Day Of Year 346 to 347, ticks correspond to 00:00 UT).

The AB index of the December 2006 event presents a strong deviation of approximately -10° reaching less than 56° of magnetic latitude. At the same time the TEC-AB curve shows TEC increase and gets down to 54° of magnetic latitude. During the first hours of the recovery phase (doy 349-350) the TEC is decreasing but remains higher than before the storm. Nevertheless, the TEC-AB estimation is quite unstable and its coherence with the AB index becomes less evident.

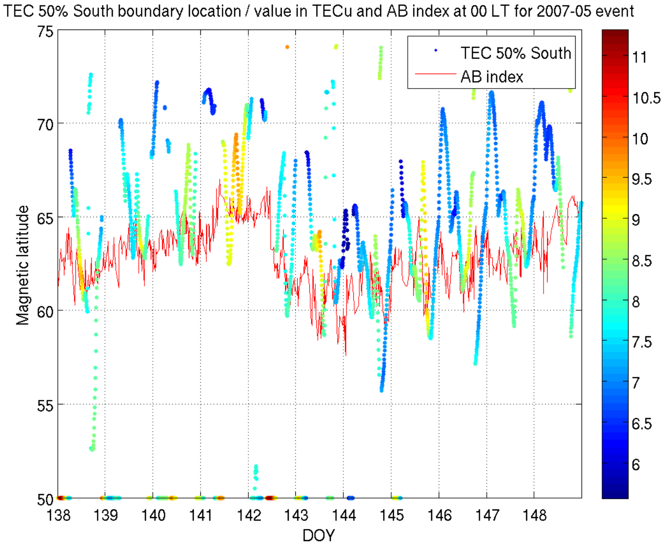

Figure 5.38 AB index from DMSP satellite (red curve) and TEC auroral boundary (dotted-coloured curve, colour bar indicates TEC value) from May 18 to 24, 2007 (Day Of Year 138 to 148, ticks correspond to 00:00 UT).

The May 2007 event shows a highly disturbed TEC-AB curve with TEC value variations impossible to interpret. This is not very surprising when comparing the results for the other negative ionosphere storms. Nevertheless, the tendency that appears in the AB index is clearly observed in the TEC-AB curve.

To conclude on the TEC-AB computation we can state that the simple method is not fully efficient but shows interesting results. The main issue is the TEC-AB strong oscillations which are not correlated with the auroral boundary index computed from DMSP data. However, the correlation between TEC-AB and AB index is greatly improved if we consider the total electron content at the auroral boundary latitude too. **Indeed the combination of strong deviation and TEC enhancement demonstrates the occurrence of particle precipitation and enlargement of the auroral oval confirmed by the AB index. Moreover, the TEC-AB latitude is generally close to the AB index latitude**. Here, we have to note that negative ionosphere storms present a different response. TEC increases are not of interest because they do not exist and the continuous oscillations of TEC-AB curve are still present. Nevertheless, if we look at the envelopes of the TEC-AB curve we can note the tendencies follow the AB index tendency during the storms. This is clearly observed for the July 2004 and May 2007 events.

6. Effects on spacecraft and on space instruments

6.1. Radiation belts effects on the functioning of the TESIS and SPHINX instruments on-board CORONAS-Photon and comparison of the measured data with the SPENVIS model predictions

6.1.1 Introduction

Space instruments on LEO satellites are operated under impact of various environmental factors which should be taken into account to prevent distortion of the observational data. Some of these factors provide cumulative effects which may reduce the useful operational time of the instrument. For solar space instruments intended for imaging and photometry in the XUV and EUV spectral ranges, the most important effect is the flux of charged particles on the near-Earth orbits which produce spontaneous background and degradation of the detectors. The radiation component includes quasi-stationary fluxes of energetic charged particles – protons and electrons of the radiation belts, transient fluxes of the high energy particles generated by the Sun during the activity events and galactic cosmic rays. The values and relation between radiation field components depend on coordinates and height of the satellite, season, daytime and vary during the solar activity cycle.

The Earth environment is very sensitive to solar activity, but physical mechanisms of its influence are not completely known because of lack of observational information. Several semi-empirical models have been developed to calculate parameters of the environment in space and time and to forecast their possible consequences in relation with the orbit of the satellite and specific design properties of the instrument.

The SPENVIS model is a WWW-based instrument intended to facilitate the use of models of the spatial environment in a consistent and structured way (http://www.spenvis.oma.be/). The SPENVIS system consists of an integrated set of models of the space environment, and a set of help pages on both the models and the SPENVIS system itself.

For the purposes of the current report, models of radiation sources and effects are the most important, in particular AE-8 and AP-8 models and models to calculate the impact of these fluxes on real electronic system or component (SHIEDOSE, NIEL). For practical application and improvement of the SPENVIS model it is very important to make a comparison of the predicted values with the data obtained under different conditions in real experiment.

Below, in the chapters 6.1.1 - 6.1.5 we describe the design of the TESIS and SPHINX instruments for the radiation dose estimations, the radiation effects in the TESIS solar images and in the SPHINX data, estimation of the averaged daily radiation dose per one CCD pixel from the TESIS data and its comparison with the SPENVIS predictions.

6.1.2 TESIS and SPHINX instruments aboard CORONAS-Photon

CORONAS-Photon

The CORONAS-Photon satellite was launched 31 January 2009 and actively operated for 10 months till 30 November 2009 when it was terminated because of failure of the electric power system. It operated in the LEO orbit with the initial parameters: apogee 575 km, perigee 550 km, inclination 82.5 deg. The initial orbital period was 95.66 min.

Fig. 6.1 CORONAS-Photon prepared for the launch at the Plesetsk cosmodrome. The arrow points to the TESIS instrument.

The scientific payload consisted of 12 instruments, the biggest and the most informative was the TESIS telescope designed by LPI (Figure 6.1). The goals of the mission are: the investigation of accumulation of the magnetic field energy and its transformation into energy of accelerated particles during solar flares; the study of the acceleration mechanisms, propagation and interaction of fast particles in the solar atmosphere; the study of the solar activity correlation with physical-chemical processes in the Earth upper atmosphere.

TESIS

TESIS is a complex of several EUV telescopes, EUV spectroheliographs (Kuzin et al., 2009, 2010, http://tesis.lebedev.ru/en/) including as one of the measuring channels the SPHINX X-ray spectrophotometer developed by the SRC PAS team (Wroclaw, Poland). The structural diagram of TESIS and its model for radiation hardness evaluation are drawn in Figure 6.2. The basic characteristics of the channels are given in Table 6.1.

The equivalent thickness of shielding estimated from thicknesses of the TESIS structure elements around the CCD corresponds to 3 g/cm^2 (12 mm of Al). The SPHINX detectors have shielding of 1 g/cm^2 (4 mm of Al). The satellite fully screens the TESIS instrument from the back (see Fig. 6.1), which decreases the solid angle for penetrating energetic particles to 2π.

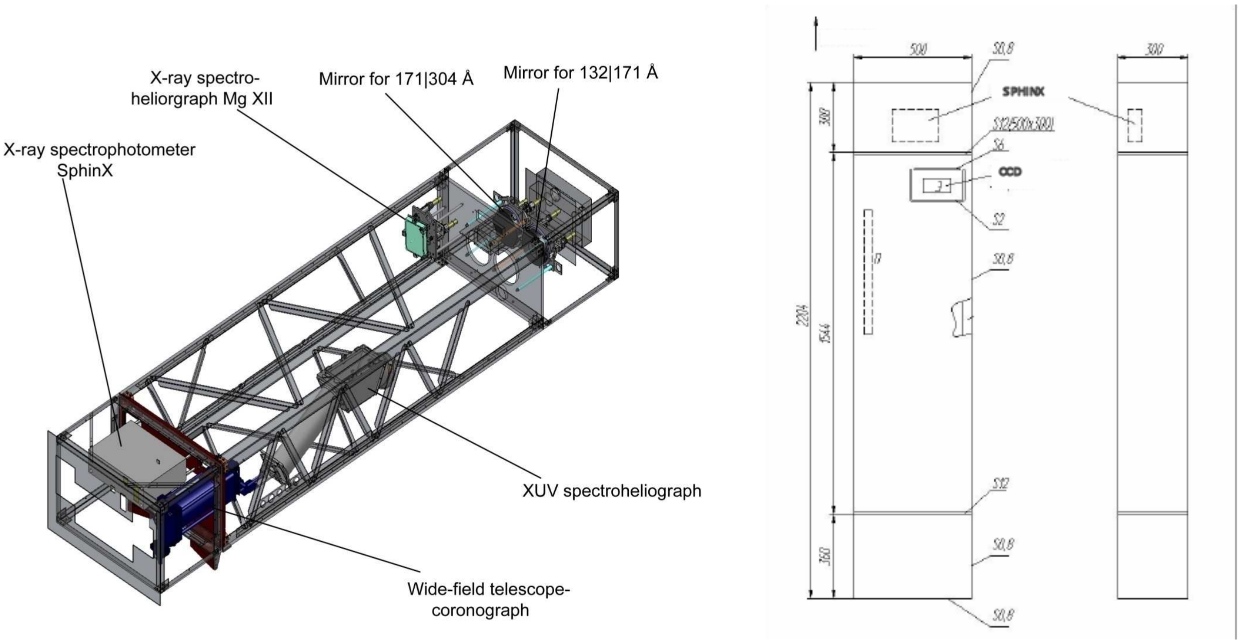

Fig. 6.2 TESIS structure diagram and the dimensional model for radiation hardness estimations

Table 6.1 Main parameters of TESIS

Register channel	Optical scheme	F, mm	Angular size	Field of view	Selectivity, $\lambda/\Delta\lambda$	Dominant ions	Mirror shape	Mirror diameter, mm
13.2/17.1	Herschel	1600	1.74	1	≈26 (13.2 nm)	Fe XIX, Fe XX, Fe XXIII (13.2 nm)	Off-axis parabola	∅100
					≈28 (17.1 nm)	Fe IX (17.1 nm)		
17.1, 30.4	Herschel	1600	1.74	1	≈28 (17.1 nm)	Fe IX (17.1 nm)	Off-axis parabola	∅100
					≈30 for (30.4 nm)	He II, Si XI (30.4 nm)		
30.4	Spectroheliograph	600	4.6 (along and ⊥ dispersion)	2	≈7	Fe XV, Ni XVIII, Si IX, Ca XVIII, Si XI, He II, Mg VIII and others	Parabolic	∅80
30.4	Ritchey–Chretien	600	4.6	2	≈7	He II, Si XI	Parabolic	Primary – 80/20, secondary – 40/10
0.84	Spectroheliograph	1200	2.3	1.3		Mg XII	Spherical	120 × 80

The imaging channels of TESIS have back-illuminated CCD-detectors built by "e2v " company with 2048x2048 pixels sized 13.5×13.5 μm. Depletion depth of the CCD is 20 *μm*. One of the detectors is shown in Figure 6.3. The factor of conversion of photoelectrons to DNs is equal to 10 DN/e.

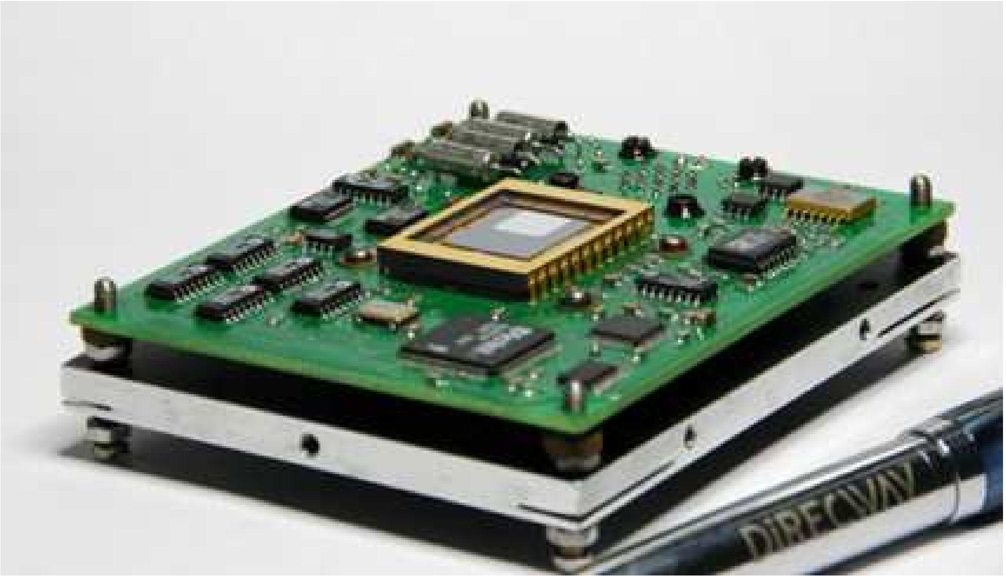

Fig. 6.3 A view of the TESIS flight CCD-detector

SPHINX (SRC PAN)

The SphinX instrument (Sylwester et al., 2008, Gburek et al., in press) consists of three Peltier-cooled PIN diodes (D1, D2, D3) placed behind precisely measured apertures with areas 21.50, 0.495, and 0.0101 mm^2 and are sensitive to 1—15 keV (0.08—1.0 nm) X-rays, similar to the emission in the *GOES* longer-wavelength channel. The PIN detectors, manufactured by Amptek (Bedford, Mass.), are silicon, 500 μm thick PIN diodes, with 12.5 μm beryllium entrance windows. SphinX was calibrated to better than 5% accuracy using BESSY II synchrotron (in Berlin) and XACT facility in Palermo, Italy. Spectral resolution (FWHM) of the detectors is 490 eV, the full energy range is divided into 256 energy bins.

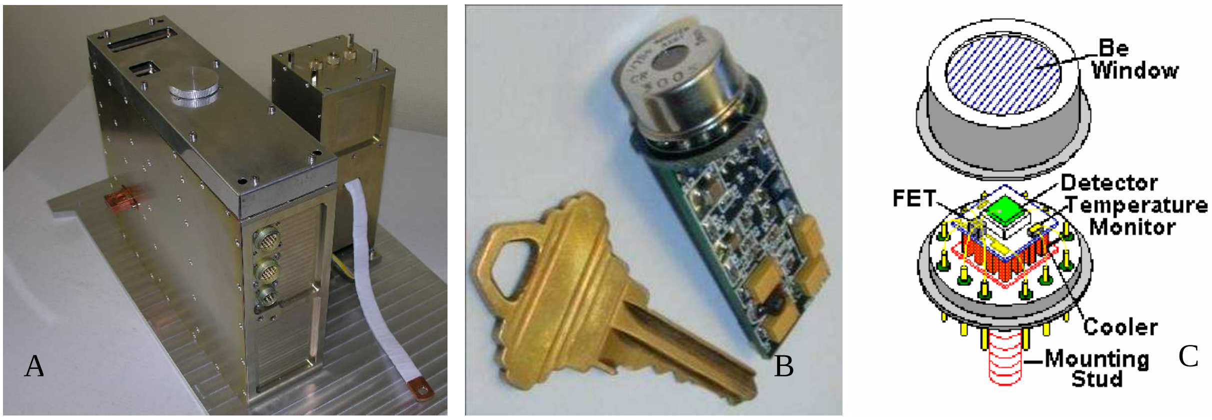

Fig. 6.4 A view of the SPHINX measuring unit (A) and X-ray detectors (B, C).

The main design parameters of the SPHINX detectors are: D1: S= 25 mm^2, thickness 500 μm, τ=8 μs, FWHM: 490 eV, D2: S= 13 mm^2, thickness 500 μm, τ= 25 μs, FWHM: 290 eV.

6.1.3 Radiation effects in the solar EUV images registered by the TESIS telescopes

In the standard synoptic mode TESIS registered solar images continuously during the daytime part of each orbit (45-47 min) with a cadence of 2.5 – 5 min (in accordance with available free telemetry volume). The imaging process included the shutter opening, the exposure, the shutter closing and readout. The exposure times for different channels varied from 0.1 to 10 s, the readout lasted 2.5-5 s depending on the selected data compression algorithm.

During the total acquisition time (exposure+readout) the TESIS detectors were sensitive to the energetic charged particles – electrons and protons which penetrated to the detectors through the satellite and instrument shielding. The charged particles interacted with silicon of the depletion zone and produced tracks in the registered images (Figure 6.5).

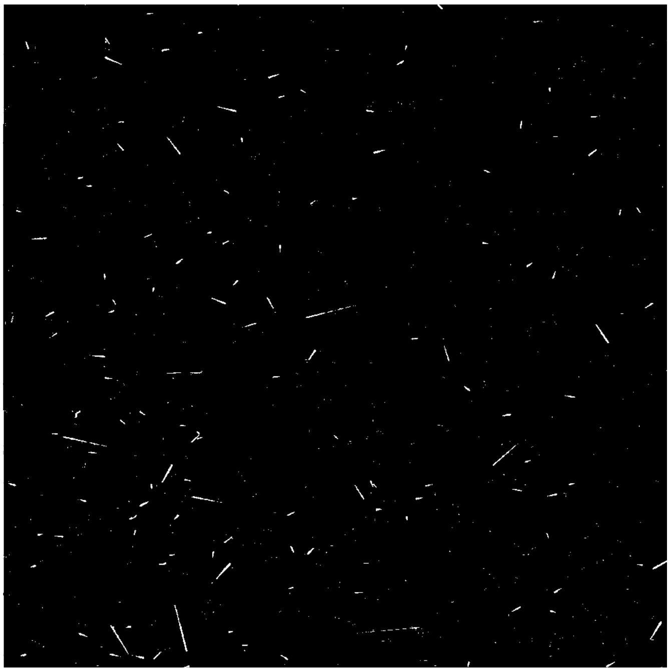

Figure 6.5 Tracks in the CCD image produced by the energetic charged particles. The TESIS 171 A channel, exposure time 3 s.

As follows from the global distribution (see below), the tracks are mostly produced by protons. A proton looses its energy providing electron-hole pairs with a binding energy of 3.65 eV. The ionization losses of protons non-linearly depend on their energy: the most of the energy releases in the end of the absorption path (see Appendix I). A track length depends on absorption path and angle of incidence. Protons produce the brightest tracks if their absorption paths are fully located within the depletion layer. Tracks with L=38 – 190 μm correspond to protons with energies E_p=2 – 5 MeV.

When moving along the orbit, all TESIS detectors registered tracks in dependence on geographic coordinates, date and daytime. For the analysis we selected images taken in the TESIS Mg XII channel from 1 to 14 June 2009. This channel was designed to obtain images of the Sun in the resonant Mg XII line 8.42 A (E=1.4 keV) which is excited only in the hot solar plasma with the temperature of 5-15.10^6 K. During the period of observations the Sun was extremely quiet, and this channel registered only background and tracks of charged particles. A special software has been developed to process the images and to detect tracks.

Figure 6.6 shows a number of tracks registered in the MgXII images from 1 to 14 June 2009 as a function of time. Exposure time is 100 s. The biggest peaks correspond to South Atlantic Anomaly - SAA (80% of the total intensity). The mean rate of tracks averaged over all time is

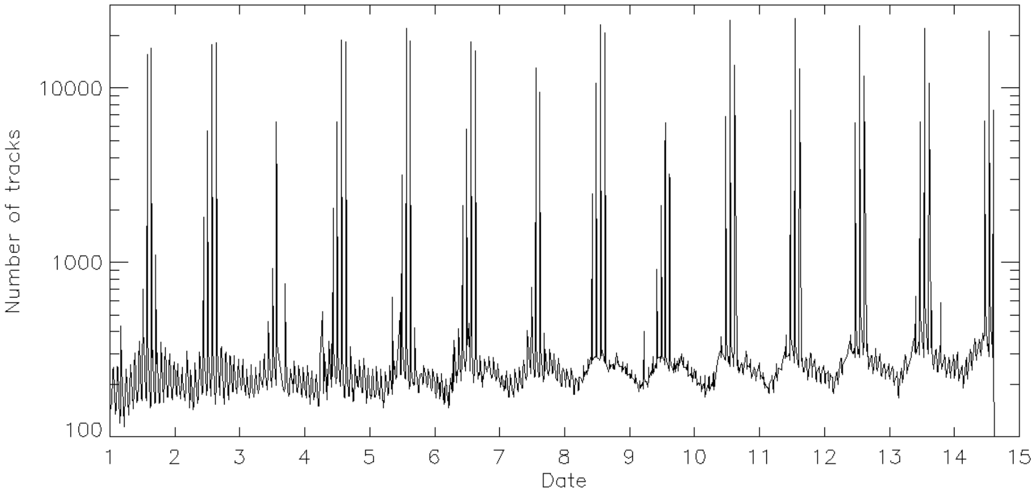

Fig. 6.6 Temporal distribution of the tracks count rate for the period of observations. The biggest peaks correspond to the South Atlantic Anomaly region (SAA).

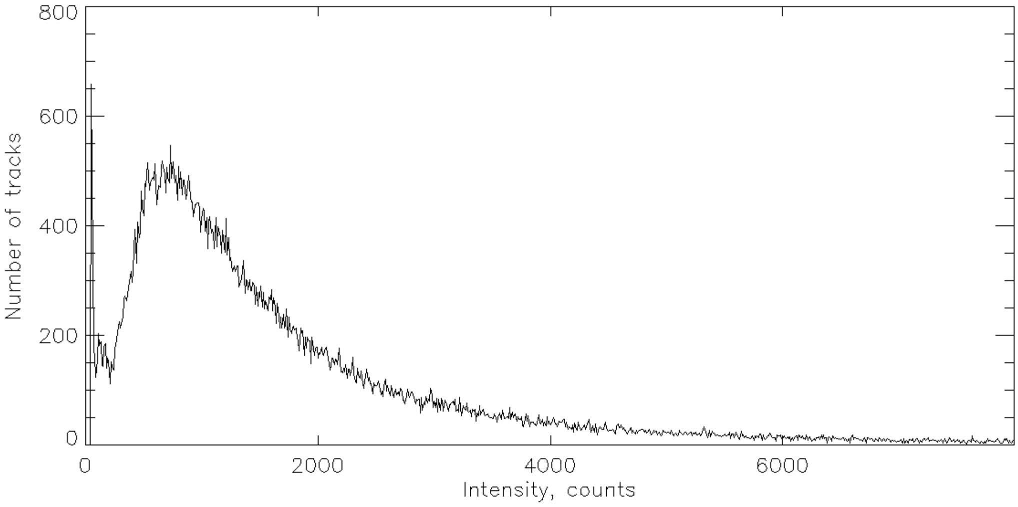

Fig. 6.7 Distribution of the tracks on their total intensity (in DNs).

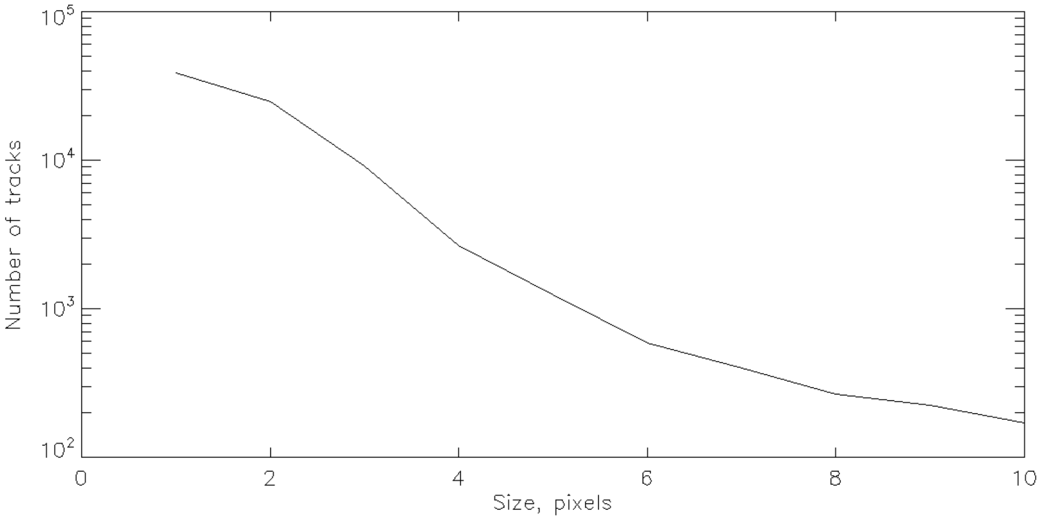

Fig. 6.8 Distribution of tracks on size (in CCD pixels)

0.029 DN/s. Figures 6.7 and 6.8 show the distributions of the tracks on the total intensity and the length. According to these data, the mean energy released in tracks:

$$<I>\sim 600 \text{ DN}*10e*3.65 \text{ eV} \sim 2.2.10^4 \text{ eV}= 3.5.10^{-8} \text{ erg}$$

The mean value of track projections: <p> ≈ 2 pix=27 μm. Max p ≈ 10 pix=135 μm. For omnidirectional angular distribution of the falling particles the mean track length L:

$$<L>= p\sqrt{2} = 38\mu m$$

Figure 6.9 shows a global distribution of the track numbers in the single image. Almost all tracks were registered in the SAA region. No detectable signal was registered in the polar regions.

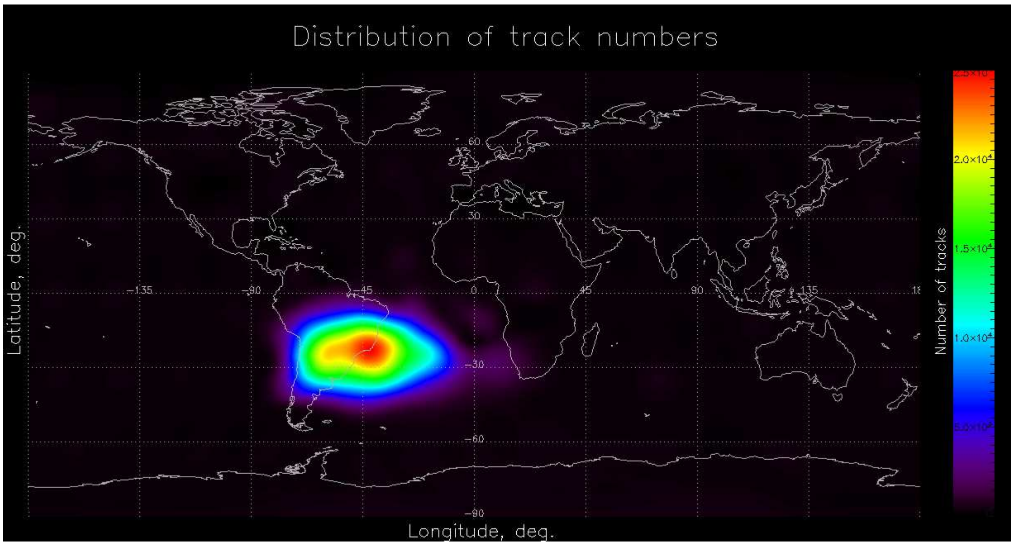

Fig. 6.9 Distribution of the track numbers over the globe.

The comparison with the SPENVIS model calculations (section 6.1.4) shows that this distribution is similar to that of the trapped protons on the CORONAS-Photon orbit. So, the registered tracks are mainly produced by protons of the radiation belts.

The anisotropy of the track distribution on angle between the detector plane and the direction of the local magnetic field is shown in Figure 6.10.

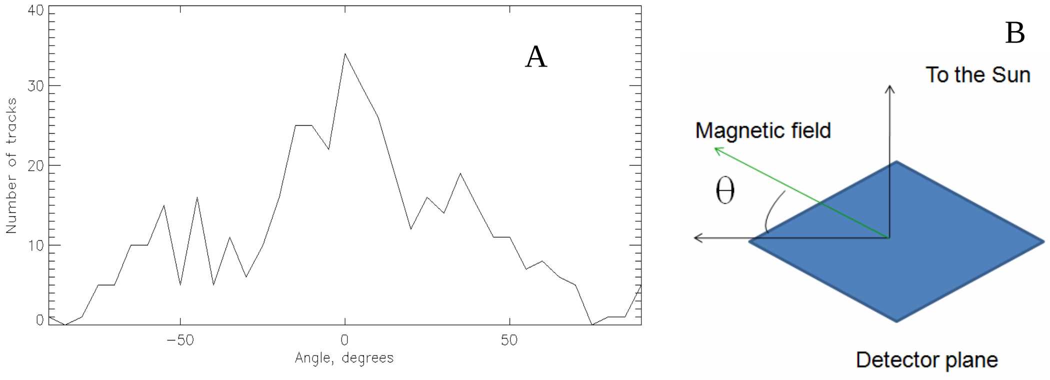

Fig. 6.10 Anisotropy of the track distribution (A) on angle between the detector plane and the direction of the local magnetic field (B).

6.1.4 PB effects in the SPHINX data

A light curve of the SPHINX signal for several orbits obtained on May 9, 2009 is shown in Figure 6.11.

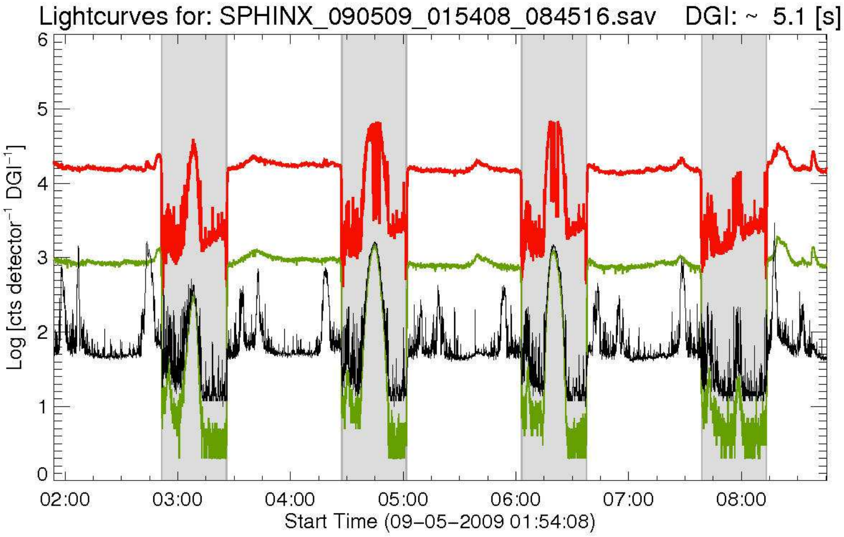

Fig. 6.11 SPHINX signal along the CORONAS-Photon orbit

The SPHINX data are available from the site:
http://156.17.94.1/sphinx_catalogue/SphinX_cat_main.html

All available SphinX particle records from detectors D1 and D2 have been examined in order to identify particle fluxes observed in South Atlantic Anomaly SAA, north radiation belts NRB, south radiation belts SRB. Also areas where no increased particle signal was observed were examined to determine the background level in SphinX detectors. All data when atypical instrument operation was found (observations after SphinX resets, time intervals when detectors temperature was increased etc.) were rejected from the analysis. Also data obtained during intense solar events were not considered in this study. A global distribution of the particle background (PB) signal after reconstruction of the Earth's particle environment from the SphinX D2 detector is shown in Figure 6.12.

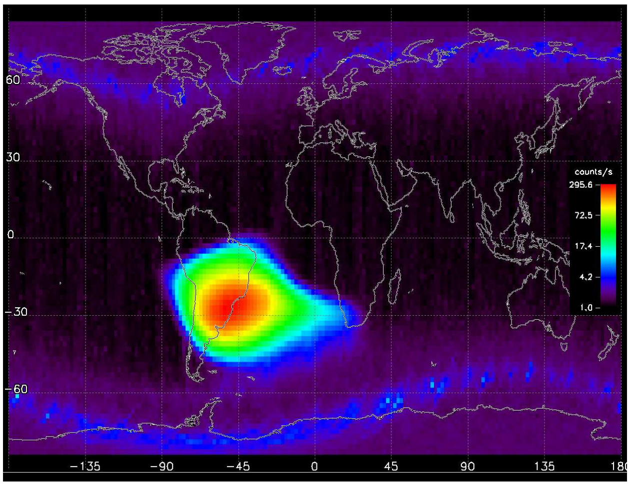

Fig. 6.12 Reconstruction of Earth's particle environment from SphinX D2 detector.

The selected data were analyzed in order to check if X-ray flux observed by SphinX instrument depends on the angle between the front surface of the SphinX Si detectors and the direction of the Earth local magnetic field vector at the instrument position in orbit. Orientation of the front surface of SphinX detectors is orthogonal to a vector $\boldsymbol{v}$ pointing from the satellite to the Sun (within the spacecraft pointing accuracy). Such a vector was determined from the spacecraft orbital position, obtained using two line orbit elements, and the respective position of the Sun at any given time moment in the scope of the study.

The magnetic field vector $\boldsymbol{B}$ was calculated using internal component of the Earth magnetic field provided by the International Geomagnetic Reference Field IGRF model:
http://wdc.kugi.kyoto-u.ac.jp/igrf/

The angle $\boldsymbol{\alpha}$ between $\boldsymbol{v}$ and $\boldsymbol{B}$ vectors was defined by the equation $\boldsymbol{\alpha} = \arccos(\boldsymbol{v}\bullet\boldsymbol{B})/|\boldsymbol{B}| - 90°$, where $\bullet$ stands for scalar product. Such definition gives angle of -90° when vectors $\boldsymbol{v}$ and $\boldsymbol{B}$ are parallel and points to the same direction, 0° when $\boldsymbol{v}$ and $\boldsymbol{B}$ are orthogonal and +90° when $\boldsymbol{v}$ and $\boldsymbol{B}$ are parallel but its orientation is opposite.

Next, the dependences of SphinX observed particle signal on the angle $\boldsymbol{\alpha}$ in north radiation belt NRB, south radiation belt SRB and South Atlantic Anomaly SAA areas have been analyzed. The SphinX particle flux was averaged over 1° angle bin and the time of the mission duration for all the three regions NRB, SRB and SAA. A background observed outside NRB, SRB and SAA has been subtracted. The results are shown in histogram plots in Figures 6.13, 6.14 and 6.15.

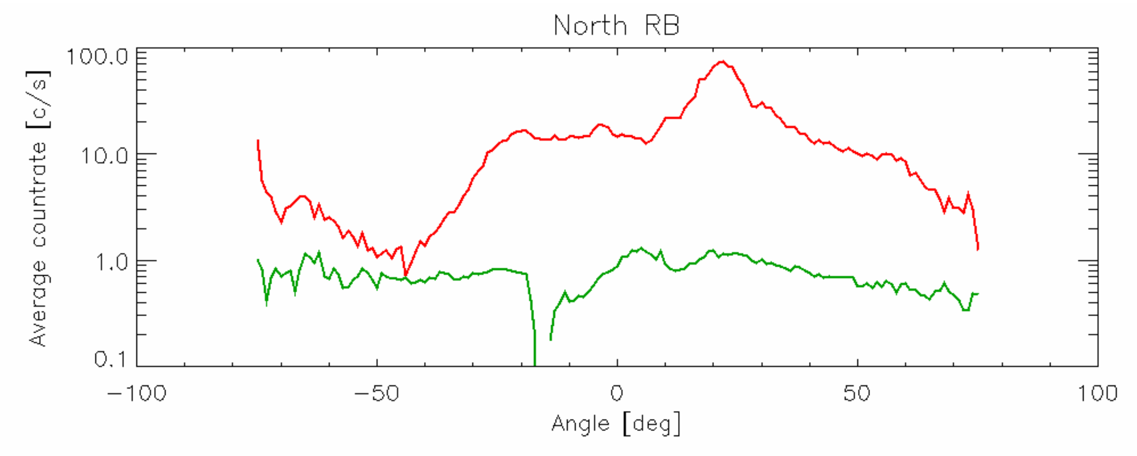

*Fig. 6.13 Dependence of the SphinX observed flux on angle **α** as seen in the northern polar oval. Flux in SphinX detector D1 – red line, the flux in the SphinX detector D2 – green line*

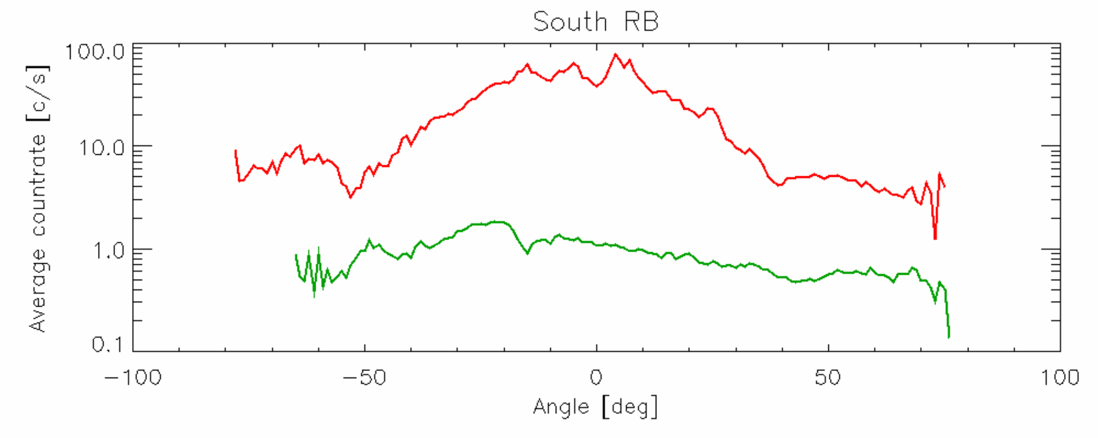

*Fig. 6.14 Dependence of the SphinX observed flux on angle **α** as seen in the southern polar oval. Flux in SphinX detector D1 – red line, the flux in the SphinX detector D2 – green line*

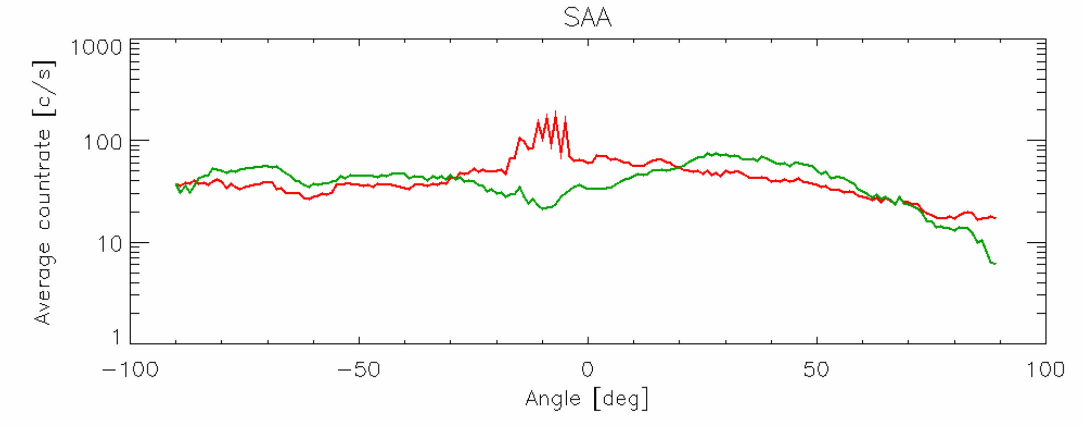

*Figure 6.15 Dependence of SphinX observed flux on angle **α** as seen in SAA. Flux in SphinX detector D1 – red line, flux in SphinX detector D2 – green line*

There is some increase of the particle flux observed in the SphinX D1 detector in NRB around **α** ≅ 25° and in SRB around **α** ≅ 0°. The SAA plots show increased particle flux for the D1 detector and decrease in D2 what is hard to explain.

Generally, the obtained results are difficult to interpret. Many factors here come into play. Results may depend on particle energy, strength of magnetic field, magnetic field model used, pointing accuracy etc. Further works to understand the results of this study are necessary.

6.1.5 Estimations of the RB effects using the SPENVIS model

We used the SPENVIS models (http://www.spenvis.oma.be/) to predict the radiation conditions on the CORONAS-Photon orbit during the development phase of the CORONAS project. In order to run these models, a spacecraft trajectory is needed. At the first step the "orbit generator" was run. The orbital parameters before the CORONAS-Photon flight were taken from the orbit of the previous CORONAS-F satellite which had near the same orbit. During the CORONAS-Photon flight the real orbital data in the two-element .tle format were taken from the site: http://www.space-track.org.

Then, to determine the initial radiation conditions, we took the electron and proton spectra using the AE-8 electron model and AP-8 proton model for the solar minimum (Figure 6.16). Figure 6.17 presents the global distributions of the electron and proton fluxes calculated for 5 mission segments from 1 to 14 June 2009.

For the purposes of this report, we estimated the radiation dose for the mission segments selected above using the SHIELDOSE model (Figure 6.18).

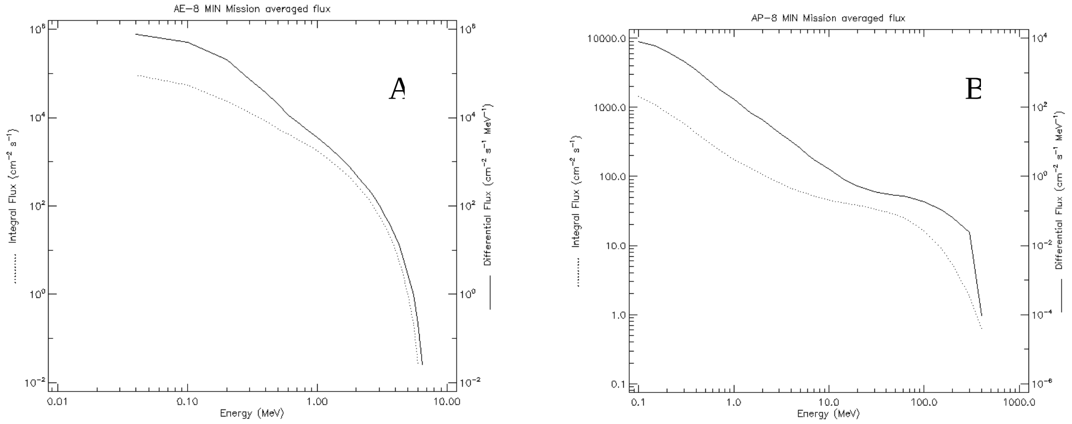

Figure 6.16 Initial spectra of trapped electrons (A) and protons (B) for solar minimum

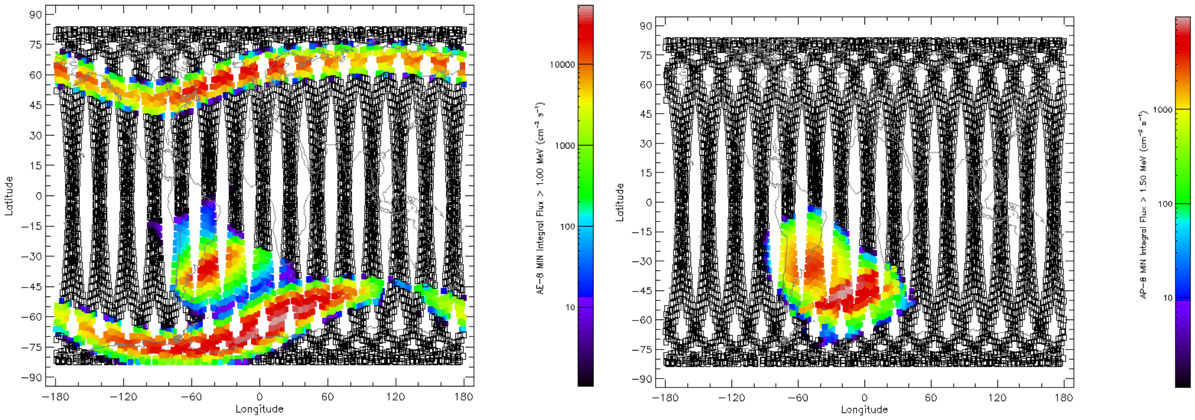

Figure 6.17 Global distributions of the trapped electrons (left) and protons (right) on the CORONAS-Photon orbit

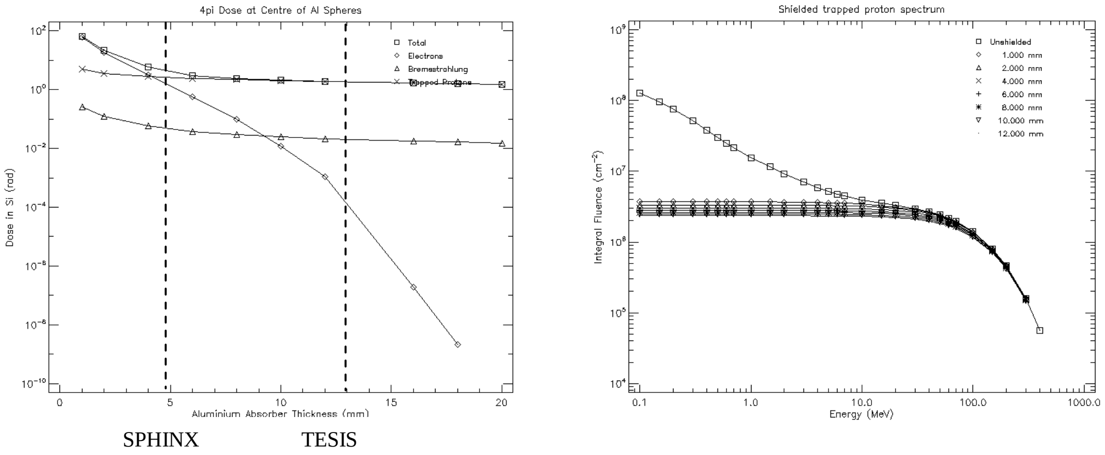

Figure 6.18 Attenuation of trapped protons and electrons by the TESIS shielding (left); the spectrum of the trapped protons penetrated the shielding (right) for the mission segment 1 (June 1, 2009, duration 1 day). The shielding values for TESIS and SPHINX detectors are indicated by the dashed lines.

6.1.6 Comparison of the accumulated radiation dose of the trapped protons from the TESIS tracks with the SPENVIS model calculations

The temporal variation of the total track intensity determined from the TESIS data and normalized to 1 CCD pixel for 1 day intervals from 1 to 14 June 2009 is shown in Figure 6.19. The averaged value of the total track intensity recalculated for the one day exposure time is T_1 = 2534 DN/pix/day.

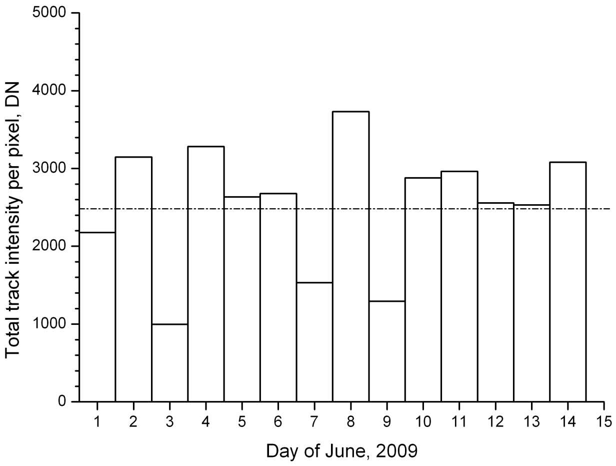

Fig. 6.19 Temporal variation of the total daily track intensity per 1 pixel.

The corresponding deposited energy equals:

(Eq. 6.1) $$E_1 = T_1 \cdot K_e \cdot 3.65ev$$

where K_e is the coefficient of conversion of electrons to DNs. For the TESIS CCD, K_e=10 (e/DN). The radiation dose D_{TESIS} accumulated in one pixel during 1 day in rad units (1 rad=100erg/1g):

(Eq. 6.2) $$D_{TESIS} = \frac{E_1 * 1.6.10^{-12}}{100 * m_1} = 6.87.10^{-5} T_1 \quad (rad),$$

where the pixel mass $m_1 = 8.49 \bullet 10^{-9} g$.

Substituting the value of T_1 in Equation 6.2, the averaged radiation dose per one CCD pixel per on day exposure time from the TESIS data was found to be: D_{TESIS} = 0.174 rad/day. The results of using SHIELDOSE model for calculation of the radiation dose for the CORONAS-Photon orbit are shown in Table 6.2.

Table 6.2 The results of the SPENVIS calculations of the radiation dose for the CORONAS-Photon orbit

Trapped particle dose (rad) for mission segment 1 (1 day)							
Al absorber thickness			Tr. el.+Bremss. +Tr. protons	Trapped electrons	Brems-strahlung	Tr. electrons+ Bremsstrahlung	Trapped protons
(mm)	(mils)	(g cm^{-2})					
12.000	472.440	3.240	0.3212	1.725E-04	3.556E-03	3.729E-03	0.3175

To compare this value with the TESIS data we should take into consideration that TESIS is shielded from one side by the spacecraft body, so:

$$D_{Spenvis} = 0.3212*(2\pi/4\pi) = 0.161 \text{ rad/day} .$$

The SPENVIS result well agrees (within 10%) with the TESIS value, so we can conclude that in our case the SPENVIS gives very reliable predictions.

6.1.7 Conclusions

1. TESIS and SPHINX data contain the information about fluxes of charged particles (trapped protons and electrons) of the radiation belts at the CORONAS-Photon orbit during the solar minimum (period February – November 2009).
2. In the TESIS images charged particles (mostly protons) produce tracks in the depletion layer. In the SPHINX data particles (protons and electrons) produce current pulses. In both cases intensities of the signal are proportional to the fluxes of the radiation belt particles.
3. Most of the particle signal in TESIS comes from the South Atlantic Anomaly. SPHINX was measuring particle background in the SAA and also in polar ovals.
4. Accumulated dose from radiation belt protons per day in the TESIS CCD detector is within 10% agree with estimation by the SPENVIS model for the solar minimum.
5. Anisotropy in the signal distribution on angle between the magnetic field and the detector plane in TESIS most probably can be explained by a non-uniform distribution of the shielding mass.
6. In SPHINX, the anisotropy of the signal is different in the polar regions and in SAA which may be partly explained by a non-uniform angular distribution of the trapped radiation belt particles.

6.1.8 Appendix

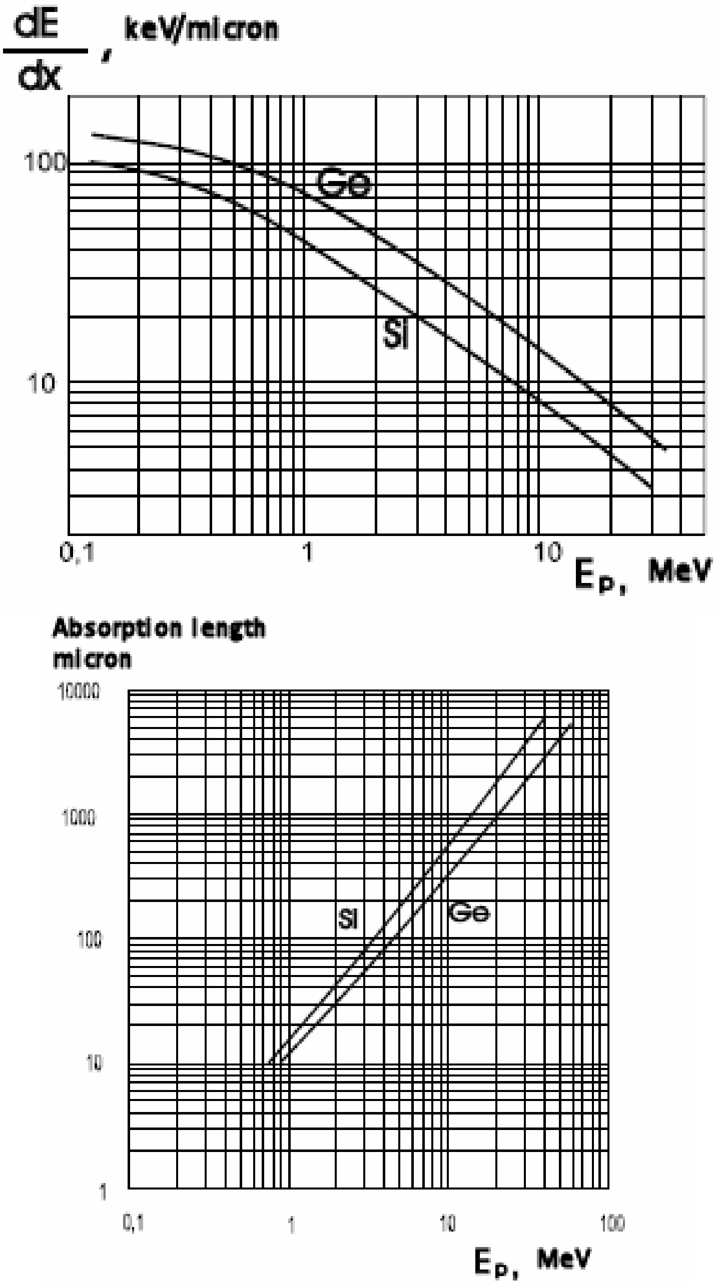

Fig. 6.20 Energy losses and absorption length of protons in germanium and silicon

6.2 Calibrating energetic particle fluxes measured by the NOAA/POES satellites

One of the longest datasets of energetic particles in the Earth’s magnetosphere has been measured by the NOAA/POES (Polar Orbiting Environmental Satellites) satellite program which has been operational since 1978, covering nearly three complete solar cycles. The time coverages of the different NOAA/POES satellites that have measured energetic particles are depicted in Figure 6.2.1 with reference to solar cycles. The NOAA/POES satellites orbit the Earth on nearly circular polar orbits with a nominal altitude of about 850 km and an orbital period of about 102 min. The orbital planes relative to the Sun-Earth line stay relatively constant ("Sun synchronous") although over a period of several years the orientation of the orbital planes of some satellites rotates significantly.

The NOAA/POES satellites include a SEM (Space Environment Monitor) instrument package, which is designed to monitor the Earth's space environment and consists of two separate instruments to measure charged particles: TED (Total Energy Detector) and MEPED (Medium Energy Proton Electron Detector). The energetic particle measurements provided by the MEPED instrument of the SEM package have been used, e.g., to study particle precipitation in the auroral zone (e.g., Wissing et al., 2008), to construct radiation belt models (e.g., Fung et al., 1996; Huston et al., 1996), to study magnetic storm dynamics (e.g., Søraas et al., 2002, 2004; Asikainen et al., 2005), the South Atlantic Anomaly and the inner radiation belts (e.g., Asikainen and Mursula, 2005, 2008). Accordingly, the NOAA/POES dataset is one of the most important energetic particle datasets in space physics.

Almost a decade ago it was noticed that the particle detectors onboard the NOAA/POES satellites showed clear signs of instrument degradation due to radiation damage, leading to erroneous fluxes and artificial long-term trends (Galand and Evans, 2000, McFadden et al., 2007). Signs of radiation damage typically become significant a couple of years after satellite launch, while the data in the beginning of the operational period of each satellite are fairly reliable (with the exception of NOAA-14 whose MEPED instrument showed erroneous fluxes from the beginning of the mission). Although the problem of instrument degradation has been known for a long time, no documented systematic attempt has been done so far to correct the measurements. We have recently studied the degradation of the MEPED detectors and presented the calibrated fluxes of energetic protons for the whole NOAA/POES satellite series (Asikainen and Mursula, 2010).

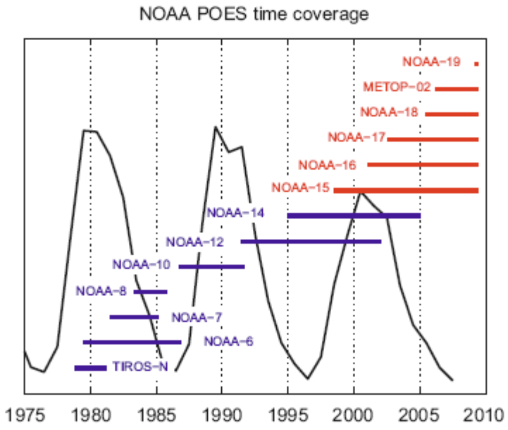

Figure 6.21 Time coverage of NOAA/POES satellites in relation to the solar cycles.

6.2.1 NOAA/MEPED detectors

The satellites up to NOAA-14 used the SEM-1 instrument package while NOAA-15 and later satellites carry an improved version of the instrument called SEM-2. The TED instrument measures auroral particles with energy below 20 keV, and the MEPED (Medium Energy Proton Electron Detector) measures energetic electrons in three integral energy channels with energy ranging from 30 keV to 2.5 MeV, and energetic protons in six (in SEM-1 only five) differential energy channels with nominal energy ranging from 30 keV upwards. The energy ranges of the MEPED instrument are given in Table 6.3. The MEPED protons and electrons are measured in two nearly orthogonal directions with a sampling time of 2 sec. The local vertical detector, the so called 0^o detector points away from the Earth along the radial Earth-satellite line (-X axis in satellite coordinate system). In SEM-2 the local horizontal detector, the so called 90^o detector points antiparallel to spacecraft velocity vector (towards +Y axis in satellite coordinate system). This orientation of the detectors means that at high latitudes, where the magnetic field lines near the Earth are nearly radial, the 0^o detector measures field-aligned precipitating particles and the 90^o detector measures locally trapped particles. At low latitudes the situation is different so that the 90^o detector measures field-aligned particles (either precipitating or upflowing, depending on the direction of satellite motion and the hemisphere) and the 0^o detector measures locally trapped particles. The measured count rates (particles/sec) are converted to physical fluxes (particles/(cm^2 sr s)) by dividing with the geometric factor G of the detector. For SEM-1 the geometric factor is G=0.0095 cm^2 sr and for SEM-2 G=0.01 cm^2 sr. A more detailed description of the SEM-1 and SEM-2 instruments is given by Hill et al. (1985), Seale and Bushnell (1987), Raben et al. (1995), and Evans and Greer (2000).

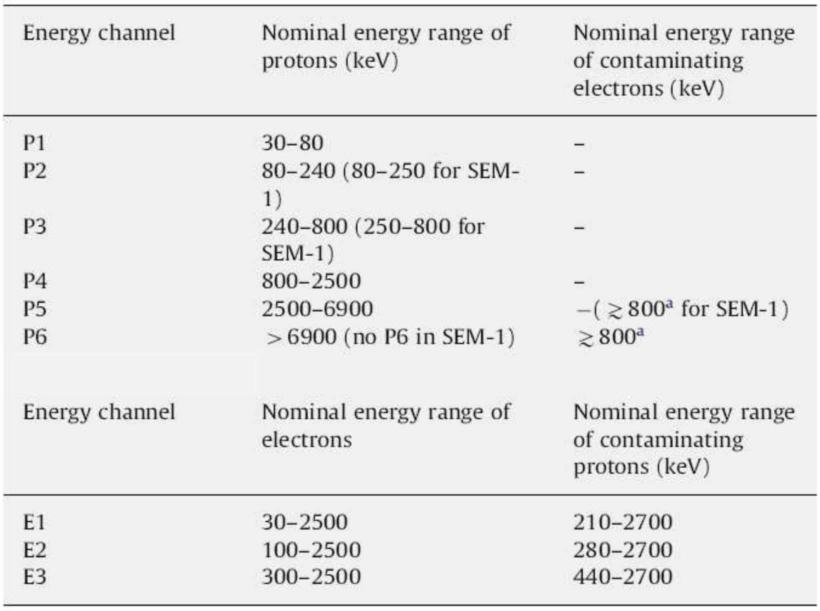

Energy channel	Nominal energy range of protons (keV)	Nominal energy range of contaminating electrons (keV)
P1	30–80	–
P2	80–240 (80–250 for SEM-1)	–
P3	240–800 (250–800 for SEM-1)	–
P4	800–2500	–
P5	2500–6900	–($\gtrsim 800^a$ for SEM-1)
P6	> 6900 (no P6 in SEM-1)	$\gtrsim 800^a$

Energy channel	Nominal energy range of electrons	Nominal energy range of contaminating protons (keV)
E1	30–2500	210–2700
E2	100–2500	280–2700
E3	300–2500	440–2700

Table 6.3 Nominal energy ranges of the MEPED SEM-2 instrument. Energy ranges for SEM-1 are the same except when indicated otherwise in parenthesis. P-channels refer to protons and the E-channels to electrons. Both detectors are sensitive to both particle species to some degree.

6.2.2 Effect of radiation on MEPED

The MEPED electron and proton detectors are solid state silicon detectors based on pulse-height analysis. In such a detector a charged particle penetrating the detector chip loses some or all of its kinetic energy and produces free charge carriers (electrons and holes) in the silicon lattice. The number of produced free charges is directly proportional to the kinetic energy lost by the incoming particle. The detector electronics collects the charge produced in the silicon chip within some integration time (85 ns in MEPED) and the charge is transformed to a voltage pulse whose amplitude is recorded. This pulse amplitude is a measure of the kinetic energy of the incoming particle. By counting the number of pulses and their heights every other second, alternately for 0^o and 90^o detectors (a full data cycle of 0^o and 90^o detectors takes 2 sec since counting electronics is shared between the two detectors), MEPED obtains the energy distribution of incoming particles which then can be used to sort particles into respective energy channels with specific thresholds given in Table 6.3.

It is well known that silicon detectors are prone to radiation damage caused by the incoming energetic particles and ionizing electromagnetic radiation (see e.g., Grupen and Schwartz, 2008). In order to minimize the effect of solar radiation, the MEPED detectors are covered by a thin metal film (aluminium in proton detectors and nickel in electron detectors) which stops most of the harmful electromagnetic radiation, still allowing particles to enter the detectors. Accordingly, the radiation damage of the MEPED instrument is caused by the very same particles that it measures. The incoming particles, e.g., create defects in the silicon lattice that reduce the mobility of the free charge carriers. Consequently, the amount of charge collected during the instrument integration time is reduced and thus the energy of the incoming particle is underestimated. Accordingly, as radiation damage progresses, particles need more and more energy to be detected in a given channel. In the present analysis we denote by α_i the factors by which the lower energy threshold of the *i*th energy channel has increased from the nominal value given in Table 6.3. It is important to note that the α_i factors are not constant but change in time.

The α_i factors for a given satellite can be estimated by comparing the measurements of the satellite with those of a newly launched satellite where radiation has not yet damaged the instruments. The comparison between the two satellites makes sense only when the satellites are roughly in the same region of space roughly at the same time. We have done the comparison between a new satellite and the old degraded satellites using satellite conjunctions where the latitudinal and longitudinal difference between the satellites is $< 1^o$, the relative difference between the satellite L-values is less than 10%, and the time difference between the measurements is less than 30 s. The conjunctions must occur within five months from the launch of the new satellite. Each 2 s measurement from one satellite is compared to each measurement of the other satellite. This typically yields some 100 comparisons for a single conjunction and typically we obtain several tens of conjunctions between any two satellites.

Let us now compare the measurements of two satellites in detail, and estimate the α factors. Let the integral proton energy spectrum measured by the newly launched satellite be

$$F_n(E) = \int_E^\infty f_n(E')dE',$$

where the index *n* refers to 'new' satellite and $f_n(E)$ is the differential energy spectrum. We assume that $F_n(E)$ is the true integral spectrum that should be sampled by both satellites. If we now assume that in the degraded satellite the energy threshold of the *i*'th channel has increased by a factor of α_i we can express the measured integral flux above energy $\alpha_i E_i$ as

(Eq. 6.3) $$F_n(\alpha_i E_i) = \frac{1}{G_o}\sum_{k=i}^{5} N_{o,k}$$

where the index *o* refers to 'old' satellite and $N_{o,k}$ is the count rate measured by the degraded old satellite at channel *k* and G_o is the geometric factor of the instrument which converts the count rate to flux. We can solve α_i from Equation 6.3 by expressing the integral spectrum $F_n(E)$ as a interpolating cubic polynomial in log-log scale determined by the fluxes observed by the new satellite. The α_i factor is then solved numerically from Equation 6.3 for different energy channels. Figure 6.22 shows graphically how the α factors are determined by finding the energy in the spectrum of the new satellite where the fluxes match those of the old satellite. The depicted spectra are examples of real measurements.

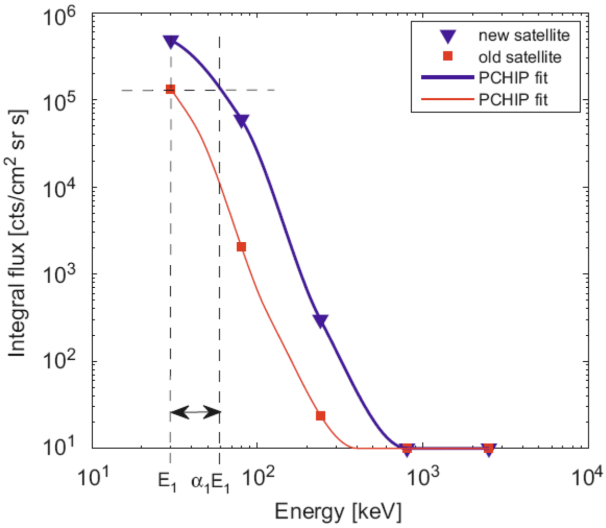

Figure 6.22 Determining the α factors by finding the energy in the spectrum of the new satellite where the fluxes match those of the old satellite.

Figure 6.23 shows the α factors of the three lowest energy channels of NOAA-15 as a function of time. The α factors are shown for 90° (red) and 0° (blue) detectors. The curves in the plots show cubic polynomial fits to the α factors determined at specific times. For NOAA-15 one can especially see that the 90° detector degrades faster (the α factors increase faster) than the 0° detector. This is because the 90° detectors measure larger fluxes.

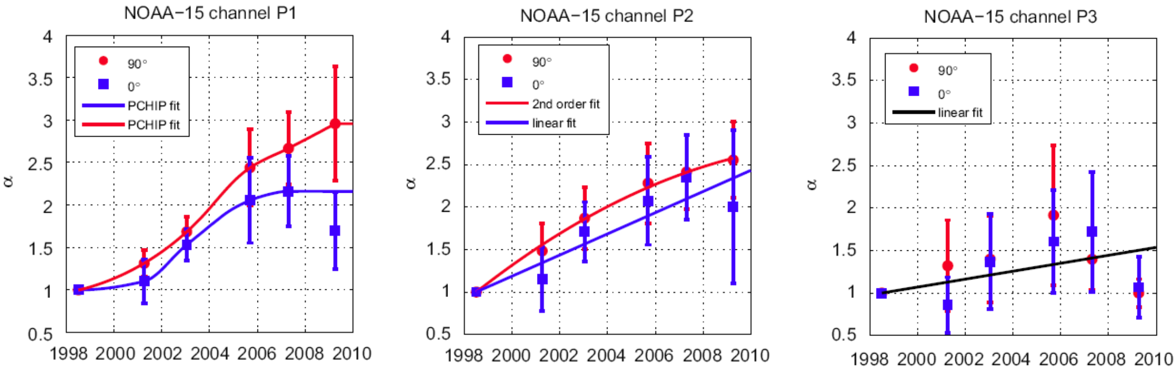

Figure 6.23 The α factors for NOAA-15 as a function of time for 90° and 0° detectors and three lowest energy channels.

After the α factors have been determined as a function of time we can correct the measured fluxes. The fluxes are corrected by first fitting an interpolating cubic polynomial to the integral spectrum of the measured data. The energy thresholds of the channels are now $\alpha_i E_i$. Using the interpolating polynomial we can compute the values of the integral spectrum $F_o(E_i)$ at the original nominal energy thresholds and then obtain the corrected count rates at the i:th channel as $N_i=F_o(E_i)-F_o(E_{i+1})$. The corrected and uncorrected fluxes of all satellites for the 0° detector at the three lowest energy channels are shown in Figure 6.24. One can see that there is a large difference between the corrected and uncorrected fluxes especially in 2006-2010. The correction seems to greatly improve the agreement between the flux levels measured simultaneously by different satellites. The correction produces best results at the 2nd and 3rd energy channels. For the 1st energy channel the correction overestimates the fluxes after the α factor has increased to above ~1.5 (see e.g., NOAA-12, the red curve). This is because the correction of the lowest energy channel requires extrapolation of the spectrum to lower energies than measured by the degraded instrument. It seems that the linear extrapolation in logarithmic scale used here tends to overestimate the spectrum. A better knowledge about the form of the spectrum would improve the correction for the lowest channel.

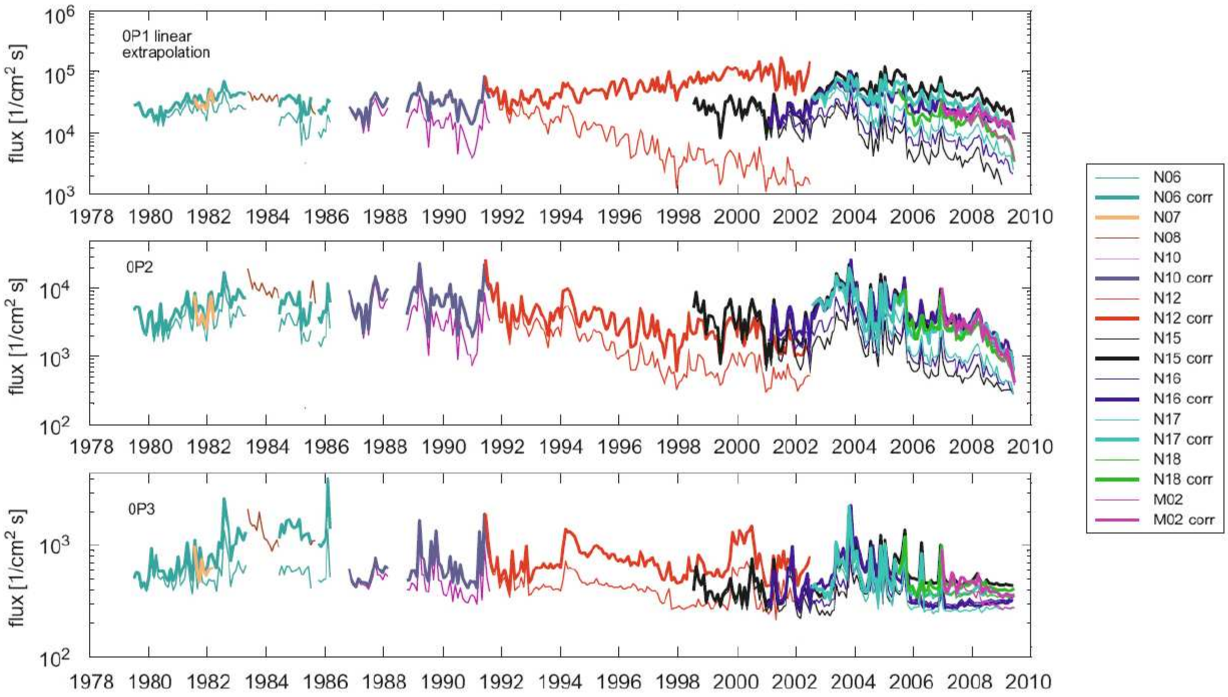

Figure 6.24 Corrected (thick lines) and uncorrected (thin lines) proton fluxes in 0^o direction for P1-P3 channels. The different colored lines indicate different satellites.

It is interesting to compare the α factors to the corrected proton fluxes which are responsible for the radiation damage in the first place. Figure 6.25 shows the α factors as a function of the cumulative corrected particle flux measured by the satellite outside the South Atlantic Anomaly. The comparison is shown for the 0^o and 90^o detectors of the SEM-1 and SEM-2 package satellites. One can see that the α factors are roughly linearly dependent on the cumulative particle flux. More importantly, all different detectors behave almost identically even though the satellites have different orbital planes and have been launched at different times. Of course, such a similar response to radiation damage is expected since the detectors should be identical.

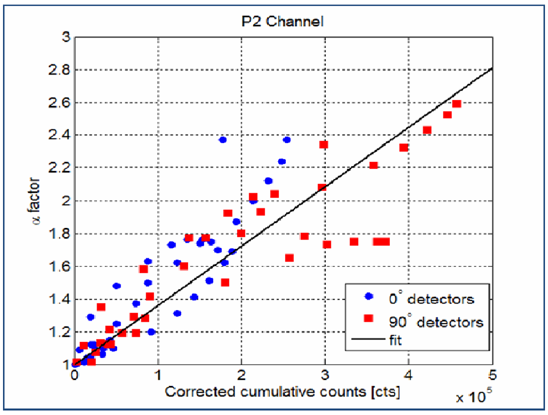

Figure 6.25 The α factors of different detectors onboard NOAA-15, 16, 17, 18 and METOP-02 as a function of the cumulative corrected flux measured by the satellite.

6.3 Effects of atmospheric heating on satellite orbits

It is well known that satellite orbits are perturbed due to variations in atmospheric density. Although the density of the upper atmosphere is very low it nevertheless exerts a drag force on spacecraft in orbit around the Earth, most notably of course for spacecraft in a low Earth orbit. If no compensating action is taken, this drag force will cause the satellites slowly to lose altitude and eventually fall down. It is therefore of importance to satellite operators and mission planners to be able to estimate the size of the drag. However, this is complicated by the fact that the density at a given altitude is highly time variable. Heating of the thermosphere in general cause the atmosphere to expand and thus increases the thermospheric density at satellite level. Various processes contribute to the thermospheric heating. The atmosphere is heated directly by the absorption of solar EUV radiation in the thermosphere, and more indirectly also by the solar wind through its effect on geomagnetic activity and particle precipitation. Thus the three most important sources are believed to be solar radiation, Joule dissipation related to geomagnetic activity and kinetic energy dissipation of precipitating particles, the latter primarily in the auroral region. In general solar EUV radiation provides the largest contribution to the heating, but during periods of high magnetic activity, such as strong geomagnetic storms, the Joule heating can be excessive (Knipp et al. 2004). The heating due to precipitating particles is believed to provide only a minor contribution (Knipp et al. 2004).

One important goal of WP4 in SOTERIA is to investigate the relationship between geomagnetic activity and Joule heating and if possible to construct new and improved geomagnetic measures of the Joule heating based on magnetic satellite data (Delivery 4.4). In this section we describe the first results of an investigation of the effect of geomagnetic activity on atmospheric densities and LEO satellite orbits. Various ground-based geomagnetic indices have been used as proxies for Joule heating and are currently used as input for different models of thermospheric density and temperature. In his pioneering work on the energy injection parameter ε, designed as a measure of the energy injection rate from the solar wind to the magnetosphere, Akosofu (1981) assumed that the Joule heating was proportional to the ionospheric Hall current and in consequence to the auroral electrojet index AE, measuring the sum of the eastward and westward electrojet intensity. This approach was taken up again by Ahn et al. 1983, and also Baumjohann and Kamide (1984). Inspired by various studies of Joule heating based on the cross polar cap potential, Chun et al. (1999) found significant improvements by using the newly developed polar cap geomagnetic index PC (or rather a second order polynomium in PC). Recently Knipp et al. (2004) improved this further by using a combination of PC and the Dst index. The geomagnetic indices are also used as input to empirical models of the thermosphere. The MSIS model developed by Hedin (1987), which is used as basis for SPENVIS thus uses Ap as an input, while other atmospheric models use Kp or can use either Ap or Kp.

The CHAMP satellite is equipped with a GPS for accurate orbital determination, and also has the advantage in this context that it flies in a relatively low LEO orbit. At launch the average altitude for an orbit was ~470 km and in early 2006 this had decreased to ~350 km. Figure 6.26 shows the rate of decrease of the CHAMP altitude from one orbit to the next, smoothed by computing running means of 31 consecutive orbits. For a circular orbit the altitude loss is approximated by the formula:

$$\Delta h = - \Delta r = 2\pi r^2 \rho / B$$

$$B = m/(C_D A)$$

where r is the distance from the spacecraft to the Earths centre, ρ is the atmospheric density at satellite altitude, B is the ballistic coefficient, C_D is the drag coefficient, m is the mass of the satellite and A is the cross section of the satellite perpendicular to the direction of flight. If the satellite attitude is constant relative to the direction of flight, which is usually the case for CHAMP, and if we consider only relative short time intervals where r is relatively constant, the rate of altitude loss is therefore approximately proportional to the atmospheric density. We can therefore use the rate of altitude loss for CHAMP to evaluate various proxies for Joule heating.

As mentioned above the two most important contributions to the rate of altitude decay is heating due to solar radiation and Joule heating. In consequence we compare the altitude rate of decrease to the most recent proxy for Joule heating developed by Knipp et al. (2004) and to the F10.7 index, which in many models serves as a proxy for the heating due to EUV absorption.

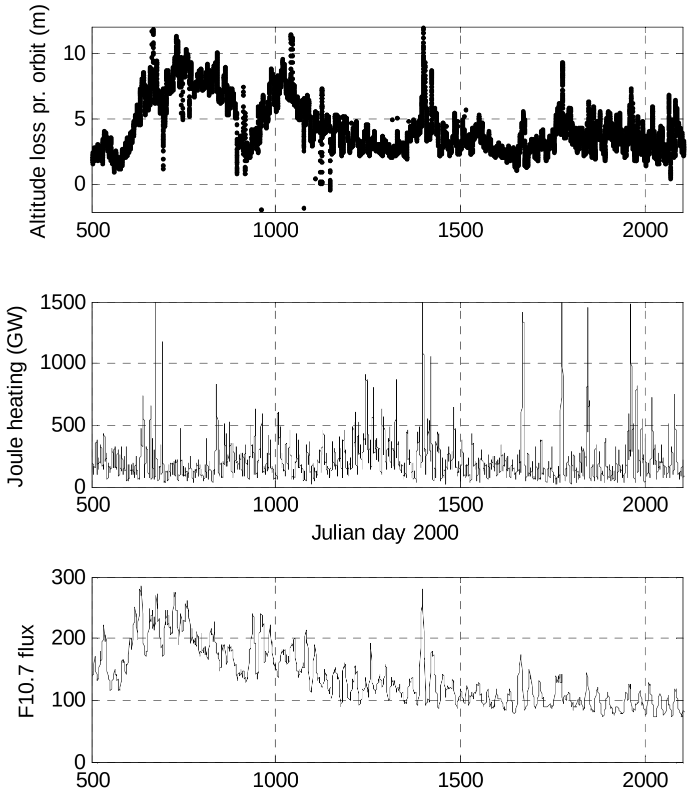

Figure 6.26
Top: Rate of altitude loss of the CHAMP satellite as a function of time (Julian day 2000=number of days elapsed since January 1. 2000).
Middle: The Joule heating proxy developed by Knipp et al. (2004) based on PC and Dst. The plot shown is 55 hour running means, corresponding roughly to the 31 CHAMP orbits.
Bottom: The Penticton adjusted F10.7 solar flux, also 55 hour means.

It can be seen from Fig. 6.26 that at these timescales the solar radiation is clearly the dominant factor. The variability of the F10.7 flux has a close resemblance to the rate of orbital decay in altitude. However, if we consider shorter time variations, comparable to the typical timescales of geomagnetic storms, this picture is expected to change, not least in the latter part of the period where the F10.7 flux has decreased considerable. In Figure 6.27 we zoom in on a shorter time period at the end of the period displays at Figure 6.26. For this 50 day period starting March 15, 2005 the F10.7 flux was almost constant, and, as expected, we therefore see the effect of geomagnetic activity much more clearly. The Joule heating proxy based on PC and Dst seems to follow the rate of orbital decay rather well. Figure 6.28 shows a similar example, but now for a period where we have a more composite response to F10.7 changes and variations in geomagnetic activity.

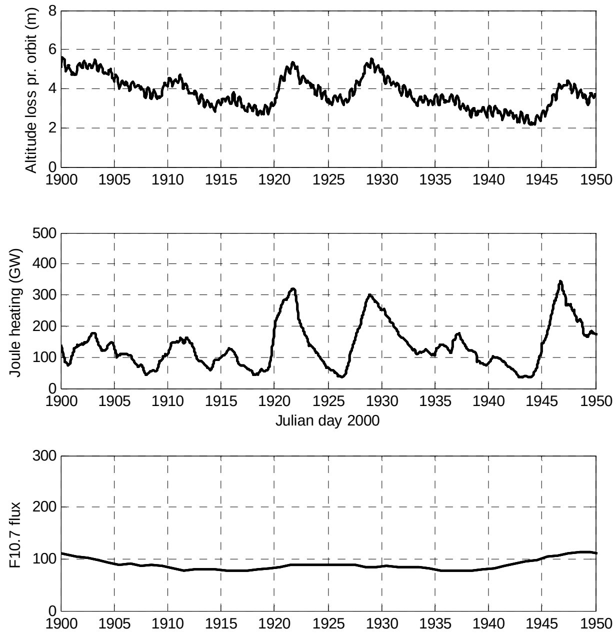

Figure 6.27

Same as Figure 6.26 but zoomed in on a 50 day time period starting in 2005 March 15.

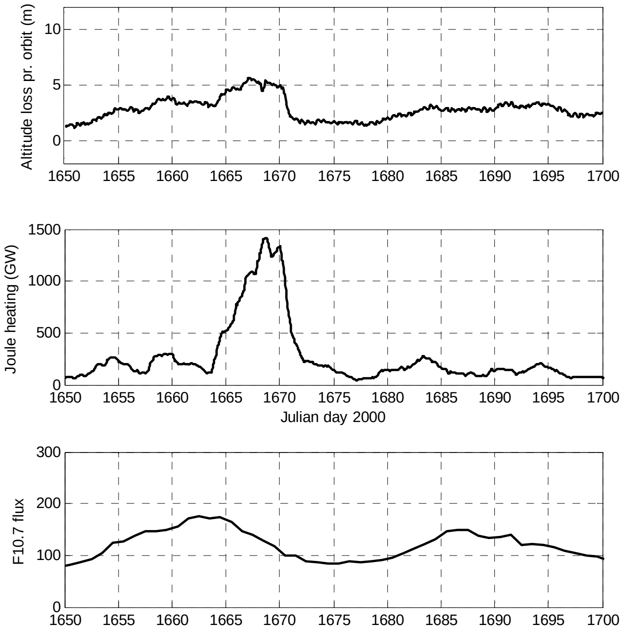

Figure 6.28

Same as Figure 6.27 but for the 50 day period starting at July 8. 2004. The prominent Joule heating event occurring between jd 1665 and jd1671 is the special 3-storm event selected for study by WP4.

It is evident from Figure 6.28 that in order to evaluate the capability of the different geomagnetic proxies to estimate the Joule heating it is necessary to separate the effect of the solar radiation as measured by the F10.7 flux. We therefore adopt the simple empirical approach modelling the rate of altitude loss Δh_{model} by a linear multiregression:

$$\Delta h_{model} = a_0 + a_{10.7}F10.7 + a_{JH}JH_{proxy} = a_0 + \Delta h_{F10.7} + \Delta h_{JH}$$

Where a_0, $a_{10.7}$ and a_{JH} are regression constants, F10.7 is the F10.7 flux and JH_{proxy} is the geomagnetic Joule heating proxy.

Figure 6.29 shows the result of applying this simple model to the time period displayed in Figure 6.28. We see a very nice fit between the observations and the linear model based on the parameters F10.7 and JH_{proxy}. It is seen that during this period the *variability* due to Joule heating and to heating by solar radiation are comparable in size. Figures 6.30 and 6.31 show two more examples later in the solar cycle. Apart from few exceptions the altitude loss rate is very well represented by the two parameters.

Figures 6.29-6.31 all have two panels. The top panel was made by equating the Joule heating proxy JH_{proxy} with the geomagnetic index ap, and the bottom panel by using the proxy derived by Knipp et al. (2004) based on a combination of PC and Dst. Both of these indices evidently do quite well as proxy for the Joule heating, no significant difference between them can be observed in this simple model.

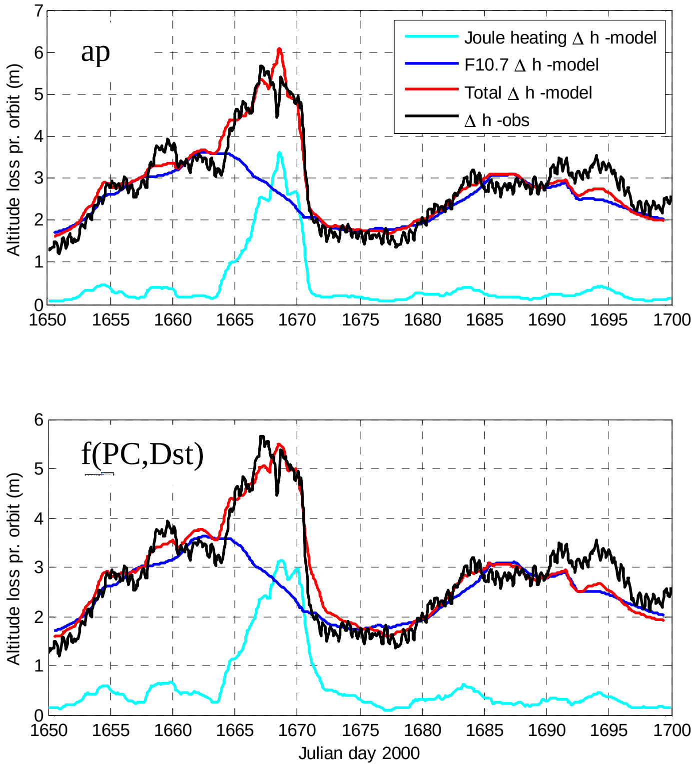

Figure 6.29

Simple multi-regression fit to the CHAMP altitude loss rate. The light blue line show the estimated altitude loss rate due to Joule heating, and the dark blue is the estimated loss rate due to heating from solar radiation. The red curve is the total estimated loss rate and the black curve is the observations.

Top: Joule heating estimate based on the geomagnetic index ap

Bottom: Joule heating estimate based on the Joule heating proxy of Knipp et al. (2004) based on PC and Dst.

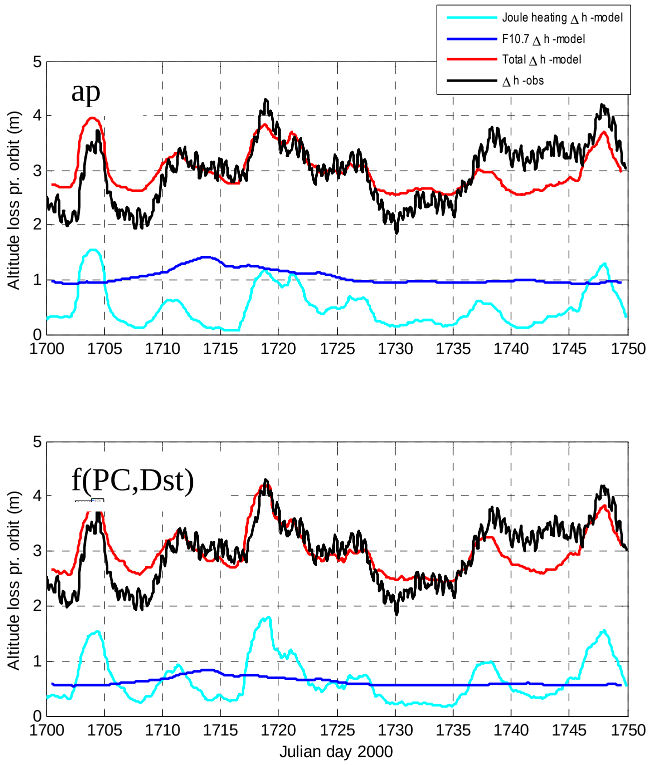

Figure 6.30

Same as Figure 6.29 but for another time period starting August 27th 2004.

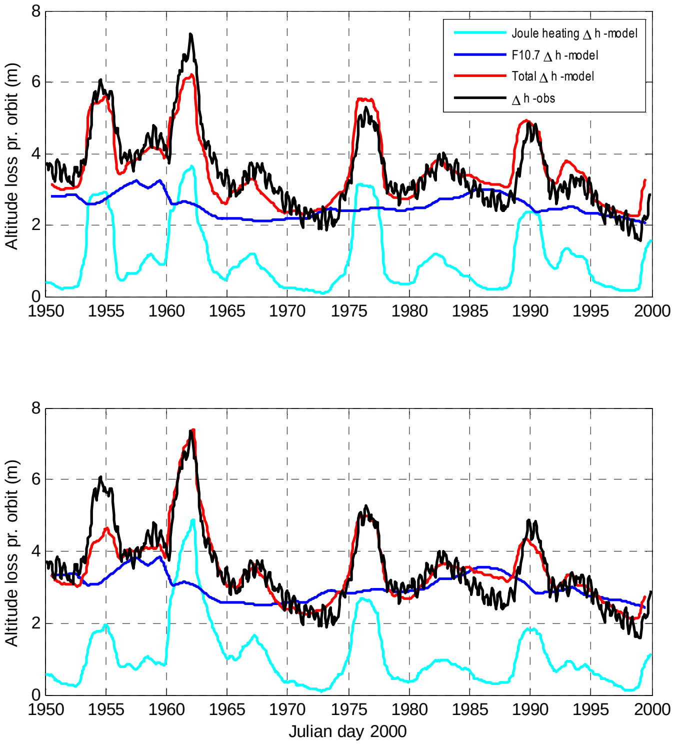

Figure 6.31

Same as Figure 6.29 but for another time interval starting May 4th 2005.

In Figure 6.32 we applied the same method but we used two other geomagnetic proxies for Joule heating, namely Kp and AE. The resulting fit is relatively good, but evidently poorer than for ap and the Knipp (2004) Joule heating proxy. In particular Kp yields larger deviations between model and observations. The same trend can be observed in Figure 6.33 when compared to Figure 6.31, although here both AE and Kp seems to produce a poorer fit to the observations than ap and the Knipp (2004) proxy.

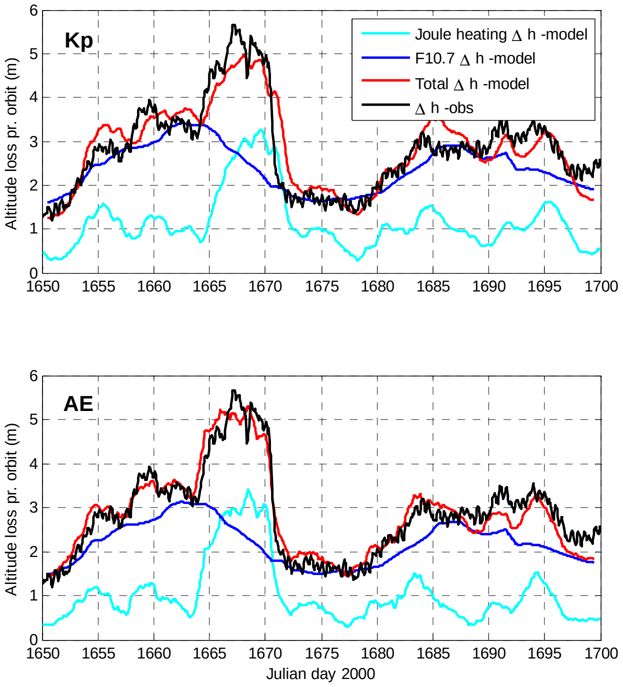

Figure 6.32

Same as Figure 6.29 but using to other geomagnetic indices as proxy for Joule heating.
Top: Kp was used as Joule heating proxy.
Bottom: AE was used as Joule heating proxy

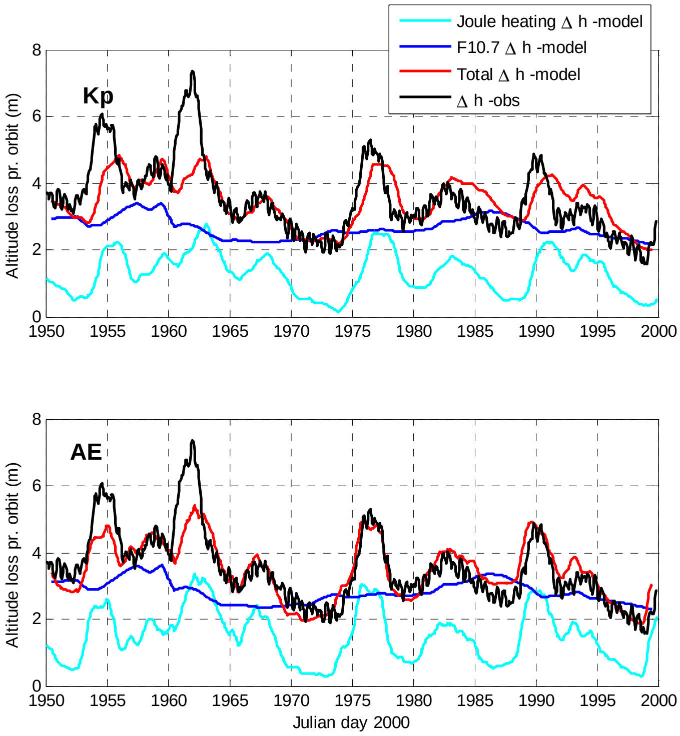

Figure 6.33

Same as Figure 6.31 but using to other geomagnetic indices as proxy for Joule heating.
Top: Kp was used as Joule heating proxy.
Bottom: AE was used as Joule heating proxy

Finally, we have examined a 100 day period in 2003 containing the two Halloween storms in late October and late November, which were some of the most powerful events of the entire cycle, and which are both part of the WP4 event list. Figure 6.34 shows the result by making a multi-regression fit using the four different geomagnetic proxies for Joule heating. Again ap and the Knipp (2004) proxy clearly provides the best results, particularly for the peak of the events. But room for improvement of the general fit, outside of the two main storm peaks, clearly exist. During this period the F10.7 flux was actually still quite high and the poorer fit may therefore also be due to inaccuracies in the use of the F10.7 flux as proxy for the heating by solar radiation.

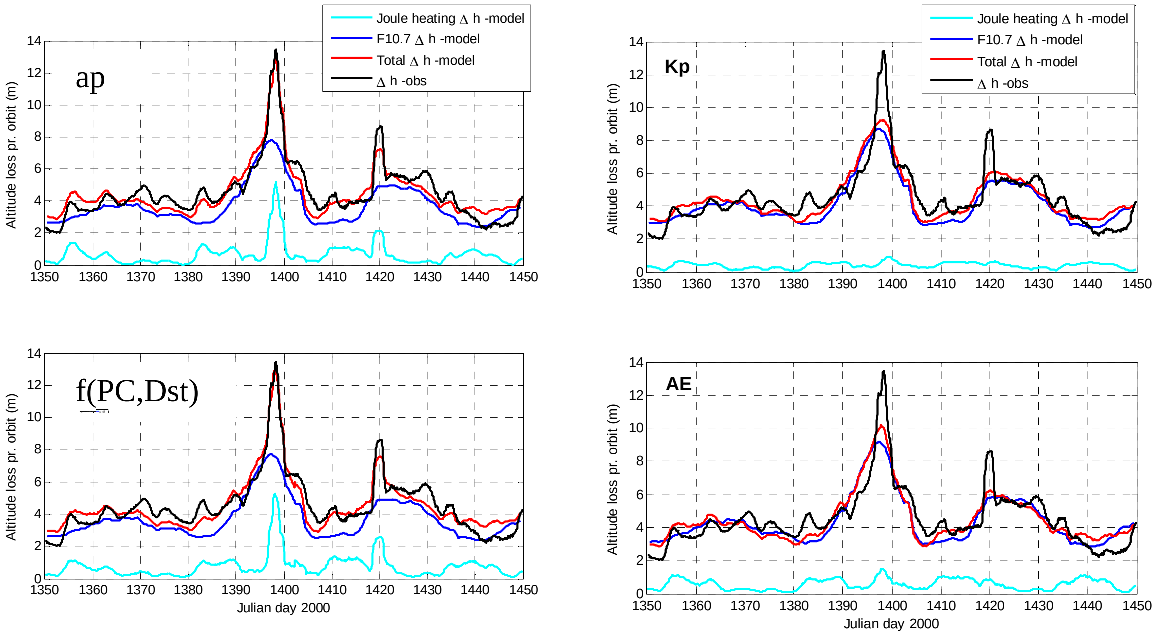

Figure 6.34

In summary, we have evaluated different existing geomagnetic proxies for Joule heating concerning their ability to reproduce the rate of altitude decay of CHAMP. We examined only variations of time scales of days and longer, and only for a set of selected periods. We find that the Joule heating contributes significantly to the altitude loss rate, particularly during periods of low solar activity and/or during large geomagnetic storms. In periods of low solar activity we also find a very nice fit when using either the Knipp (2004) Joule heating proxy based on PC and Dst or by using ap directly as Joule heating proxy. The fit is poorer when AE and Kp are used, particularly for the very large events in 2003. In the coming period of the SOTERIA collaboration, we will examine these effects in more detail, in particular we will develop a new geomagnetic proxy for Joule heating based on satellite magnetic data (see section 4.2 for the first results). The new method will then be evaluated using the same method as described above for the ground based magnetic indices.

7. Summary

This report D4.3 of SOTERIA has been summarizing the results of different investigations performed in the research field of Task 4.2: Solar wind – magnetosphere coupling and terrestrial impact. Each section was presenting the work of a smaller team of Work Package 4 participants. Almost all studies were dealing with one or more of the eight large solar events of D4.1.

In Section 2 the location of the magnetopause and that of the bow shock were investigated during extreme solar wind conditions when these discontinuities were unusually close to the Earth. Bow shock and magnetopause observations of the Cluster spacecraft and magnetopause crossings of the geosynchronous GOES satellites were compared to the predictions of different models. The full three-dimensional MHD BATS-R-US model (time consuming run in the Community Coordinated Modeling Center) reproduced the location of both discontinuities well. Good predictions were provided by the three-dimensional empirical magnetopause model of Lin et al. (2010), which is easy to use and fast compared to global 3D MHD modelling. The Cluster spacecraft usually observed the bow shock closer to the Earth than predicted by the simple 2D models. A three-dimensional bow shock model is also needed which is easy to use and it takes into account the shape of the 3D magnetopause in addition to the interplanetary parameters.

Section 3 was discussing the contributions of the ring, tail and magnetopause currents to the Dcx (corrected Dst) index. In the past, only some quantitative estimates of the tail current effects were discussed when Dst was estimated. Here, quantitative expressions were presented for the different contributions, which were evaluated each hour allowing us to follow the intensity and dynamics of the different current systems. We found, e.g., that the tail current is very dynamic during magnetic storms and its contribution to the Dcx can be quite large, on rough average about 30 %.

Section 4.1 analyzed the effect of the solar wind on energetic protons in the ring current. Fluxes were found to increase with increasing solar wind electric field for southward IMF. Also, solar wind velocity influences the proton fluxes, i.e. they increase with increasing velocity. In Section 4.2, field-aligned currents and ionospheric currents were derived from single passes of the Ørsted and Champ satellites. The Joule heating derived directly from the ionospheric currents was fitting well with empirical models based on the Dst and PC indices. The aim is to develop this method to an operational tool which may run automatically when receiving input data from satellites in order to deliver position and strength of currents in different regions as well as Joule heating and other ionospheric parameters.

Section 5.1 discussed that the cut-off latitude of solar energetic particles is highly correlated with the auroral boundary index, particularly in the dusk and midnight sectors. During magnetic storms, however, the cut-off latitude is both time-varying and local time dependent. Though correlation with Dst gives some information on variations in cut-off latitude during magnetic storms, magnetic intensity measurements from satellites on low-Earth polar orbit may provide further information in specific local time intervals. Section 5.2 presented how magnetic field data from satellites on low-Earth polar orbit may be used to monitor the auroral electrojets, in particular how the location of the electrojet is related to energetic electron precipitation. During magnetic storms the TEC (total electron content) increases (except for negative ionosphere storms occurring during the summer period) indicating increased ionospheric conductances and thereby increased ionospheric currents and electrojet activity. From TEC maps one may derive the AB (auroral boundary) latitude, too. The TEC-AB latitude is in general close to the AB index latitude computed from DMSP satellite data, though the TEC-AB shows strong oscillations which are not seen in the AB index.

Section 6 was dealing with the effects of the radiation belts on space instruments and atmospheric effects on the trajectories of near-Earth orbiting satellites. Protons and electrons of the radiation belts produce tracks in the CCD images of solar telescopes and enhance the background in photometric detectors as discussed in Section 6.1. Data obtained with the TESIS telescope aboard the CORONAS-Photon satellite were compared with the predictions of the SPENVIS space environment model during the last solar minimum period from February to November 2009. It was shown that the measured dose from radiation belt protons accumulated during one day in the TESIS CCD detector agree well with the SPENVIS estimation of the ionization losses. Energetic particles produced current pulses in the SPHINX X-ray spectrophotometer. The anisotropy of the signal in the polar regions is different from that in the SSA which may partly be explained by a non-uniform angular distribution of the trapped radiation belt particles.

Section 6.2 presented the analysis of the entire time series (from 1978 to present) of the MEPED energetic proton detectors onboard the low-altitude NOAA/POES satellites. By inter-satellite comparison we studied the effects of the radiation damage on the instruments and computed for each satellite the factors by which the effective energy thresholds of the instruments increased as a result of the radiation. We used these factors to correct the entire NOAA/POES dataset and produced the longest consistently calibrated dataset of energetic particle measurements. The results of this work were utilized in the calculation of the isotropic boundary that allowed us to separate the contribution of the tail current to the Dcx index.

The decay of the near-Earth orbit of the Champ satellite was discussed in Section 6.3. The density variations of the atmosphere at satellite altitude depend on solar heating of the thermosphere (EUV), kinetic energy depositing (precipitating particles), and Joule heating (ionospheric currents). After investigating the altitude variations of the satellite for 1500 days, we found that a linear combination of the F10.7 index and geomagnetic indices (Ap or PC/Dst) reproduce the major features of Champ's orbit decay. Particularly during periods of low solar activity and/or large geomagnetic storms, Joule heating contributes significantly.

The number of publications acknowledging SOTERIA is small in connection with this report. Most of the results have not yet been published, but several papers are in preparation. Therefore the authors would like to keep D4.3 at a dissemination level PP (restricted to other program participants).

References

Ahn, B.-H., S.-I. Akasofu, and Y. Kamide, The Joule heat production rate and the particle energy injection rate as a function of the geomagnetic indices AE and AL, *J. Geophys. Res., 88*, 6275-6287 (1983)

Akasofu, S.-I., Energy coupling between the solar wind and the magnetosphere, *Space Science Reviews 28*, 121-190 (1981)

Asikainen, T., Mursula, K., Filling of the South Atlantic Anomaly by energetic electrons during a great magnetic storm. *Geophys. Res. Lett. 32*, L16102 doi:10.1029/2005GL023634 (2005)

Asikainen, T., Mursula, K., Energetic electron flux behavior at low L-shells and its relation to the South Atlantic Anomaly. *J. Atmos. Solar-Terrestrial Phys. 70*, 532–538 (2008)

Asikainen, T., and K. Mursula, Recalibration of NOAA/MEPED energetic proton measurements, *J. Atmos. Solar-Terrestrial Phys.*, doi:10.1016/j.jastp.2009.12.011, in press, available online (2010)

Asikainen, T., and V. Maliniemi and K. Mursula, Modeling the contributions of ring, tail and magnetopause currents to the corrected Dst index, *J.Geophys. Res.*, in press (2010)

Asikainen, T., R. Kerttula, K. Mursula, R. Friedel, D. Baker, F. Søraas, J. Fennell, and J. Blake, Global view of energetic particles during a major magnetic storm, in *The Inner Magnetosphere: Physics and Modeling*, *Geophysical Monograph*, vol. 155, edited by T. Pulkkinen, N. Tsyganenko, and R. Friedel, 97–104, American Geophysical Union (2005)

Baumjohann, W., and Y. Kamide, Hemispherical Joule heating and the AE indices, *J. Geophys. Res.*, *89*, 383-388 (1984)

Belov, A., L. Baisultanova, E. Eroshenko, H. Mavromichalaki, V. Yanke, V. Pchelkin, C. Plainaki, and G. Mariatos, Magnetospheric effects in cosmic rays during the unique magnetic storm on November 2003, *J. Geophys. Res*., *110*, A09S20, doi:10.1029/2005JA011067 (2005)

Buresova D., Lastovicka J. and De Franceschi G., Manifestation of strong geomagnetic storms in the ionosphere over Europe, in: *Space Weather, Research Toward Applications in Europe*, 185-202, J. Lilensten (ed.), Springer-Verlag Berlin Heidelberg (2007)

Burton, R., R. McPherron, and C. Russell, An empirical relationship between interplanetary conditions and Dst, *J. Geophys. Res., 80* (31), 4204–4214 (1975)

Chen, J., Nonlinear dynamics of charged particles in the magnetotail, *J. Geophys. Res., 97*, 15,001–15,050 (1992)

Chun F. K., D.J. Knipp, M.G. McHarg, G. Lu, B.A. Emery, S. Vennerstrom and O.A. Troshichev, Polar cap index as a proxy for hemispheric Joule Heating, *Geophys. Res. Lett. 26*, 1101 (1999)

Daglis, I. A., The role of magnetosphereionosphere coupling in magnetic storm dynamics, in *Magnetic storms*, *Geophysical Monograph*, vol. 98, edited by B. Tsurutani, W. Gonzalez, Y. Kamide, and J. Arballo, pp. 107–116, American Geophysical Union (1997)

Dessler, A., and E. Parker, Hydromagnetic theory of geomagnetic storms, *J. Geophys. Res., 64*, 2239–2252 (1959)

Dmitriev, A., J.-K. Chao, M. Thomsen, A. Suvorova, Geosynchronous magnetopause crossings on 29-31 October 2003, *J. Geophys. Res., 110*, CiteID A08209, doi: 10.1029/2004JA010582 (2005)

Engels, U., and N. Olsen, Computation of magnetic fields within source regions of ionospheric and magnetospheric currents, *J. Atm. Sol.-Terr. Phys. 60*, 1585-1592 (1998)

Evans, D.S., M.S. Greer, Polar orbiting environmental satellite Space Environment Monitor-2: instrument descriptions and archive data documentation. NOAA Technical Memorandum, Boulder, Colorado OARSEC-93 (2000)

Fairfield, D.H., Average and unusual locations of the Earth’s magnetopause and bow shock, *J. Geophys. Res.*, *76*, p. 6700 (1971)

Farris, M. H.; S.M. Petrinec, C.T. Russell, The thickness of the magnetosheath - Constraints on the polytropic index, *Geophys. Res. Lett. 18*, 1821-1824 (1991)

Farris, M. H. and C.T. Russell, Determining the standoff distance of the bow shock: Mach number dependence and use of models, *J. Geophys. Res. 99*, 17,681-17,689 (1994)

Ferraro, V.C.A., On the theory of the first phase of a geomagnetic storm: A new illustrative calculation based on idealized (plane not cylindrical) model field distribution, *J. Geophys. Res.* 57, 15 (1952)

Fung, S., Recent development in the NASA trapped radiation models, in: *Radiation Belts: Models and Standards*, *Geophysical Monograph*, *97*, Lemaire, J., Heynderickx, D., Baker, D. (Eds.), American Geophysical Union, pp. 79–91 (1996)

Galand, M., Evans, D., Radiation damage of the proton MEPED detector on POES (TIROS/NOAA) satellites. NOAA Technical Memorandum, Boulder, Colorado OAR 456-SEC 42 (2000)

Ganushkina, N., T. Pulkkinen, M. Kubyshkina, H. Singer, and C. Russell, Long-term evolution of magnetospheric current systems during storms, *Ann. Geophys.*, *22*, 1317–1334 (2004)

Gburek, S., J. Sylwester, M. Kowalinski, J. Bakala, Z. Kordylewski, P. Podgorski, S. Plocieniak, M. Siarkowski, B. Sylwester, W. Trzebinski, S. Kuzin, A. Pertsov, Yu. Kotov, F. Farnik, F. Reale, K.J.H. Phillips, Soft X-ray Spectrophotometer SphinX: Science objectives, design and in orbit performance, *Solar System Research*, in press

Gonzalez, W., J. Joselyn, Y. Kamide, H. Kroel, G. Rostocker, B. Tsurutani, and V.Vasyliunas, What is a geomagnetic storm?, *J. Geophys. Res.*, *99 (A4)*, 5771–5792 (1994)

Grupen, C., Shwartz, B., Particle Detectors, *Cambridge Monographs on Particle Physics, Nuclear Physics and Cosmology, vol. 26*, second ed., Cambridge University Press (2008)

Gussenhoven M.S., D. A. Hardy, and W. J. Burke, DMSP/F2 electron observations of equatorward auroral boundaries and their relationship to magnetosphereic electric fields, *J. Geophys. Res.*, *86*, 768 (1981)

Gussenhoven M. S., D. A. Hardy, N. Heinemann, and E. Holeman, 1978 diffuse auroral boundaries and a derived auroral boundary index, *Rep. AFGL-TR-82-0398, Air Force Geophys. Lab.*, Hanscom, AFB, Mass. (1982)

Gussenhoven M. S., D. A. Hardy, N. Heinemann, Systematics of the Equatorward Diffuse Auroral Boundary, *J. Geophys. Res. 88*, NO. A7, 5692-5708 (1983)

Hardy, D. A., M. S. Gussenhoven, and R. Raistrick, Statistical and functional representations of the pattern of auroral energy flux. Number flux and conductivity, *J. Geophys. Res. 92*, 12275-12294 (1987)

Hedin, A. E., MSIS-86 Thermospheric model, *J. Geophys. Res. 92*, 4649-4662 (1987)

Hill, V.J., Evans, D.S., Sauer, H.H., TIROS-N/NOAA satellites space environment monitor archive tape documentation, *NOAA Technical Memorandum, Boulder*, Colorado ERL SEL-71 (1985)

Huston, S., Kuck, G., Pfitzer, K., Low altitude trapped radiation model using TIROS/NOAA data, in: *Radiation belts: Models and Standards of Geophysical Monograph, 97*, Lemaire, J., Heynderickx, D., Baker, D. (Eds.), American Geophysical Union, pp. 119–122 (1996)

Iijima, T., and T. A. Potemra, The amplitude distribution of field-aligned currents at northern high latitudes observed by Triad, *J. Geophys. Res., 81*, 2165 (1976)

Kalegaev, V., N. Ganushkina, T. Pulkkinen, M. Kubyshkina, H. Singer, and C. Russell, Relation between the ring current and the tail current during magnetic storms, *Ann. Geophys.*, *23*, 523–533 (2005)

Kalegaev, V., and E. Makarenkov, Dynamics of geomagnetic current systems during magnetic storms of different intensity, *Geomagn. Aeronomy*, *46(5)*, 570–579 (2006)

Karinen, A., K. Mursula, J. Takalo, and T. Ulich, An erroneous Dst index in 1971, in *Proc. of the SOLSPA 2001 Conference, ESA-SP-477*, 443–446 (2002)

Karinen, A., and K. Mursula, A new reconstruction of the Dst index for 1932-2002, *Ann. Geophys.*, *23*, 475–485 (2005)

Karinen, A., and K. Mursula, Correcting the Dst index: Consequences for absolute level and correlations, *J. Geophys. Res.*, *111*, A08207, doi:10.1029/2005JA011299 (2006)

Knipp D. J., W.K. Tobiska ,and B. A. Emery, Direct and indirect thermospheric heating sources for solar cycles 21-23, *Solar Physics*, *224*, 495-505 (2004)

Knipp D. J., Special Section on the Joint CEDAR-SCOSTEP Meeting, *J. Atm. Solar-Terr. Phys.* 66, 805 (2004)

Kress, B. T., M. K. Hudson, K. L. Perry, and P. L. Slocum, Dynamic modeling of geomagnetic cutoff for the 23–24 November 2001 solar energetic particle event, *Geophys. Res. Lett., 31*, L04808, doi:10.1029/2003GL018599 (2004)

Kress, B. T., C. J. Mertens, and M. Wiltberger: Solar energetic particle cutoff variations during the 29–31 October 2003 geomagnetic storm, *Space Weather, 8*, S05001, doi:10.1029/ 2009SW000488 (2010)

Kuzin, S.V., S.A. Bogachev, I.A. Zhitnik, A.A. Pertsov, A.P. Ignatiev, A.M. Mitrofanov, V.A. Slemzin, S.V. Shestov, N.K. Sukhodrev, O.I. Bugaenko, TESIS experiment on EUV imaging spectroscopy of the Sun, *Adv. Space Res. 43*, 1001-1006 (2009)

Kuzin, S. et al. The TESIS Solar Imaging Spectroscopy Experiment on Board the CORONAS B Photon Satellite, *Bulletin of the Russian Academy of Sciences: Physics, 74*, 3337 (2010)

Lee, D. and B.T. Kress, Geomagnetic cutoff variations due to interplanetary shocks, *EOS Trans. AGU,* 89 (53), Fall Meet. Suppl., abstract SM53A-1661 (2008)

Leske, R. A., R. A. Mewaldt, E. C. Stone, and T. T. von Rosenvinge, Observations of geomagnetic cutoff variations during solar energetic particle events and implications for the radiation environment at the space station, *J. Geophys. Res.*, 106, 30,011–30,022, doi:10.1029/2000JA000212 (2001)

Lin, R.L., X.X. Zhang, S.Q. Liu, Y.L. Wang, J.C. Gong, A three-dimensional asymmetric magnetopause model, *J. Geophys. Res.*, 115, CiteID A04207, doi: 10.1029/2009JA014235 (2010)

Lopez, R.E. S. Hernandez, M. Wiltberger, C.-L. Huang, E.L. Kepko, H. Spence, C.C. Goodrich, J.G. Lyon, Predicting magnetopause crossings at geosynchronous orbit during the Halloween storms, *Space Weather 5*, S01005, doi: 10.1029/2006SW000222 (2007)

McFadden, J., Evans, D., Kasprzak, W., et al., In-flight instrument calibration and performance verification. In: *Calibration of Particle Instruments in Space Physics. Vol. SR-007 of ISSI Scientific Report*, Wüest, M., Evans, D.S., von Steiger, R. (Eds.), ESA Publications Division, pp. 277–385. (2007)

Mertens, C. J., B. T. Kress, M. Wiltberger, S. R. Blattnig, T. S. Slaba, S. C. Solomon, and M. Engle, Geomagnetic influence on aircraft radiation exposure during a solar energetic particle event in October 2003, *Space Weather, 8*, S03006, doi:10.1029/2009SW000487 (2010)

Moen, B., and J. Brekke, Observations of high latitude ionospheric conductances, *J. Atm. Terr. Phys. 55*, 1493-1512 (1993)

Mursula, K., and A. Karinen, Explaining and correcting the excessive semiannual variation in the Dst index, *Geophys. Res. Lett.*, *32*, L14,107 (2005)

Mursula, K., L. Holappa, and A. Karinen, Correct normalization of the Dst index, *Astrophys. Space Sci. Trans.*, *4*, 41–45 (2008)

Mursula, K., L. Holappa, and A. Karinen, Uneven weighting of stations in the Dst index, *J. Atmos. Solar-Terrestrial Phys.*, *doi:10.1016/j.jastp.2010.04.007*, in press, available online (2010)

Newell, P. T., Y.I. Feldstein, Y. I Galperin and C.-I. Meng, Morphology of nightside precipitation, *J. Geophys. Res.* 101, A5, 10737-10748 (1996)

O'Brien, T., and R. McPherron, An empirical phase space analysis of ring current dynamics: Solar wind control of injection and decay, *J. Geophys. Res.*, *105* (A4), 7707–7719 (2000)

Prölss, G.W.: Ionospheric F-region storms, in: *Handbook of Atmospheric Electrodynamics* 2, Volland, H. (ed.), 195-248, CRC Press Boca Raton, FL (1995)

Prölss, G.W.: *Physics of the Earth's space environment*, Springer-Verlag Berlin Heidelberg, (2004)

Raben, V.J., Evans, D.S., Sauer, H. H., Sahm, S.R., Huynh, M., TIROS/NOAA satellite space environment monitor data archive documentation: 1995 update. NOAA Technical Memorandum, Boulder, Colorado ERL SEL-86 (1995)

Sckopke, N., A general relation between the energy of trapped particles and the disturbance field near the Earth, *J. Geophys. Res. 71*, 3125–3130 (1966)

Seale, R.A., Bushnell, R.H., The TIROS-N/NOAA A-J space environment monitor subsystem. NOAA Technical Memorandum, Boulder, Colorado ERL SEL-75 (1987)

Sergeev, V., and B. Gvozdevsky, MT-index - a possible new index to characterize the magnetic configuration of magnetotail, *Ann. Geophys. 13*, 1093–1103 (1995)

Sergeev, V., M. Malkov, and K. Mursula, Testing the isotropic boundary algorithm method to evaluate the magnetic field configuration in the tail, *J. Geophys. Res. 98*, 7609–7620 (1993)

Sergeev, V. A., M. Sazhina, N. A. Tsyganenko, J.A. Lundblad and F. Soraas, Pitch-angle scattering of energetic protons in the magnetotail current sheet as the dominant source of their isotropic precipitation into the night-side ionosphere, *Planet Space Sci. 31*, 1147 (1983)

Sergeev, V., and N. Tsyganenko, Energetic particle losses and trapping boundaries as deduced from calculations with a realistic magnetic field model, *Planet. Space Sci. 30*, 999–1007 (1982)

Shue, J.-H., J.K. Chao, H.C. Fu, C.T. Russell, P. Song, K.K. Khurana, H.J. Singer, A new functional form to study the solar wind control of the magnetopause size and shape, *J. Geophys. Res. 102,* 9497-9511 (1997)

Shue, J.-H., P. Song, C.T. Russell, J.T. Steinberg, J.K. Chao, G. Zastenker, O.L. Vaisberg, S. Kokobun, H.J. Singer, T.R. Detman, H. Kawano, Magnetopause location under extreme solar wind conditions, *J. Geophys. Res. 103*, 17691-17700 (1998)

Søraas, F., Aarsnes, K., Oksavik, K., Ring current intensity estimated from low-altitude proton observations. *J. Geophys. Res. 107* (*A7*) doi:10.1029/ 2001JA000123 (2002)

Søraas, F., Aarsnes, K., Oksavik, K., Sandanger, M., Evans, D., Greer, M., Evidence for particle injection as the cause of Dst reduction during HILDCAA events. *J. Atmos. Solar-Terrestrial Phys. 66*, 177–186 (2004)

Sugiura, M., and T. Kamei, Equatorial Dst index 1957-1986, ISGI Publ. Off., Saint-Maur des-Fosses, France (1991)

Sylwester, J., S. Kuzin, Yu. D. Kotov, F. Farnik, and F. Reale, SphinX: A Fast Solar Photometer in X-rays, *J. Astrophys. Astr. 29,* 339-343 (2008)

Tsyganenko, N.A., Effects of the solar wind conditions on the global magnetosopheric configuration as deduced from data-based field models, *Eur. Space Agency Spec. Publ., ESA SP-89*, p. 181 (1996)

Tsyganenko, N., and M. Sitnov, Modeling the dynamics of the inner magnetosphere during strong geomagnetic storms, *J. Geophys. Res. 110,* A03208, doi:10.1029/2004JA010,798 (2005)

Turner, N., D. Baker, T. Pulkkinen, and R. McPherron, Evaluation of the tail current contribution to Dst, *J. Geophys. Res. 105* (A3), 5431–5439 (2000)

Vennerstrøm, S., E. Friis-Christensen, H. Lühr, T. Moretto, N. Olsen, C. Manoj, P. Ritter, L. Rastätter, A. Kuvshinov, and S. Maus, The Impact of Combined Magnetic and Electric Field Ananlysis and of Ocean Circulation Effects on Swarm Mission Performance, Swarm Final Report (2004)

Verigin, M.I., G.A. Kotova, J. Slavin, A. Szabo, M. Kessel, J. Safrankova, Z. Nemecek, T.I. Gombosi, K. Kabin, F. Shugaev, A. Kalinchenko: Analysis of the 3-D shape of the terrestrial bow shock by Interball/Magion observations, *Adv. Space Res. 28(6),* 857-862 (2001)

Verigin, M., J. Slavin, A. Szabo, G. Kotova, T. Gombosi, Planetary bow shocks: asymptotic MHD Mach cones, *Earth Planets Space 55*, 33-38 (2003)

Wissing, J., J. Bornebusch, M.-B. Kallenrode, Variation of energetic particle precipitation with local magnetic time. *Adv. Space Res. 41*, 1274–1278 (2008)

SOTERIA acknowledged:

Asikainen, T., and K. Mursula, Recalibration of NOAA/MEPED energetic proton measurements, *J. Atmos. Solar-Terrestrial Phys., doi:10.1016/j.jastp.2009.12.011,* in press, available online (2010)

Asikainen, T., and V. Maliniemi and K. Mursula, Modeling the contributions of ring, tail and magnetopause currents to the corrected Dst index, *J. Geophys. Res.*, in press (2010)

Gburek, S., J. Sylwester, M. Kowalinski, J. Bakala, Z. Kordylewski, P. Podgorski, S. Plocieniak, M. Siarkowski, B. Sylwester, W. Trzebinski, S. Kuzin, A. Pertsov, Yu. Kotov, F. Farnik, F. Reale, K.J.H. Phillips, Soft X-ray Spectrophotometer SphinX: Science objectives, design and in orbit performance, *Solar System Research*, in press.

Kuzin, S.V., S.A. Bogachev, I.A. Zhitnik, A.A. Pertsov, A.P. Ignatiev, A.M. Mitrofanov, V.A. Slemzin, S.V. Shestov, N.K. Sukhodrev, O.I. Bugaenko, TESIS experiment on EUV imaging spectroscopy of the Sun, *Adv. Space Res.*, *43*, 1001-1006 (2009)

Kuzin, S., Bogachev, S. A.; Zhitnik, I. A.; Shestov, S. V.; Slemzin, V. A.; Mitrofanov, A. V.; Sukhodrev, N. K.; Pertsov, A. A.; Ignatev, A. V.; Bugaenko, O. I.; Ivanov, Yu. S.; Reva, A. A.; Zykov, M. S.; Ulyanov, A. S.; Oparin, S. N.; Goncharov, A. L.; Shergina, T. A.; Urnov, A. M.; Solovev, V. A.; Popova, S. G., The TESIS Solar Imaging Spectroscopy Experiment on Board the CORONAS B Photon Satellite, *Bulletin of the Russian Academy of Sciences: Physics*, *74,* 33-37 (2010)

Mursula, K., L. Holappa, and A. Karinen, Uneven weighting of stations in the Dst index, *J. Atmos. Solar-Terrestrial Phys.*, *doi:10.1016/j.jastp.2010.04.007*, in press, available online, (2010)

References on Internet

CCMC	http://ccmc.gsfc.nasa.gov/
CDAWeb	http://cdaweb.gsfc.nasa.gov/istp_public/
SOTERIA	http://soteria-space.eu/
SPENVIS	http://www.spenvis.oma.be/
OMNIWeb	http://omniweb.gsfc.nasa.gov/
International GNSS Service	http://igscb.jpl.nasa.gov/
SPHINX data	http://156.17.94.1/sphinx_catalogue/SphinX_cat_main.html/
IGRF model	http://wdc.kugi.kyoto-u.ac.jp/igrf/
Orbital data	http://www.space-track.org/
TESIS	http://tesis.lebedev.ru/en/